2014

Performance Analysis of PowerWindow: a Linear Wind Generator

Seyed AmirHosein Jafari
University of Wollongong

School of Electrical, Computer and Telecommunications Engineering

Faculty of Engineering and Information Sciences

Performance Analysis of PowerWindow: a Linear Wind Generator

Seyed AmirHosein Jafari

This thesis is presented as part of the requirements for the award of the Degree of Master of Philosophy in Electrical Engineering of the University of Wollongong

March 2014

ABSTRACT

Linear wind generators (LWGs) are a new type of wind turbine developed recently. Unlike the conventional horizontal or vertical axis wind turbines, the power extraction mechanism of linear wind generator is based on the translational movement of blades along a path perpendicular to the incoming wind. This study focuses on a LWG design developed at the University of Wollongong, named PowerWindow, which represents a modular wind power generator, and investigates its characteristics and performance.

The thesis develops an analytical model for PowerWindow using the modified blade element momentum theory. It also develops a simulation of this device using the computational fluid dynamic method. It is envisaged that in practice PowerWindow modules can be installed and operated in two different positions, either suspended on a frame or landed on ground. The suspended configuration means that the module is placed in an elevated position for example, between two towers, and landed configuration means that the module is placed on a flat surface, for example, the roof of a tall building. Aerodynamic mechanisms of PowerWindow in both positions are analyzed and compared using the modified blade element momentum theory and the computational fluid dynamic model, and also validated by the experimental data obtained from the prototype tests in the wind tunnel.

This study shows that the PowerWindow turbine can operate with acceptable efficiency in very low blade to wind velocity ratio, which is not achievable by conventional wind turbines at the same value of tip speed ratio. It is shown that installation position (suspended or landed) greatly affects its performance. This study

also shows that the front blades can significantly impact on the performance of the rear blades, by increasing their angle of attack. Increasing the angle of attack also increases the possibility of stall. However it is also shown that stall condition can be postponed by increasing the solidity.

CERTIFICATION

I, Seyed AmirHosein Jafari, declare that this thesis, submitted in fulfillment of the requirements for the award of Master of Philosophy, in the School of Electrical, Computer and Telecommunications Engineering, Faculty of Engineering and Information Sciences, University of Wollongong, is wholly my own work unless otherwise acknowledged. The document has not previously been submitted for qualification at any academic institution.

ACKNOWLEDGEMENTS

I would like to thank Prof. Farzad Safaei and Dr. Buyung Kosasih for being my advisors during the course of this study. This project could not be accomplished without their guidance, support and encouragement. They have been excellent supervisors and taught me different aspects of academic research.

I would also like to express my heartfelt thanks to my dear parents and wife for their unconditional love and support from overseas. They may not know how to make a good machine, but they do know how to make a good human being.

TABLE OF CONTENTS

LIST OF FIGURES

LIST OF TABLES

NOMENCLATURE

a	Induction factor (dimensionless)
A	Air swept area (m^2)
B	Airfoil plan area (m^2)
C_D	Drag coefficient (dimensionless)
C_L	Lift coefficient (dimensionless)
C_P	Coefficient of performance (dimensionless)
C_{sp}	Surface Pressure Coefficient (dimensionless)
F_D	Drag force (N)
F_L	Lift force (N)
$\dot{m}$	Mass flow rate ($kg\ m^{-2}\ s^{-1}$)
N	Number of blades in one side of PowerWindow
P	Power (Watt)
P	Pressure (Pa)
R_V	Velocity ratio (dimensionless)
V	Air velocity ($m\ s^{-1}$)
α	Angle of attack (degree)
β	Effective angle (degree)
θ_0	Design angle (dimensionless)
ε	Flow affected ratio (dimensionless)
σ	Solidity (dimensionless)
ρ	Air density ($kg\ m^{-3}$)
λ	Linear velocity ratio (dimensionless)

CHAPTER 1. INTRODUCTION

Wind turbines use wind kinetic energy of wind to rotate a shaft and generate electrical power. There are different designs for wind turbines but based on the orientation of the axis of rotation there are generally categorized into two groups: horizontal axis wind turbines (HAWTs); and vertical axis wind turbines (VAWTs). Coefficient of performance of HAWTs is generally higher than VAWTs. The maximum coefficient of performance of HAWTs is reported 45% to 50% while it is reported below 40% for efficient VAWTs [1]. Despite all the developments in this area many researches are still being done to develop new devices which can compete with the conventional technologies in capturing wind energy.

The challenge for developing a new device is to have high efficiency as well as being cost effective in comparison to conventional designs. Linear wind generator (LWG) is a new generation of wind turbines which are proposed for this purpose. Power extraction mechanism of LWG is based on the transitional movement of its blades over two straight lines in opposite directions perpendicular to the incoming wind. One LWG feature which makes it superior to the VAWTs and HAWTs is its ability to operate with a very low operation velocity but acceptable efficiency compared to those turbines. However very few studies have been done on optimization of LWG and enhancement of its performance; hence this device has not still been broadly utilized. PowerWindow, developed at the University of Wollongong, Australia, is a particular LWG design with some new characteristics and advantages, which is introduced and analyzed in this study.

1.1 Aims of the Thesis

PowerWindow is a new wind turbine design and many optimizations can be applied to enhance its performance. The main aim of this study is to develop a suitable analytical model for its power generation mechanism and verify this model using experimental and/or simulation methods. This model can later be used to optimize the design or evaluate various characteristics of this particular type of LWG.

1.2 Contributions of the Thesis

Three methods are developed in this study for analysis of power generation mechanism and performance of PowerWindow:

(i) An analytical model using the blade element momentum theory.

(ii) A numerical simulation using the computational fluid dynamic method.

(iii) Comparison with experimental data obtained from a wind tunnel test of the current prototype of the device.

1.3 Structure of the Thesis

The thesis is structured as follows.

Chapter 1. Introduction, describes the background, aims and contributions of the thesis.

Chapter 2. The Current Status of Research on Wind Generator Mechanisms and Performance Analysis, categorizes different wind turbines including PowerWindow based on their aerodynamics characteristics, and gives a general overview of their performance and reliability.

Chapter 3. Modified Bladed Element Momentum Theory for PowerWindow, derives an analytical model for PowerWindow using a modified blade element momentum method.

Chapter 4. PowerWindow Computational Fluid Dynamic model, describes the transitional model, mesh structure and solution method used in the computational fluid dynamic software for PowerWindow simulation.

Chapter 5. Results and Discussion, presents and analyses the coefficient of performances obtained by the analytical and numerical models for PowerWindow, validates them with the experimental data from the prototype wind tunnel tests, and compares the performance of PowerWindow in the two operating positions described in chapter 2.

Chapter 6. Conclusions, briefly discusses the accuracy of the PowerWindow analytical and numerical models and summarizes the results obtained by these models in both operation positions.

1.4 Publication Arising from the Thesis

Based on the investigations of this thesis a journal article entitled "Power Generation Analysis of PowerWindow, a Linear Wind Generator, using Computational Fluid Dynamic Simulations" has been submitted to the Journal of Wind Engineering & Industrial Aerodynamics, and is still under review. Another journal article entitled "Analysis of Aerodynamic Performance of Landed and Suspended PowerWindow using Numerical and Analytical Models" is also in the final stages of preparation.

CHAPTER 2. THE CURRENT STATUS OF RESEARCH ON WIND GENERATOR MECHANISMS AND PERFORMANCE ANALYSIS

2.1 Aerodynamics and Power Generation Mechanisms of Wind Turbines

The mechanisms of wind generators can be categorized by their aerodynamics. Exposing a flat object to an incident wind creates aerodynamics forces known as drag and lift forces. As shown in Figure 2.1, drag force is the component created parallel to the flow direction, and lift force is the component created perpendicular to the flow direction. As the aerodynamic quality of the object is better, the lift force is higher and the drag force is lower. Different aerodynamics of wind generators is explained in this part and they are categorized based on their aerodynamic mechanism.

Many studies have been done to improve aerodynamic quality of wind turbine blades. A number of commercial airfoils with different applications are shown in appendix A. Bak and Fuglsang [2], studied on enhancement of aerodynamic performance the NACA 622-415 airfoil, and as they have reported HAWTs structures are extremely dynamic, and are mostly subjected to complex distributions of aerodynamic forces. Malcolm [3] reported heavy vertical wind shear might result in motion in the vertical plane and yaw system of the rotor.

Based on the design of the turbines' rotors they can be lift-based or drag-based. Savonius wind turbine, (among VAWTs) is categorized as a drag-based wind turbine because its rotor rotates by the drag component of the aerodynamic force. Darrieus wind turbines (among VAWTs) and HAWTs are lift-based wind turbines. Their rotors basically rotate because of the lift component of the aerodynamic force. The

analytical model of some wind turbines such as Darrieus type is quite complex. Hence computational fluid dynamics is used for their power generation prediction. However, several analytical models are developed for HAWTs.

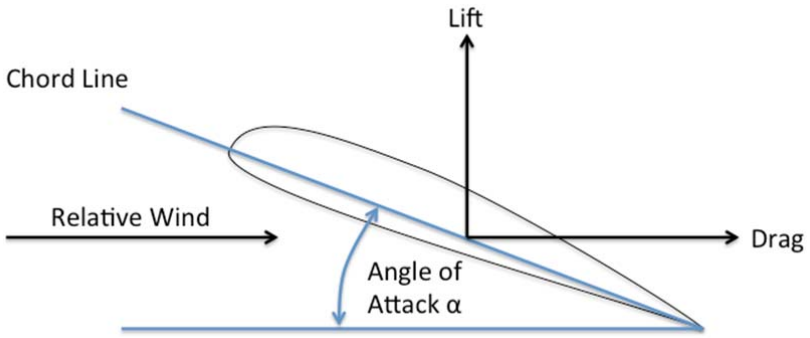

Figure 2-1. Aerodynamic forces over a blade (Drag and Lift components).

Many studies have been done on aerodynamic of wind turbine blades. Miller [4] developed aerodynamics analysis of HAWTs and emphasized the necessity of a comprehensive design theory. Schreck et al. [5] studied three-dimensional (3D), unsteady, vortex dominated flows creating dynamic stall on HAWT rotor blades in various wind speeds and yaw angles.

2.1.1 Horizontal Axis Wind Turbine (HAWT)

In the HAWTs the main rotor shaft is arranged on a horizontal axis.The first windmills were vertical axis wind turbines but, later HAWTs received more attention and HAWTs are currently more popular, because HAWTs primarily have higher coefficient of performance compared to other wind turbines. The maximum coefficient of performance of a modern HAWT has been reported up to 45% to 50% [1]. In the HAWTs the rotor shaft and the electrical generator are located on the top of a tower. The rotor is not able to capture the wind energy from all direction and

should be pointed to the wind direction. Hence a special mechanism is required to turn the rotor to that direction. Similar to the other lift-type wind turbines, HAWTs are very sensitive to variation in its blade surface roughness and profile design [6].

Large scales HAWTs have a yaw system which is a component basically that is adjust the orientation of the HAWT rotor towards the direction of the wind. In small scale HAWTs, the yaw system consists of a tail with a wing mounted on its end which creates a regulator moment which turns the wind turbine rotor towards the wind direction. This yaw system is also named ‘passive yaw system’. However the yaw system in the large size HAWTs is ‘active yaw mechanism’. In this yaw systems there is a wind sensor which can sense the wind direction, and there is a servo motor which creates a torque that is required to rotate the rotor and generator above the stationary tower.

Interests in the design and development of small scale wind turbines has world widely been increased during the last decades [7, 8]. The main idea behind that might be power generation from wind in the urban built environments. The idea is underpinned by the benefits from having power generated at the point of use. Despite this significant benefit, there are technological, economical and social hurdles which undermine wind turbine installations in the urban built environments [9] such as: (i) lack of suitable area for medium-large size wind turbines; (ii) noise pollution generated from (mainly medium-large size) wind turbines in high wind velocity conditions; and (iii) relatively low power output and unreliable performance due to unfavorable urban wind conditions such as low wind energy content (low wind velocity), continuously variable wind directions, high turbulence level and strong gust occurrences.

Billinton and Guung [10] showed that the site wind condition (speed and direction) extremely affect the reliability performance of a generating system. Therefore new large wind turbines use the active yaw mechanism to orient the wind turbine rotor to the wind direction. Minimizing the yaw angle maximizes the power output and minimizes the non-symmetrical loads. However, yawing cannot make a significant reduction in high wind speeds as it can in low-to-medium speeds, because the wind direction is less variable at high wind speeds compared to low-to-medium speeds.

(a) (b)

Figure 2-2. (a) Number of three-bladed HAWTs used in a wind farm. (b) A counter rotating HAWT.

Commercial HAWT rotors used in wind farms for electric power generation normally have three blades as shown in Figure 2.2. (a), these rotor should be pointed to the wind direction by computer-controlled motors. These rotors usually have high tip speed and efficiency, with a low torque ripple, which creates a good reliability. There are, however, limitations on how closely one can place wind turbines next to each other. This is because the rotary model creates a rotation of air flow in its vicinity and wake due to tip vortices and rotational torque imparted on air flow. The

interference from these turbulence flows will reduce the efficiency of adjacent wind turbines at close distances.

An alternative design of HAWT is counter-rotating HAWT shown in Figure 2.2 (b). This turbine has two rotors rotating oppositely on one axis. This technique assists in enhancing the maximum coefficient of performance of the HAWT. The maximum coefficient of performance of a counter-rotating HAWT without any losses is reported 64% [11]. Lee et al. [12] investigated aerodynamic characteristics of a counter-rotating HAWT using three kinds of rotor configurations (single rotor with 2 and 4 blades, and counter-rotating rotor with 2 blades on each rotor) and compared them using a numerical method. Hwang et al. [13] showed that the interactions of the front and the rear rotor creates a complex flow field in counter-rotating HAWTs. Choosing the rotational speeds, radius ratios and pitch angles of both rotors as the design parameters, optimized a counter-rotating HAWT, and observed variations of the coefficient of performances and thrust coefficients.

2.1.2 Vertical Axis Wind Turbine (VAWT)

In the VAWTs the main rotor shaft is arranged on a vertical axis. The primary advantage of the VAWTs compared to HAWTs is that there is no yaw mechanisms required for these types, which significantly simplifies their design and configurations [6]. Hence the VAWTs are more applicable than the HAWTs in mountainous areas and urban areas with extremely gusty winds. Another advantage of the VAWTs over the HAWTs is that they are less noisy than the HAWTs, which is very important for urban areas. However the VAWTs also have some main constraints compared to the HAWTs. Their TSR is basically lower than the HAWTs.

They are unable to self-start and control the output power or rotational speed by adjusting blades pitch angle [14].

VAWTs are effectively applicable on high buildings in the cities where wind speed reaches 14 m/s or greater. Similarly [15]. There are many VAWT designs, but they all have been categorized three groups: (a) Savonius VAWT, (b) Curved-blade Darrieus VAWT, and (c) Straight-blade Darrieus or H-rotor VAWT which are shown in Figure 2.3 (a), (b) and (c). Similar to the HAWTs, Darrieus (Curved-blade and Straight-blade/ H-rotor) VAWTs are lift-type wind turbines which typically have the maximum coefficient of performance from 30% to 45%. Savonius VAWTs are the only drag-type wind turbines, which its maximum coefficient of performance does not exceed 25% according to most investigators [6].

Savonius VAWT was invented by S.J. Savonius (Finnish engineer) in 1929. This type of VAWT is suitable for lower wind speeds and power applications. The greatest advantage of a Savonius rotor compared to the Lift-type VAWTs is its self-start ability [16]. Savonius VAWTs also have other advantages such as having low cost, simple construction, insensitivity to the wind direction, low angular velocity and noise in operation [17].

(a) (b) (c)

Figure 2-3. (a) Savonius VAWT, (b) Curved-blade Darrieus VAWT, and (c) Straight-blade Darrieus or H-rotor VAWT.

George Jeans Mary Darrieus (French engineer) invented the Darrieus VAWT in 1931. Although Darrieus VAWTs have the highest coefficient of performance among VAWTs, they generally have problems such as low starting torque and weak configuration structure [15]. The Eole, with 96 m height and maximum power of 3.8 MW was the largest Darrieus VAWT ever, which was built in 1986 [1]. Darrieus VAWTs have number of blades (usually aerofoil-shaped) attached to a vertical shaft. VAWTs are basically lift-type wind turbines. The wind creates an aerodynamic momentum on the blades due to the lift force and rotates them around the shaft. Gupta and Biswas [18] studied application of twisted blades in Darrieus VAWT rotor at the trailing edge. Sharpe and Proven [19] presented the idea of Cross-flex wind turbine. This idea uses an innovative configuration in the primary concept of Darrieus VAWT. From the coefficient of performance aspect the Darrieus VAWT is more desirable than the Savonius VAWT [20].

Many researches have been done on power augmentation of both VAWT types. Zhang et al. [21] studies on the semi-rotary VAWT with two perpendicular blades,

and found that adding disks at the bottom and top of the rotor enhances the confident of performance to till 30%. They have also stated that increasing the number of the turbine blades from 4 to 6 can improve its coefficient of performance up to 6–7% [22]. Bedon et al. [23] constructing a configuration characterized by rotor performance improvement, enhanced the coefficient of performance of Darrieus VAWT above 30% using an algorithm named W.O.M.B.A.T[1] [24].

Straight-blade or H-rotor VAWTs were developed in the United Kingdom through the research carried out during the 1970–1980s. It was shown that drag/stall effect created by a blade when leaving the wind flow constraints the speed which the contrary blade can propel the entire rotor. As a result the straight-blade/H-rotor Darrieus VAWT is self-regulating and in a short time after its cut-in wind speed can acheive its optimal rotational speed in all wind velocities[1]. Although the Darrieus VAWTs are known to have a lower C_P than the HAWTs, Mertens et al. [25] have shown that the coefficient of performance of an straight-blade/H-rotor Darrieus VAWT can be greater than HAWT if it is located on a rooftop. Another advantage of the straight-blade/H-rotor Darrieus VAWT over the HAWT is that unlike the HAWTs, their blades are not twisted and have much easier manufacturing process.

2.1.3 Linear Wind Generator (LWG)

Ponta et al. [26] studied on applications of large scale Darrieus VAWTs and presented a new design which was variable-geometry oval-trajectory (VGOT) Darrieus turbine. As Figure 2.4 shows the blades move on rail tracks located in an

1 . W.O.M.B.A.T is a software package for quantitative genetic analyses of continuous traits, fitting a linear, mixed model; estimates of covariance components and the resulting genetic parameters are obtained by restricted maximum likelihood [20].

elevated position, instead of rotating around a single rotor shaft. The blades are mounted on wheels which are coupled with electrical power generators. This design uses multi-directional power absorption capability of VAWT but operates with a high coefficient of performance (nearby 57% in the optimum design configurations), and resolve the low starting torque problems [27, 28]. The results from these studies show that VGOT Darrieus turbine achieves greater coefficient of performance with higher number of blades (N = 120‑160) in low TSR (~2) while at higher TSR, greater coefficient of performance can be achieved by a comparatively fewer number of blades (N = 60–80).

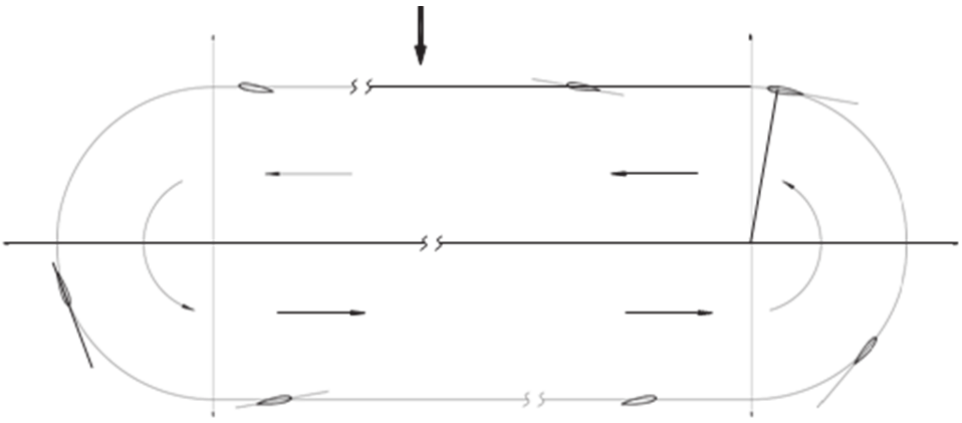

Figure 2-4. VGOT Darrieus turbine configuration [26].

As can be seen in Figure 2.5 the VGOT Darrieus blades are attached to a wagon which can follow a non-circular trajectory. Increasing the ration of transit perpendicular area to the total incoming wind area may results in increasing wind the energy conversion and optimizing efficiency of the entire plant. The VGOT Darrieus blades generate higher power output when tracking along the perpendicular line to the incoming wind direction, but they consume power instead of generation when tracking along the line parallel to the incoming wind direction.

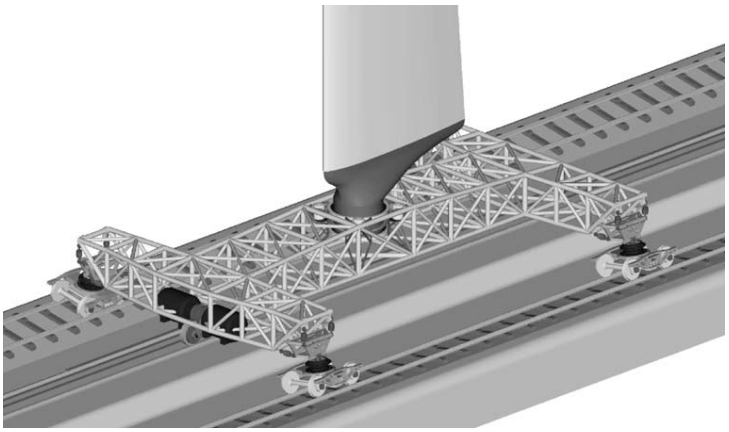

Figure 2-5. VGOT Darrieus blades are attached to a wagon following a non-circular trajectory [26].

VGOT Darrieus configuration allows increasing the swept area by increasing height of the trajectory line and/or widening the blades. On the other hand, the inflow direction remains constant along these straight tracks, which also results in the system aerodynamic and structural stability, while in the traditional Darrieus VAWTs the blades are subjected to a variable inflow in both magnitude and direction over the blades.

PowerWindow developed at the University of Wollongong, Australia, is another design among the LWGs. The variable-geometry oval-trajectory (VGOT) Darrieus turbine (which is initially a VAWT) [26-28] aerodynamic mechanism might be most similar to the PW, which allows them to operate efficiently at very low linear velocity ratios. This ratio is analogous to tip speed ratio (TSR) in HAWT and VAWT, but is required to be at much lower value than typical tip speed ratio of HAWT. However a major deference existing between these two designs is that the PW has also benefits the counter-rotating HAWT [11-13] power generation

mechanism which enables the front blades to enhance the power generation of the rear blades.

2.2 PowerWindow Mechanism

The approach to develop the PowerWindow is to abandon the rotary model (with its undesirable effects on creating turbulence in the vicinity and the wake of the turbine) and use a modular approach in building a large harvesting area. This design would have scalability with respect to technology, manufacturing and cost because the modules can be mass produced. A PowerWindow prototype is sketched in Figure 2.6. The current prototype dimensions are $2\text{m} \times 2\text{m} \times 0.4\text{m}$.

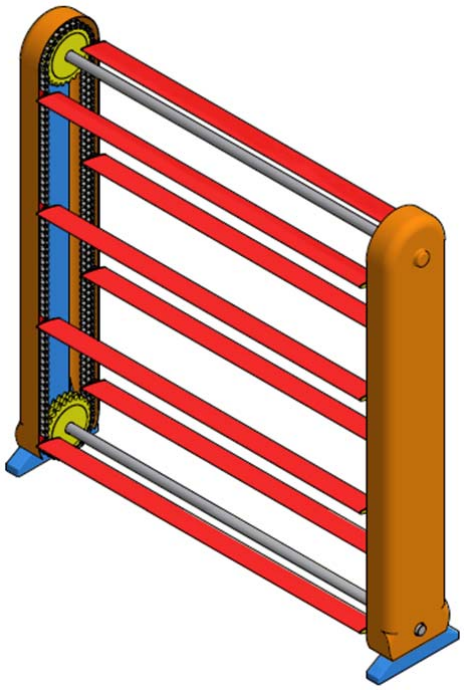

Figure 2-6. Sketch of PowerWindow module

There are two positions in which, PowerWindow can be located subjected to the wind: (i) somewhere elevated from the ground so that the wind can expand from

both side of the PowerWindow when facing, e.g. between two buildings which is named suspended position; (ii) and landed on the ground so that the wind can expand only from top side of the PowerWindow when facing it, e.g. on the top of a building which is named landed position. Figure 2.7 show PowerWindow inside the axial stream tube in (a) suspended position and (b) landed position.

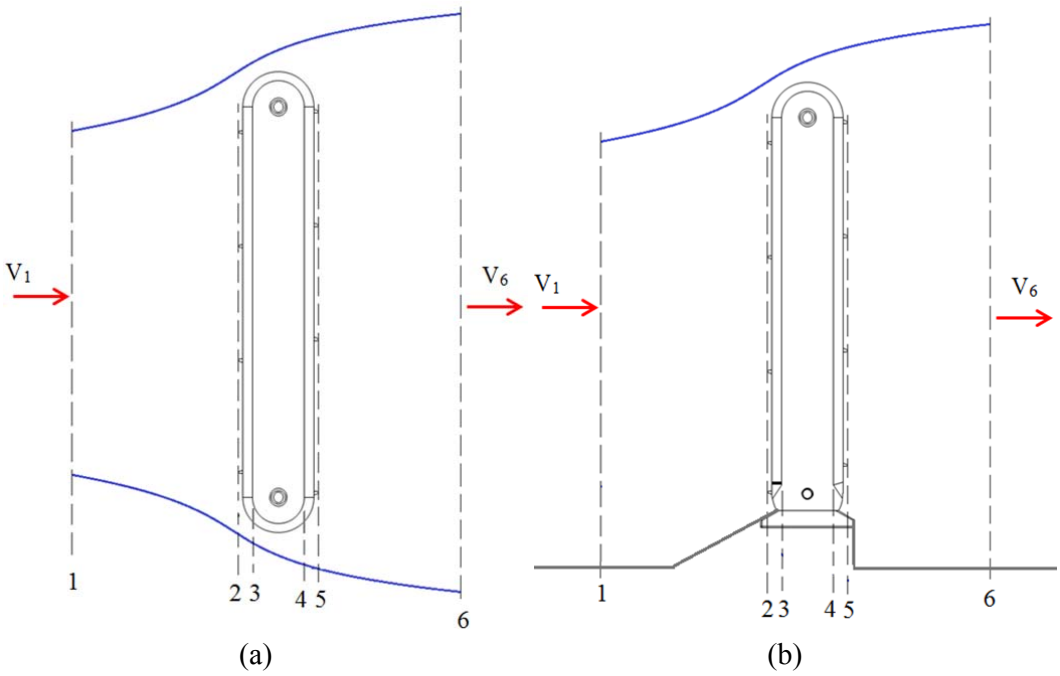

Figure 2-7. PowerWindow inside the axial stream tube in (a) suspended position and (b) landed position

A couple of rotating disks are mounted on this fixed frame and connected together with a shaft. The generator will be attached to this shaft using a gearbox. There are two belts running over each disk and guiding rollers at the top of the module. The blades are mounted on these belts. The wind will apply a lift force onto blades causing the belt to roll (similar to a garage door opening or closing). As the belt goes over the top roller guides and the bottom rotating disks, the blades will change side and orientation. The top and bottom sides of the PowerWindow are covered using an aerodynamically shaped (plastic) cover that guides the wind towards the center of the

module and enables the tips of the blades and their flipping over at the top and bottom to happen outside the wind.

As mentioned before, an important characteristic of the PowerWindow is that the blades do not rotate in the wind but are only experiencing a translational motion (up or down). As such, all the points on a blade move at the same speed and the blade does not impart a torque on the air flow. In addition PowerWindow edges are out of wind and covered so the tip vortices are likely to be small with little chance of interfering with neighboring modules. Consequently, the modules can be placed next to each other without significant loss of efficiency to build a large PowerWindow plant.

2.3 Summary of Wind Turbines Mechanisms

The key differences between the mechanisms of VAWT, HAWT and PowerWindow are briefly summarized in Table 2.1.

Table 2.1. Key differences between VAWTs, HAWTs and LWGs

	Straight-blade Darrieus VAWT	Curved-blade Darrieus VAWT	HAWT	PowerWindow (LWG)
Blade Profile	Simple	Complicated	Complicated	Simple
Need for Yaw Mechanism	No	No	Yes	Yes
Possibility of Pitch Mechanism	Yes	No	Yes	No need
Tower	Yes	No	Yes	No
Guy Wires	Optional	Yes	No	No
Noise	Low	Moderate	High	Very low
Blade Area	Moderate	Large	Small	small
Generator position	On ground	On ground	On tower	On frame
Blade load	Moderate	Low	High	Low
Self-start	No	No	Yes	Yes
Tower/frame interference	small	small	High	small
Foundation	Moderate	Simple	Extensive	Simple
Overall Structure	Simple	Simple	Complicated	Moderate

2.4 Wind Turbines Performance and Reliability

There are many limitations and difficulties which influence wind generators reliability and performance of wind generators. The most important is Betz's limitation. Betz's law computes the maximum energy which can be captured from the wind energy in free stream, disregarding the wind turbine design. Albert Betz (a German physicist) published it in 1919. Betz's law applying mass and momentum conservation principles of the flow stream passing through an ideal disk including the rotor, named "actuator disk" extracts the maximum energy from the wind stream. Betz's law shows that, no wind power generator can capture more than 59.3% of the wind kinetic energy. Therefore this factor is known as the Betz's limit.

Considering an air stream-tube entering the actuator disc (Figure 2.8), the wind speed at the upstream of stream-tube is equal to u_1 and its cross-sectional area is equal to A_1. As the actuator disc captures greater kinetic energy from the wind its exit velocity would be decelerated. By assuming air as an incompressible flow in low speeds ($u \leq 0.3\ Ma$), the cross-sectional area of the stream-tube expands instead of compressing the flow in the the stream-tube and this decelerates its velocity. The cross-sectional area of the stream-tube increases to A_2 in this section. Wind static pressure also drops from $P^+$to P^- when passing the actuator disk. As a result the downstream flow continue the expansion till static pressure of the flow reaches the atmospheric pressure, P_∞. This increases the cross-sectional area of the stream-tube far from the actuator disk from A_2 to A_3, where wind velocity is decelerated to u_3.

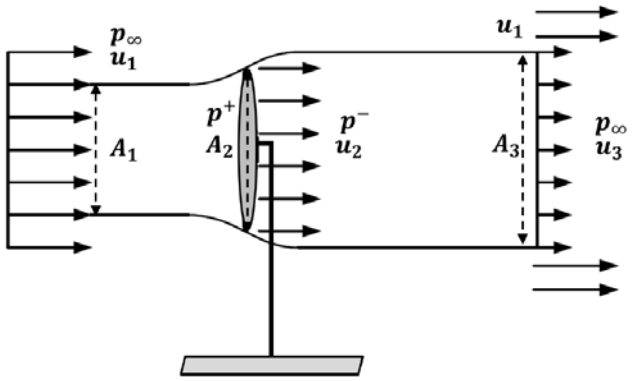

Figure 2-8. Stream-tube at the up-stream and down-stream of the actuator disc.

Assuming constant mass flow rate ṁ through the stream-tube, using continuity equation, its value would be:

$$\dot{m} = \rho A_1 u_1 = \rho A_2 u_2 = \rho A_3 u_3 \tag{2-1}$$

Equation 2.2 gives the total wind power available in the wind flow when its speed is $u_1$and passing through the cross-sectional area A_2 at the actuator disk section.

$$P_{max} = \tfrac{1}{2}\dot{m}_2 {u_1}^2 = \tfrac{1}{2}(\rho A_2 u_2){u_1}^2 = \tfrac{1}{2}\rho A_2 {u_1}^3 \tag{2-2}$$

This is the maximum wind power available in the wind flow.

Equation 2.3 gives the power extracted by the wind turbine

$$P_{ext} = \tfrac{1}{2}\dot{m}{u_1}^2 - \tfrac{1}{2}\dot{m}{u_3}^2 = \tfrac{1}{2}\rho A_2 u_2({u_1}^2 - {u_3}^2) \tag{2-3}$$

Also, using Bernoulli's equation, it can be written as:

$$\tfrac{1}{2}\rho {u_1}^2 + P_\infty = \tfrac{1}{2}\rho {u_2}^2 + P^+ \tag{2-4}$$

$$\tfrac{1}{2}\rho {u_2}^2 + P^- = \tfrac{1}{2}\rho {u_3}^2 + P_\infty \tag{2-5}$$

From equations 2.4 and 2.5, it can be derived that:

$$P^+ - P^- = \tfrac{1}{2}\rho {u_1}^2 - \tfrac{1}{2}\rho {u_3}^2 \quad (2\text{-}6)$$

The total axial thrust exerted by the turbine over the wind flow equals to the change rate in the momentum of the flow.

$$(P^+ - P^-)A_2 = \dot{m}(u_1 - u_3) \quad (2\text{-}7)$$

Or $$(P^+ - P^-)A_2 = \rho A_2 u_2 (u_1 - u_3) \quad (2\text{-}8)$$

From equations 1.7 and 1.8:

$$\rho A_2 u_2 (u_1 - u_3) = A_2(\tfrac{1}{2}\rho {u_1}^2 - \tfrac{1}{2}\rho {u_3}^2) \quad (2\text{-}9)$$

This implies, $u_2 = \frac{1}{2}(u_1 + u_3)$

The coefficient of performance (C_P) of a wind turbine is defined as the ratio of the extracted power over the total available power, shown in equation 2.10:

$$C_P = \frac{P_{ext}}{P_{max}} = \frac{\frac{1}{2}\rho A_2 u_2 ({u_1}^2 - {u_3}^2)}{\frac{1}{2}\rho A_2 {u_1}^3} \quad (2\text{-}10)$$

Therefore C_P can be written as shown in equation 2.11 and 2.12:

$$C_P = \frac{\frac{1}{4}\rho A_2 (u_1 + u_3)({u_1}^2 - {u_3}^2)}{\frac{1}{2}\rho A_2 {u_1}^3} \quad (2\text{-}11)$$

$$C_P = \frac{1}{2}(1 + \frac{u_3}{u_1})(1 - \frac{{u_3}^2}{{u_1}^2}) \quad (2\text{-}12)$$

If $y = \frac{u_3}{u_1}$

$$C_P = \frac{1}{2}(1 + y)(1 - y^2) \quad (2\text{-}13)$$

The maximum coefficient of performance occurs when $\frac{dC_P}{dy} = 0$, so:

$$\frac{dC_P}{dy} = \frac{1}{2}(1+y)(1-3y) = 0 \qquad (2\text{-}14)$$

Since, $y = \frac{u_3}{u_1} \neq -1$ and $y = \frac{1}{3}$. This gives maximum value of coefficient of performance: $C_{P,max} = C_P\left(y = \frac{1}{3}\right) = \frac{16}{27}$.

The ideal turbine defined by Betz is a HAWT operating with infinite blades at infinite TSR and no energy losses. This turbine is very similar to the actual wind turbines, which typically operate at high TSRs. At t high TSRs three blades are enough for interacting with the entire flow passing through the rotor area. A diffuser can be used for collecting further wind flow and conducting it through the turbine, which results in greater energy extraction. However, configuration of these shrouded turbines namely diffuser augmented wind turbines (DAWT) are more expensive because of the additional required structure.

Another factor which greatly influences the performance of the wind generators is their scale and scalability. Initially, the notion of a small wind turbine was defined based on its power generation capability which should be enough to supply an individual household electricity demand. However this is an approximation because the average household electricity demand is fixed around the world. There have also portable wind turbines been emerged for vehicles and small wind turbines for domestic applications. Nevertheless, developing larger wind turbines for capturing more wind power attracts significant interest.

Before 1990, wind turbines power generation capacity was typically less than 100 kW. This capacity increased to 500 kW by 1990, and increased to 750 to 1000 in

a few years. By 2000 and 2005, the turbine power generation capacity reached 2500 and 3500 kW respectively [29]. The largest turbine in world is currently Enercon E126 wind turbine (shown in Figure 2.9) with7.5MW power rating introduced in 2007. This turbine with 127 metre rotor diameters with segmented steel-composite hybrid blades is mounted on a concrete tower with a 135 metre hub height. However the V164 with 8MW power rating and164 metre rotor diameter will be the world's most powerful turbine in close future.

Figure2-9. Enercon E126 wind turbine.

There always been some common problems facing the wind turbines. Since the wind turbines are under dynamic forces, they are always subjected to fatigue due to vibration. Hence it has been tried to develop models in order to analyse vibration

problem in these devices. Ramsamooj, et al. [30] presented a new analytical model for corrosion fatigue. Ye, Z.Q., et al. [31] studied the 'structural dynamic characteristics of rotor blades to avoid sympathetic vibration problem' using theoretical and experimental methods. The test revealed that flap-wise vibration is the main vibration of the rotor blade and this problem is emphasized for the larger wind turbines because as the rotor is larger, it is exposed to greater fatigue load.

2.5 Methods for Wind Turbines Performance Analysis

PowerWindow is still in development process. In order to enhance its performance a model is needed which can accurately predict its flow mechanism and loads exerted over it blades. Since very few studies have been done on LWG types, an investigation is needed to be done over the same studies on the other wind generator types. Loading calculation over the blades is the most basic of power generation analysis in the wind turbines. The methods for calculating the aerodynamic forces on the turbine blades are currently: (i). Blade Element Momentum (BEM) theory; (ii). Computational Fluid Dynamics (CFD) simulations; (iii) experimental prototyping in wind tunnel" [32]. These three methods have been used in this study to develop models which can analyse the aerodynamic mechanism of PowerWindow.

2.5.1 BEM Method

A mathematical method for fluid dynamics analysis of wind turbines and evaluating its performance is BEM method [33]. The BEM aerodynamic analysis concept is based on Glauert's airscrew theory [34]. This method was previousely getting used for the analysis of propellers, exclusively in the helicopter industry [35].

Later its application was extended to wind turbines and computing the performance of wind turbines [36] BEM has recently broadly used for HAWTs analysis [37], [38], [39], [40] and VAWTs [23], using tabulated airfoil data. This method is also successfully applied for the tidal turbines [41], [42], [43].

BEM has been used for optimization of different types of wind turbines [44]. This method needs the blade two dimensional (2D) airfoil data, distributions of chord length and the twist angle along the blade length to find the optimum shape for blade. One major issue is that once HAWT blade optimization is done at one operating condition, the result is valid only for the relative TSR and angle of attacks. Hence that design will no longer be optimal for other TSR and angle of attacks [45].

Two assumptions are made in applying the BEM theory:

(i) There is no aerodynamic interaction between the elements; and

(ii) The forces on the blades are determined solely by the lift and drag characteristics of the airfoil shape of the blades [46].

The BEM model calculation is directly based on airfoil data and dependent on empirical corrections to two dimensional (2D) airfoil results to account for three-dimensional (3D) effects, such as tip losses, rotational flow, and dynamic stall [46]. Including the total loss (tip and hub loss) factor can improve BEM calculation accuracy. Prandtl [47] and Byand [48] developed BEM tip loss correction models. The modified BEM method has also been developed based on comparisons with actuator disc simulations [49].

The predictions obtained by the BEM method is reliable while it requires much less computational calculations compared to CFD simulation models [23]. However comparing CFD simulations and BEM method for small scale propellers, Carroll and Marcum [50] showed that the BEM method acceptably predicts the thrust with acceptable accuracy when the propeller operates with little separation and the blade has a high aspect ratio with little or no chord variation. However, in large regions of separated flow and blades of lower aspect ratio and chord variation, the accuracy of BEM diminishes. Moreover one key limitations of the BEM method compared to CFD simulation is that it cannot analyse the rotor impact on the surrounding flow [51]. Therefore a combination of BEM method and CFD simulations are being used in some recent studies [32], [51], [42], [52].

2.5.2 CFD Simulation

CFD is a numerical calculation to analyse to predict physical phenomenon such as flow and heat conduction in a flow [32]. The three-dimensional (3D) CFD simulations solving the Navier‑Stokes equations are very physically realistic, but they need very long calculation times [53]. The CFD simulations can give explicit modelling of turbine blades and estimate the complex turbulent flows adjacent to its blades and wake regions created at the far downstream [54].

CFD simulation is very useful when a rotor is subjected to a complex flow conditions which needs three-dimensional investigation. High turbulence level and variable flow directions can create such a complex condition. Another condition is when a significant part of blades is operating in stall condition. In such a condition it is not possible to rely on pre-determined lift coefficients achieved by wind tunnel

experimental test [55]. There are also very accurate and realistic CFD simulation methods for representation turbine wakes, which need very long calculation times, so are not usually used for their performance evaluation [56].

Many researchers have performed wind turbine CFD simulations using different methods. Sezer-Uzol and Long [57] computed the NREL Phase VI turbine in various wind speeds and yaw angles using the finite volume flow solver PUMA2 with rotating unstructured tetrahedral grids. Their results well agreed with experimental tests, but since the nature of their code was inviscid, it had limited ability for prediction in massive flow separation conditions. A comprehensive aerodynamic study was later performed by Buning, et al. [58] who computed the NREL Phase VI turbine with the NASA compressible RANS flow solver Overflow-D, based on a finite differences approach and overset grid [59]. They compared the results with the experiments, and using the validated results discussed the aerodynamic mechanisms of the wind turbine such as shaft power, normal force and pressure coefficient

Sørensen et al. [60] used a multi-block finite volume and incompressible RANS flow solver EllipSys3D to study the three –dimensional (3D) aerodynamic effects on a rotor-only configuration. Their computational results had good agreement with the experimental measurements. Mark and Dimitri [61] used the unstructured multi-grid RANS code NSU3D to predict the aerodynamics of an isolated wind turbine rotor. Bazilevs et al. [62] using a finite element and a (Non-Uniform Rational B-splines) NURB-based [63] method studied the NREL 5 MW baseline wind turbine rotor. NURB-based approach enables coupleing the aerodynamic and structural analysis.

CFD simulations which have been widely used in recent studies about wind turbines [64], [53], [59], [65]. The major advantage of CFD simulations compared to experimental prototyping is that they not only take less time and cost, but also can give further insight over flow mechanism passing through the wind turbines [66]. CFD simulations have also some advantages compared to BEM model. As mentioned before, in large regions of separated flow and blades of lower aspect ratio and chord variation, the accuracy of BEM diminishes [51]. While CFD simulations have successfully been used for performance analysis of large-scale wind turbines [67], [68], and wake effects on turbines downstream [69]. CFD simulations are also able to predict VAWT performance more accurately than BEM model [70].

2.5.3 Experimental Prototyping

Experimental prototyping is the most expensive and time consuming but also the most reliable method for performance analysis of the wind devices. There are some approaches to measure power generation performance of the wind turbines in a wind tunnel. Hirahara et al. [71] and Koki et al. [72] used small scale wind turbine models and measured the mechanical torque over the blade by installing a torque converter on the shaft. Hirahara et al. [71] successfully derived performance curves of a HAWT by applying an electronic load which could change the rotational speed of the rotor. Hailiang et al. [73] presented improved control strategies for doubly fed induction generator (DFIG)-based generators. Experimental prototyping has been previously widely used for modelling and analysis of HAWTs [74] and VAWTs [75].

CHAPTER 3. MODIFIED BLADE ELEMENT MOMENTUM MODEL FOR POWERWINDOW

As mentioned before BEM method combines two theories of momentum theory and blade element theory. Applying the momentum theory, the maximum coefficient of performance of a wind turbine cannot exceed over 59% (Betz limit). However the maximum coefficient of performance of conventional single rotor HAWTs is about 40‑50% which can be resulted by the energy losses such as viscous loss, three-dimensional loss, and transmission loss [11]. There is almost no three-dimensional loss in the PowerWindow, however its viscous loss is greater than VAWTs and HAWTs because unlike the other turbines, the PowerWindow blades have been allocated in a cascade configuration. When the fluid passes through the cascade, there will be a decrease in total pressure between the inlet to the cascade and at the section downstream of the cascade which is due to: (i) Frictional loss due to the formation of boundary layer on blades; and (ii) Losses due to mixing of blade wakes. Therefore BEM theory has been modified in this study by replacing lift and drag coefficient of the single blade by lift and drag coefficients of cascade.

3.1 Aerodynamics of Cascade

Operating condition, blade geometry and the airfoil lift and drag coefficients are essential parameters to be provided to generate the simulation code. As the blades might be under several different wind directions, the aerodynamic lift and drag curves are need in different angle of attacks(α). Most of the databases developed for aeronautical use are limited to a range of angle of attack (α) for Reynolds and Mach numbers which are greater than the values typically experienced by wind turbine

blades during operation [23]. For the airfoil used in PowerWindow, its lift (C_L) and drag (C_D) coefficients data were generated for $-14° < \alpha < 36°$ using Computational Fluid Dynamic (CFD) simulations. C_L and C_D can be defined in equations 3.1 and 3.2.

$$C_L = \frac{F_L}{\left(\frac{\rho B}{2}\right) V_{rel}{}^2} \tag{3-1}$$

$$C_D = \frac{F_D}{\left(\frac{\rho B}{2}\right) V_{rel}{}^2} \tag{3-2}$$

F_L is the component of the force that is perpendicular to the oncoming flow direction (not cord line direction) and F_D is the component of the surface force parallel to the flow direction (not cord line direction), B is the airfoil plan area, ρ is the air density and V_{rel} is the relative velocity of wind to the airfoil. Hence by obtaining F_L and F_D from the CFD simulations and having B, ρ and V_{rel}, the C_L and C_D of the airfoil can be calculated for each α. The CFD simulations have been done using $K-\omega$, SST transitional model for isolated airfoil and cascade configuration with three different solidities. The inlet wind velocity was set to $8\, ms^{-1}$ which is the average velocity that the PowerWindow is designed to operate in. As a result Reynolds number and Mach number of the flow over the airfoil were 7.1×10^4 and 2.33×10^{-2} respectively.

Figure 3.1 shows the PowerWindow airfoil cross-section. As mentioned before this airfoil is axisymmetric to the vertical axis since it is designed to extract power when flipped over and moves in the opposite direction in the rear side. Figure 3.2 shows a "goe 15k-il aerofoil" which is a commercial airfoil and partly similar to the PowerWindow aerofoil. The maximum thickness is 15% of the chord at 50% of its length. Therefor C_L and C_D data obtained by the CFD simulations for the isolated

PowerWindow airfoil is compared to goe 15k-il C_L and C_D from aerofoil database in Figure 3.3 (a) and (b) and 3.4 (a) and (b). C_L and C_D curves are not exactly the same but comparison shows that the CFD results are reasonable.

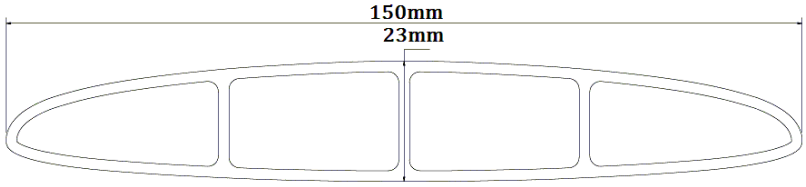

Figure 3-1. Cross section view of PowerWindow airfoil.

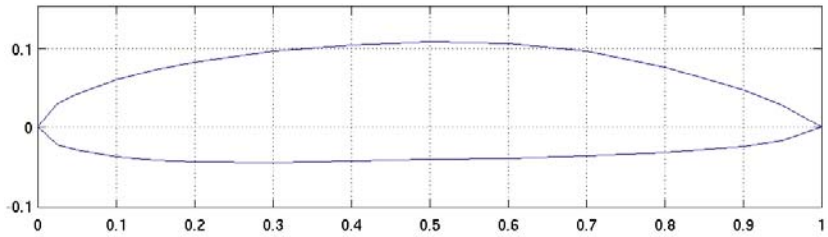

Figure 3-2. Cross section view of goe 15k-il aerofoil.

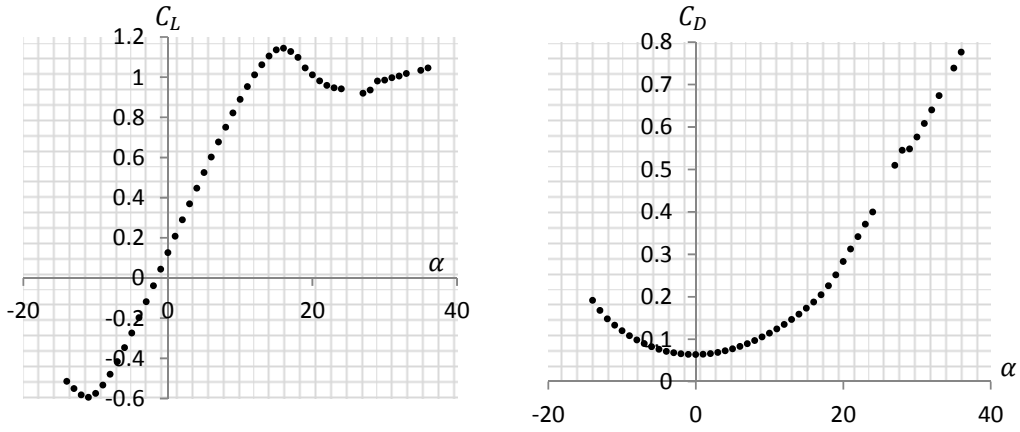

(a) (b)

Figure 3-3. (a) C_L and (b) C_D of the PowerWindow isolated airfoil.

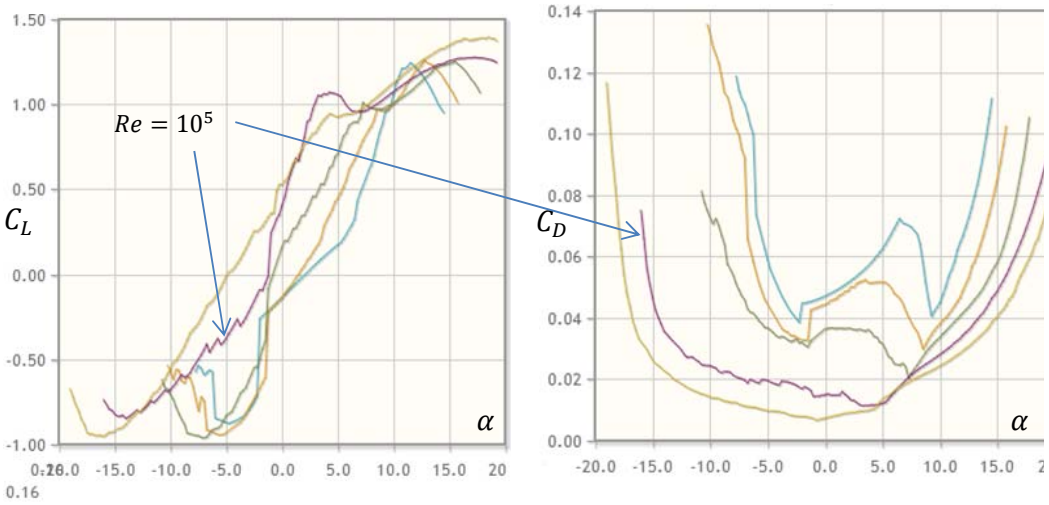

(a) (b)

Figure 3-4. (a) C_L and (b) C_D of goe 15k-il aerofoil.

Figure 3.6 (a) and (b) show C_L and C_D of isolated airfoil and cascade configuration with three different solidities ($\sigma = 0.428, 0.857$ and 1.714) against α obtained by the CFD simulations. C_L and C_D data is also reported in Table B.1 and B.2 in appendix B for $-14° < \alpha < 36°$. σ shows a relation between number of the blades, their blade and the rotor swept area, which is not similarly defined for every wind turbine. For a PowerWindow, it is defined as written below.

$$\sigma = \frac{NB}{A} \tag{3-3}$$

N shows the blade numbers and A is the swept area of a PowerWindow.

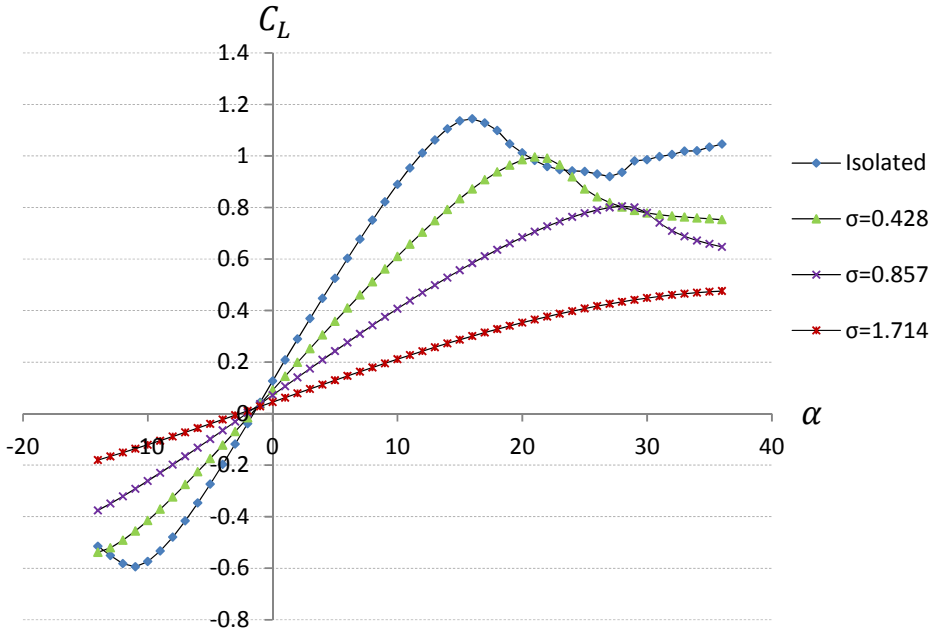

(a)

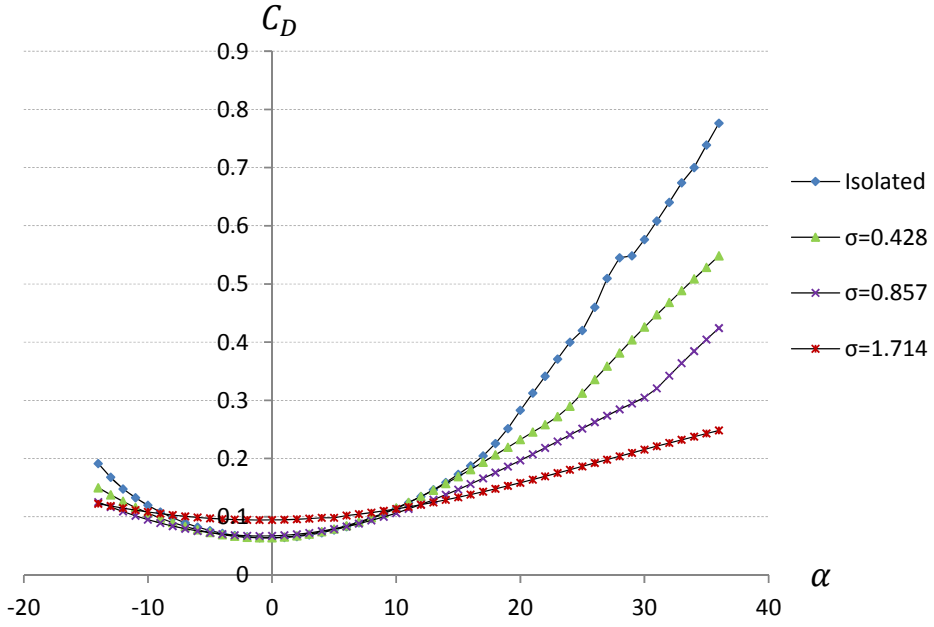

(b)

Figure 3-5. (a) C_L and (b) C_D of the PowerWindow isolated airfoil and cascade for different σ.

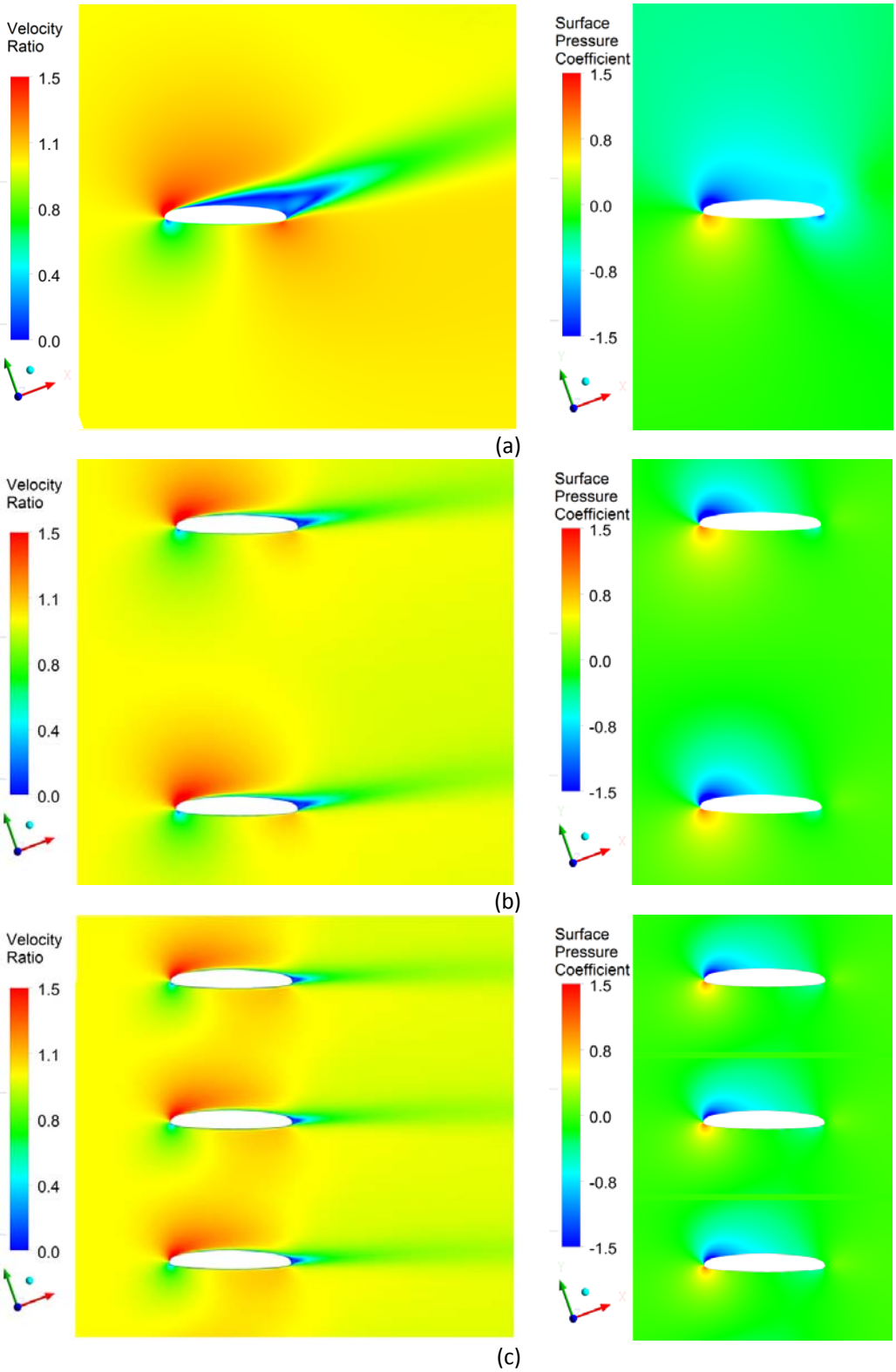

Figure 3-6. Velocity (on the left) and pressure (on the right) contours of (a). isolated airfoil and cascade configuration in (b). $\sigma = 0.428$ and (c). $\sigma = 0.857$ in $\alpha = 20°$.

As can be seen from Figure 3.5 (a), the maximum C_L for cascades are lower than the maximum for the isolated airfoil. Moreover as the solidity of the cascade increases, the maximum C_L decreases, and shifts to higher α. The reason can be investigated in the velocity and pressure contours around the blades. Figures 3.6 (a), (b) and (c) show the velocity (on the left) and pressure on the right) contours of the isolated airfoil and cascade configuration when $\sigma = 0.428$ and $\sigma = 0.857$ in $\alpha = 20°$ in terms of velocity ratio and surface pressure coefficient which are later discussed in the discussion and results.

The velocity contours show that the low velocity region on the suction side of the blade decreases as σ increases. Comparing the relative pressure contours shows that decreasing in the area of the low velocity region results in decreasing the area of the sub atmospheric region on the blade suction side. The reason is that when a blade is located on top of another one, the flow within the blades gets trapped. This pushes the separation point toward the trailing edge. The flow over the blades becomes more uniform and minifies the area of the low pressure region on the top of the lower blade. However meanwhile the pressure increases on the pressure side but the overall effect is decreases in C_L. Hence increasing σ shifts the separation point from the leading edge to the trailing edge. Hence as the σ is higher, C_L and stall occurs at higher α.

3.2 Applying Modified BEM Theory

As mentioned before in BEM theory power generation of the device should be calculated using both momentum theory and blade element theory. Therefore both calculation methods have been derived.

3.2.1 The modified momentum theory

Figure 2.7 (a) and (b) show the flow expansion when entering PowerWindow in suspended and landed position. These figures show that two stages of blades block the wind entered the PowerWindow. This mechanism is very similar to the counter-rotating HAWTs. Lee, S., et al. [11] showed that in a counter-rotating HAWT the stream tube behind the front rotor and before entering the rear one can be assumed to be fully developed, unless on cases of very closely spaced rotor. Figure 3.7 shows flow model of a counter-rotating HAWT with a rear rotor operating inside the stream tube of the front rotor. As can be seen the flow enters the rear rotor is assumed to be entirely induced by the front rotor.

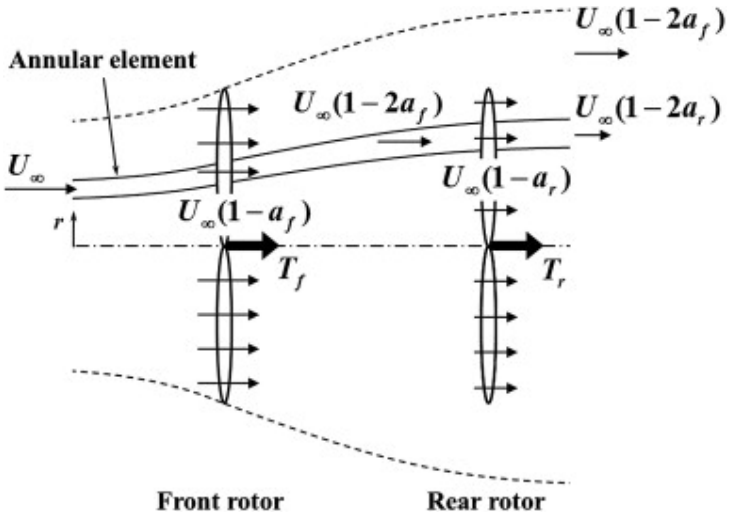

Figure 3-7. Flow model of a counter-rotating HAWT [11].

Distance between the front and rear blades in the PowerWindow prototype is almost equal to the blades cord line. Hence unlike the counter rotating HAWT, the axial stream behind the front rotor and before entering the rear one is assumed to be not developed and air flow cannot expand within two stages. As a result it is assumed

that in Figures 2.7 (a) and (b) $P_4 = P_3$ (also shown in Figure 5.11) and $V_3 = V_4$. In the first flow expansion air velocity reduces from V_1 to V_2 and air pressure increases from P_1 to P_2. This expansion should magnify upstream pressure to create enough pressure-gradient for air to pass through both front and rear blades, so upstream and downstream velocities should decrease with a higher induction factor (a) compared to HAWT to create a higher ultra-atmospheric pressure region at the inlet of the PowerWindow and a lower sub-atmospheric pressure region at its outlet.

Induction factor is the ratio of reduction of the air velocity to that far away from the wind and defined in equation 3.4.

$$a = \frac{V_1 - V_2}{V_1} \tag{3-4}$$

Therefore V_2 and P_2 can be calculated based on V_1 and P_1 using equation 3.5 and 3.6.

$$V_2 = V_1(1 - a) \tag{3-5}$$

$$P_2 = P_1 + \frac{\rho(V_1^2 - V_2^2)}{2} \tag{3-6}$$

Air pressure drops from P_2 to P_3 when the flow passes the front region and from P_4 to P_5 when passes the rear region, while the low distance between the section 2 and 3 and section 4 and 5 does not allow the flow to expand and change its velocity in both stages.

$$P_4 = P_3 \tag{3-7}$$

$$V_5 = V_4 = V_3 = V_2 \tag{3-8}$$

So the power extracted from these regions will be:

$$P_{wind,front} = V_2 A(P_2 - P_3) = V_1 A(1 - a)(P_2 - P_3) \tag{3-9}$$

$$P_{wind,rear} = V_4 A(P_4 - P_5) = V_1 A(1 - a)(P_3 - P_5) \tag{3-10}$$

A shows the swept area of the PowerWindow facing the wind. Adding the power extraction from front and rear regions gives:

$$P_{wind,total} = V_1 A(1-a)(P_2 - P_5) \quad (3\text{-}11)$$

Assuming equal air velocity reduction rates in upstream and downstream of the flow, it can be written:

$$V_6 = V_1(1-2a) \quad (3\text{-}12)$$

$$P_6 = P_5 + \frac{\rho(V_5^2 - V_6^2)}{2} = P_5 + \frac{\rho(V_2^2 - V_6^2)}{2} \quad (3\text{-}13)$$

Therefore:

$$P_{wind,total} = V_1 A(1-a)\left((P_1 + \frac{\rho(V_1^2 - V_2^2)}{2}) - (P_6 - \frac{\rho(V_5^2 - V_6^2)}{2})\right) \quad (3\text{-}14)$$

Since that $P_1 = P_6 = P_{atm}$, it can be written:

$$P_{wind,total} = V_1 A(1-a)\left(\frac{\rho(V_1^2 - V_2^2)}{2} + \frac{\rho(V_5^2 - V_6^2)}{2}\right) \quad (3\text{-}15)$$

Re-writing the velocities in equation 3.15 based on V_1 and a, $P_{wind,total}$ and considering that V_1equals to V_{wind} (wind velocity far from the PowerWindow before entering its inlet region) can be stated as below:

$$P_{wind,total} = \frac{1}{2}\rho A V_{wind}^3 4a(1-a)^2 \quad (3\text{-}16)$$

3.2.2 The Modified Blade Element Theory

Blade element theory is mathematical approach, originally designed for estimation of the propeller's behavior. This method divides a blade into several small elements and calculates the forces on each element. Integrating the forces a along the entire blade and calculating the resulted moments gives the entire torque created over

propeller or rotor [76]. Calculation of the vertical and horizontal forces exerted on the PowerWindow blades is straight forward, since the PowerWindow blades are not twisted and have same shape along the span. The vertical and horizontal forces can be calculated using F_L and F_D from equations 3.1 and 3.2 in equations 3.17 and 3.18.

$$F_x = (F_L sin\beta + F_D cos\beta) \quad (3\text{-}17)$$

$$F_y = (F_L cos\beta - F_D sin\beta) \quad (3\text{-}18)$$

In figure 3.8, β defines the angle between the drag force direction and the horizontal axis and/or between the lift force direction and the vertical axis and α is angle of attack of the wind when facing the blade in any position. Four blade locations of the PowerWindow are shown in Figure 3.8: for front blade, region 1; for rear blade, region 2; for top front blade, region 3; and for top rear blade, region 4 of the PowerWindow. In Figure 8, θ_0 is the design pitch angle of the blades in the region 1 which is reversely repeated in the region 2. θ is the angle of the blades from horizontal axis when canter of the blade is located on the semicircular region, 3 and 4 on the top, which varies with φ (the angle of from the horizontal axis). Equation 3.19 shows the relations between θ and φ and θ_0 in the regions 3 and 4.

$$\theta = \theta_0 \left(1 - \frac{\varphi}{90}\right) + \varphi \quad (3\text{-}19)$$

β (effective angle) and α values depend on θ and φ value in the regions 3 and 4. However β and α values are constant in the regions 1 and 2 and can be calculated based on θ_0. Based on the PowerWindow blade configuration and the gears diameters, minimum zero and maximum two blades can be located in the semicircular region (3 and 4). In the case that two blades are located in this region

one would be in region 3 and the other in the region 4. In the BEM analysis, calculation of the power generation in regions 3 and 4 is more complicated than regions 1 and 2, because as mentioned before the power extracted from these blades is dependent on their orientations (φ).

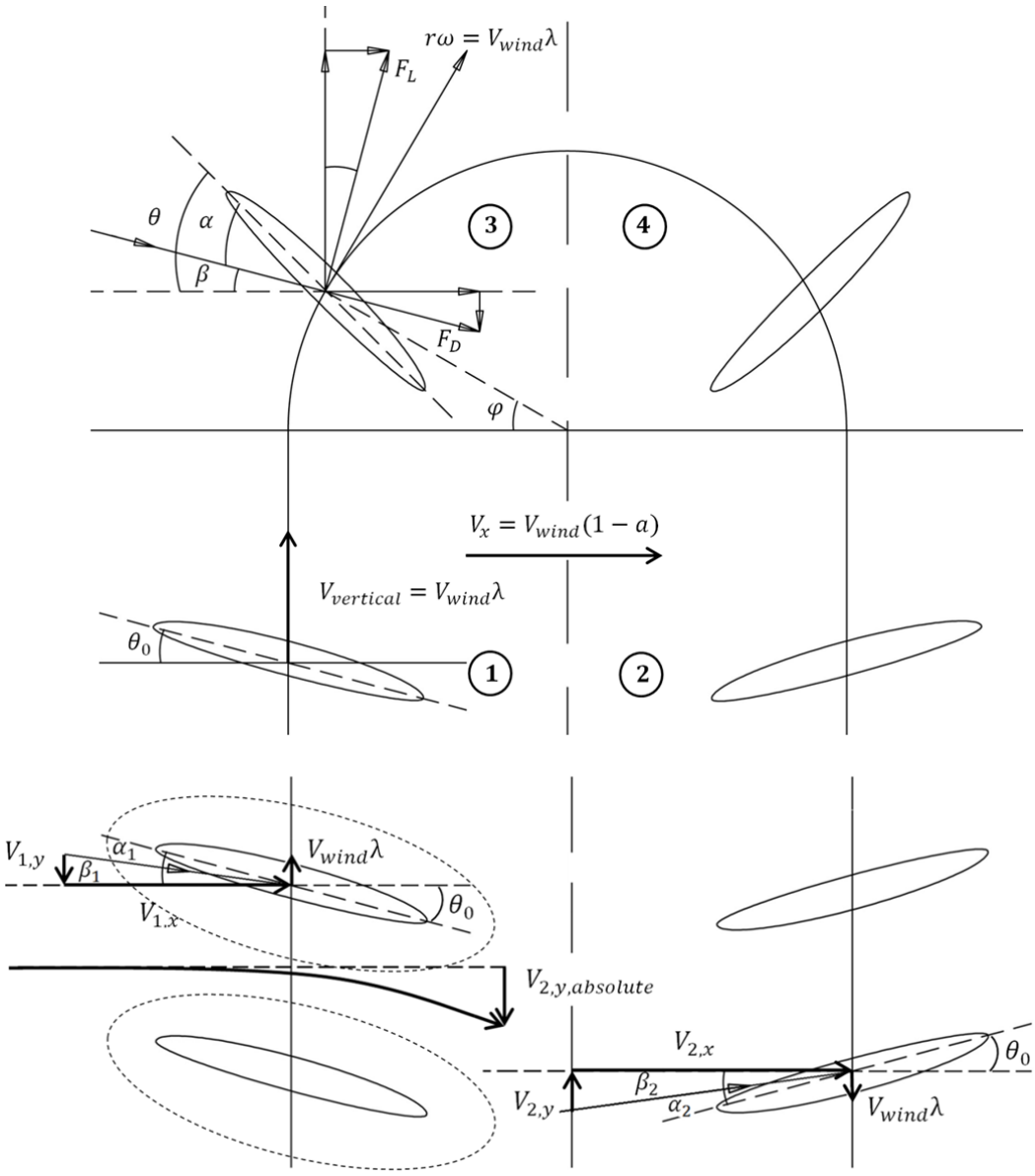

Figure 3-8. Path view followed by the PowerWindow blades in regions 1, 2, 3 and 4, and the velocity composition of the wind facing the front and rear blades which result in the aerodynamic forces acting on the blades.

λ defines the PowerWindow blades absolute velocity (which is also equal to their vertical velocity) to the wind velocity ratio (equation 3.20).

$$\lambda = \frac{V_{blade}}{V_{wind}} = \frac{V_{y,absolute}}{V_{wind}} \quad (3\text{-}20)$$

Considering the PowerWindow blades move vertically in regions 1 and 2, power extracted from them can be calculated by summation of the vertical force exerted on each blade multiplied by its vertical velocity (equation 3.21). The vertical force exerted on the blades (F_y) have been calculated using F_L and F_D in equation 3.17 and 3.18, and vertical velocity of the blades has been calculated from equation 3.20.

$$Power = \sum_1^N \left(\frac{\rho B}{2}\right) {V_{rel}}^2 \, [C_L cos\beta - C_D sin\beta](V_{wind}\lambda) \quad (3\text{-}21)$$

V_{rel} shows relative wind velocity to a blade and can be calculated in equation 3.22 ($i = 1$ for front blades, 2 for rear blades).

$${V_{rel_i}}^2 = {V_{y,relative_i}}^2 + {V_{x,relative_i}}^2 \quad (3\text{-}22)$$

Considering that very low distance between front and rear blades of PowerWindow does not allow wind to expand when passing regions 1 and 2 (in Figure 3.8), its horizontal velocity does not change in the sections 2, 3, 4 and 5 in Figure 2.7 (a) and (b) have same average velocity when facing the front and rear blades. On the other hand the blades have no horizontal velocity through their path in regions 1 and 2. Hence this velocity would be equal to the relative horizontal velocity of the wind to both the front and the rear blades in these regions, which are stated in equation 3.23. But the relative vertical velocity of the wind when facing the rear blades is not equal to the relative vertical velocity of the wind when facing the front blades, because the relative vertical of the wind when facing the rear blades is not

only dependent on their downward vertical velocity, but is also affected by the vertical velocity of the front blades which are moving on the opposite direction and lead the flow upward and also their design angle which lead this flow downward. Hence those have to be calculated separately.

$$V_{1x} = V_{2x} = V_{wind}(1 - a) \tag{3-23}$$

Considering that V_1 in momentum theory equals to V_{wind} (wind velocity far from the PowerWindow before entering its inlet region), air axial velocity affecting the front blades was achieved in equation 3.23 and its tangential velocity equals to the PowerWindow blades absolute velocity which is shown in equation 3.24.

$$\mathrm{V_{1y}} = \lambda \mathrm{V_{wind}} \tag{3-24}$$

By the definition of β and α, β_1 defines the angle between the drag force exerted on the front blades and the horizontal axis (and/or between the lift force exerted on the front blades and the vertical axis) and α_1 is the angle of attack of the wind created the front blades when the design angle is θ_0.These angles are shown in Figure 3.8. Using equations 3.23 and 3.24, β_1 and α_1 can be written as:

$$\beta_1 = tan^{-1}\big(V_{1y}/V_{1x}\big) = tan^{-1}\big(\lambda/(1-a)\big) \tag{3-25}$$

$$\alpha_1 = \theta_0 - tan^{-1}\left(\lambda/(1-a)\right) \tag{3-26}$$

Using the velocities achieved in the equation 3.22, 3.23 and 3.24, and the angles achieved in the equations 3.25 and 3.26 in the equation 3.21 gives equation 3.27 which calculates the power generated by the front blades of the PowerWindow.

$$P_{PW,front} =$$

$$\sum_1^N \left(\frac{\rho B}{2}\right) {V_{wind}}^2 \left((1-a)^2 + \lambda^2\right) \left[C_{L_{\alpha 1}} \cos\left(tan^{-1}\left(\frac{\lambda}{(1-a)}\right)\right) - \right.$$

$$\left. C_{D_{\alpha 1}} \sin\left(tan^{-1}\left(\frac{\lambda}{(1-a)}\right)\right)\right] (\lambda V_{wind}) \qquad (3\text{-}27)$$

Assuming that uniform aerodynamic force is exerted on every blade, the power exerted from the entire front blades can be obtained by simplifying this equation to equation 3.28. The power extracted by each blade is not practically equal ,however this assumption is reasonably acceptable if the PowerWindow is set up in suspended position.

$$P_{PW,front} = N\left(\frac{\rho B}{2}\right) {V_{wind}}^3 \lambda((1-a)^2 + \lambda^2) \begin{bmatrix} C_{L_{\alpha 1}} \cos\left(tan^{-1}\left(\frac{\lambda}{(1-a)}\right)\right) - \\ C_{D_{\alpha 1}} \sin\left(tan^{-1}\left(\frac{\lambda}{(1-a)}\right)\right) \end{bmatrix} \qquad (3\text{-}28)$$

As mentioned before the axial component of the wind velocity affecting the blades in the rear region is equal to the front region (as show in equation 3.23), but its vertical component changes when passing the front blades. Assuming a high σ for the PowerWindow such that the front blades can influence the entire flow passing them, this flow turns upward with the same velocity as the vertical velocity of the front blades and then downwarded with the vertical velocity due to their design angle. Hence the vertical component of the wind velocity in the middle of PowerWindow upstream of the rear blades shown in Figure 3.8 can be calculated as written in equation 3.29.

$$V_{2y,absolute} = \lambda V_{wind} - V_{wind}(1-a)tan\theta_0 = V_{wind}(\lambda - (1-a)tan\theta_0) \qquad (3\text{-}29)$$

Considering that the rear blades also have a downward vertical velocity equal to the upward vertical velocity of the front blades, the relative vertical velocity of the wind facing the rear blades shown in Figure 3.5 can be achieved from equation 3.30.

$$V_{2y} = V_{2y,absolute} + \lambda V_{wind} = V_{wind}(2\lambda - (1-a)tan\theta_0) \quad (3\text{-}30)$$

Considering equations 3.23 and 3.30, β_2 and α_2 shown in Figure 3.9 can be calculated as written in equations 3.31 and 3.32.

$$\beta_2 = tan^{-1}\left(\frac{V_{2y}}{V_{2x}}\right) = tan^{-1}\left(\frac{2\lambda-(1-a)tan\theta_0}{1-a}\right) \quad (3\text{-}31)$$

$$\alpha_2 = \theta_0 - tan^{-1}\left(\frac{(2\lambda-(1-a)tan\theta_0)}{(1-a)}\right) \quad (3\text{-}32)$$

Using the velocities achieved by equation 3.22, 3.23 and 3.30, and the angles of the equations 3.31 and 3.32 in the equation 3.21 gives equation 3.33 which calculates the power generated by the rear blades of the PowerWindow.

$$P_{Pw,rear} =$$

$$\sum_1^N \left(\frac{\rho B}{2}\right) {V_{wind}}^2 ((1-a)^2 + (2\lambda - (1-a)tan\theta)^2)\left[C_{L_{\alpha 2}} cos\left(tan^{-1}\left(\frac{(2\lambda-(1-a)tan\theta_0)}{(1-a)}\right)\right) - C_{D_{\alpha 2}} sin\left(tan^{-1}\left(\frac{(2\lambda-(1-a)tan\theta_0)}{(1-a)}\right)\right)\right](\lambda V_{wind}) \quad (3\text{-}33)$$

Assuming uniform aerodynamic force to be exerted on every blade, the power extracted by each blade would be equal in equation 3.33, and it simplifies this equation to equation 3.34. As mentioned before, although the power extracted from every blade is not practically equal, this assumption is reasonably acceptable if the PowerWindow is set up in suspended position.

$$P_{Pw,rear} =$$

$$N\left(\frac{\rho B}{2}\right) {V_{wind}}^3\, \lambda((1-a)^2 + (2\lambda - (1-a)tan\theta)^2)\left[C_{L_{\alpha 2}} cos\left(tan^{-1}\left(\frac{(2\lambda-(1-a)tan\theta_0)}{(1-a)}\right)\right) - C_{D_{\alpha 2}} sin\left(tan^{-1}\left(\frac{(2\lambda-(1-a)tan\theta_0)}{(1-a)}\right)\right)\right] \quad (3\text{-}34)$$

However if the entire flow passed the front blades and facing the rear blades is not affected by the vertical velocity and design angle of the front blades, equations 3.29-3.32 give different velocity and angles. When σ is very low ($\sigma \ll 1$), or incoming wind velocity is very high or flow is very turbulent, etc. the front blades might only affect the air adjacent to their boundaries. The area within the dashed line in Figure 3.8 shows such an area. In this condition an Affected Flow Ratio (AFR), ε is defined which presents the proportion of the flow affected by the front blades to the entire incoming flow. This changes equations 3.29, 3.30, 3.31 and 3.32 to equations 3.35-3.38.

$$V_{2y,absolute} = \varepsilon V_{wind}(\lambda - (1-a)tan\theta_0) \quad (3\text{-}35)$$

$$V_{2y} = \varepsilon V_{2y,absolute} + \lambda V_{wind} = V_{wind}\big((\varepsilon+1)\lambda - \varepsilon(1-a)tan\theta_0\big) \quad (3\text{-}36)$$

$$\beta_2 = tan^{-1}\left(\frac{V_{2y}}{V_{2x}}\right) = tan^{-1}\left(\frac{\big((\varepsilon+1)\lambda-\varepsilon(1-a)tan\theta_0\big)}{(1-a)}\right) \quad (3\text{-}37)$$

$$\alpha_2 = \theta_0 - tan^{-1}\left(\frac{\big((\varepsilon+1)\lambda-\varepsilon(1-a)tan\theta_0\big)}{(1-a)}\right) \quad (3\text{-}38)$$

Replacing above velocity and angles in equation 3.34 modifies this equation to equation 3.39.

$$P_{Pw,rear} =$$

$$N\left(\frac{\rho B}{2}\right) {V_{wind}}^3 \lambda \left(\begin{matrix} (1-a)^2 + \\ \left((\varepsilon+1)\lambda - \varepsilon(1-a)tan\theta_0\right)^2 \end{matrix} \right) \left[C_{L_{\alpha 2}} cos\left(tan^{-1} \left(\frac{\left((\varepsilon+1)\lambda - \varepsilon(1-a)tan\theta_0\right)}{(1-a)} \right) \right) - \right.$$

$$\left. C_{D_{\alpha 2}} sin\left(tan^{-1} \left(\frac{\left((\varepsilon+1)\lambda - \varepsilon(1-a)tan\theta_0\right)}{(1-a)} \right) \right) \right] \quad (3\text{-}39)$$

Magnitude of ε depends on σ and the incoming wind condition and is needed to be investigated in further studies. However if $1 \geq \sigma$ the flow passed the front blades and facing the rear blades is highly affected by the front blades and it can be assumed that $\varepsilon \cong 1$ and the power captured by the rear blades can be calculated using equation 3.34.

Power generated by each blade of PowerWindow blades when located in regions 3 and 4 can also be calculated by multiplying the linear velocity magnitude of the blade to the force exerted on the blade, parallel to this velocity. Using equations 3.17 and 3.18, Equation 3.40 shows the power generated by the PoweWindow blades when locating at the top/bottom of PoweWindow.

$$Power = \left(\frac{\rho B}{2}\right) {V_{rel}}^2 \left[\begin{matrix} [C_L cos\beta - C_D sin\beta](V_{wind}\lambda cos\varphi) \\ +[C_L sin\beta + C_D cos\beta](V_{wind}\lambda sin\varphi) \end{matrix} \right] \quad (3\text{-}40)$$

The difficulty in calculating power generation of the top/bottom blade via the BEM model is that there are many items (V_{rel}, C_L, C_D, $cos\varphi$ and $sin\varphi$) in Equation 3.40 which are dependent on φ value. Therefore the power generated in those regions is obtained exclusively using CFD simulations. However, the results showed that the power extracted from the top blade when located at its optimum φ value (on the margin of region 3 and 4) might have a considerable (maximum 11%) contribution in the total power generation, but the undesirable force simultaneously exerted on the bottom blade counteracts a significant (70-80%) part of this power generation.

Therefore power generation of the top/bottom bade of PowerWindow has not been further investigated in this study.

3.2.3 Derivation of BEM Formulation

When $\varepsilon \cong 1$ the power captured by the PowerWindow can be calculated by equating the total power with summation of the captured power by the front blades using equation 3.26 and captured power by the rear blades using equation 3.32, which results equation 3.38.

$$\tfrac{1}{2}\rho A V_{\text{wind}}^3 4a(1-a)^2 = B\left(\frac{\rho C}{2}\right) {V_{wind}}^3 \lambda \Bigg[((1-a)^2+\lambda^2)\left[C_{L_{\alpha 1}} \cos(tan^{-1}\lambda) - C_{D_{\alpha 1}} \sin(tan^{-1}\lambda)\right] + ((1-a)^2 + (2\lambda-(1-a)tan\theta)^2)\left[C_{L_{\alpha 2}} cos\left(tan^{-1}\left(\frac{(2\lambda-(1-a)tan\theta_0)}{(1-a)}\right)\right) - C_{D_{\alpha 2}} sin\left(tan^{-1}\left(\frac{(2\lambda-(1-a)tan\theta_0)}{(1-a)}\right)\right)\right]\Bigg] \quad (3\text{-}41)$$

If that $\varepsilon < 1$ equation 3.41 would be modified to equation 3.42.

$$\tfrac{1}{2}\rho A V_{\text{wind}}^3 4a(1-a)^2 = B\left(\frac{\rho C}{2}\right) {V_{wind}}^3 \lambda \Bigg[((1-a)^2+\lambda^2)\left[C_{L_{\alpha 1}} \cos(tan^{-1}\lambda) - C_{D_{\alpha 1}} \sin(tan^{-1}\lambda)\right] + \left((1-a)^2 + \left((\varepsilon+1)\lambda-\varepsilon(1-a)tan\theta_0\right)^2\right)\left[C_{L_{\alpha 2}} cos\left(tan^{-1}\left(\frac{\left((\varepsilon+1)\lambda-\varepsilon(1-a)tan\theta_0\right)}{(1-a)}\right)\right) - C_{D_{\alpha 2}} sin\left(tan^{-1}\left(\frac{\left((\varepsilon+1)\lambda-\varepsilon(1-a)tan\theta_0\right)}{(1-a)}\right)\right)\right]\Bigg] \quad (3\text{-}42)$$

The approach to solving equation 3.41 (or 3.42) is to fix a value for λ and solve the equation to find a in that λ. Once a is achieved, the total power captured by the PowerWindow and its front and rear blades can be achieved using equations 16, 28 and 3.34 (or 3.39) respectively. The considerable point about this model is that as the power exerted from every blade is assumed to be equal, this model can predict the flow mechanism and power captured by the PowerWindow in suspended position, not in landed position. MATLAB is used in this study for solving equation 3.41 (or 3.42), calculating a and its relevant powers in every λ, and plotting them against λ. The λ in which the maximum total power is captured by the PowerWindow, would be its operating condition and that power is ideally its power generation.

Appendix C contains the modified BEM model programed for a PowerWindow prototype configuration (which has been investigated in this study), when 5 blades are located on each side ($N = 5$), each blade and PowerWindow swept area equals 0.3 m^2 and 3.35 m^2 ($B = 0.3\ m.s^{-1}, A = 3.35\ m.s^{-1}$), which results in a solidity of 0.428 ($\sigma = 0.428$), design angle of 18° ($\theta_0 = 12°$), when incoming wind velocity is 8 $m.s^{-1}$($V = 8\ m.s^{-1}$) and AFR is 0.5 ($\varepsilon = 0.5$).

Power extraction by the PowerWindow front and rear blades and the relevant a, α_1 and $\alpha_2$in every λ calculated by the modified BEM model when $\sigma = 0.428$, $\varepsilon = 0.5$ and 1, $\theta_0 = 12°$, 14°, 16° and 18° are reported in the tables in appendix D.

CHAPTER 4. POWERWINDOW COMPUTATIONAL FLUID DYNAMIC MODEL

To assess the validity of the analytical (BEM) model derived for the PowerWindow, a 2D CFD model of the PowerWindow in suspended position has been created. A 2D model of the PowerWindow in landed position has also been created using CFD simulations in Fluent (ANSYS). The modified BEM model cannot predict the flow mechanism and power generation of PowerWindow in landed position, so the result achieved by an experimental test has been compared with CFD results. It should be mentioned that experimental prototyping (with minimum errors) might be very reliable compared to analytical or CFD models, but CFD simulations are much more desirable than experimental prototyping since the time they need and the costs they have are much less. Nevertheless accurate analytical models need practical parameters to express different effects unique to ducted flow.

4.1 Solution Method

The flow over the PowerWindow blades can be subject to significant region of laminar-turbulence transition and the transition process can affect the separation behavior of the boundary layer on the blade surface. Hence selecting an appropriate model for CFD simulation is very important because not every model can predict precisely separation phenomenon. Separation from the blade surface greatly affects the performance of the PowerWindow. SST model has extensively been validated for separating 2D flows with Reynolds-averaged Navier–Stokes (RANS) models [77]. Menter, F.R. [78] showed the SST model outperformed the 4-equation, v2-f (transition SST) model in velocity profiles separation prediction for the NACA 4412 airfoil case. El-Behery, S.M. and M.H. Hamed [79] compared the SST, 7-eqation

Reynolds stress model (RSM), v2-f andlow-Re k-ε models using the Buice, C.U. and J.K. Eaton [80] data for an asymmetric planar diffuser. The v2-f model gave the best prediction of the separation point. Menter, F.R. [78] suggested that flow over the rotor blades can be subject to significant region of laminar-turbulence transition and because the transition process can affect the separation behavior of the boundary layer on the blade surface, it is agreed that the v2-f model is the best model in case of separation. Therefore v2-f model is selected and used for this study.

4.2 Mesh Structure, Quality and Boundary Conditions

Reliability of the CFD result is dependent on the mesh structure and quality, and also setting appropriate boundary conditions which are discussed in this study.

4.2.1 Mesh Structure

Higher mesh quality is mostly achievable using finer and structured mesh. The number of grids are higher, the simulations speed is slower. In order to make a balance between solution accuracy and calculation time, a combination of structured and unstructured mesh was used. Although structured mesh is the preferred; it is difficult to generate a high quality structured mesh in the entire domain. This technique assists to decreasing number of grid while having a high quality mesh around the body [66]. Therefore rows of very fine structured rectangular grids were generated adjacent to the blade surface as shown in Figure 4.1 (c). The optimum number of these grids is investigated later. This structured region was connected to the structured regions via unstructured triangular grids as shown in Figure 4.1 (b) structured coarser mesh was used around this region in the entire domain which can be seen in this Figure 4.1 (a). Gambit is used for mesh generation in this study.

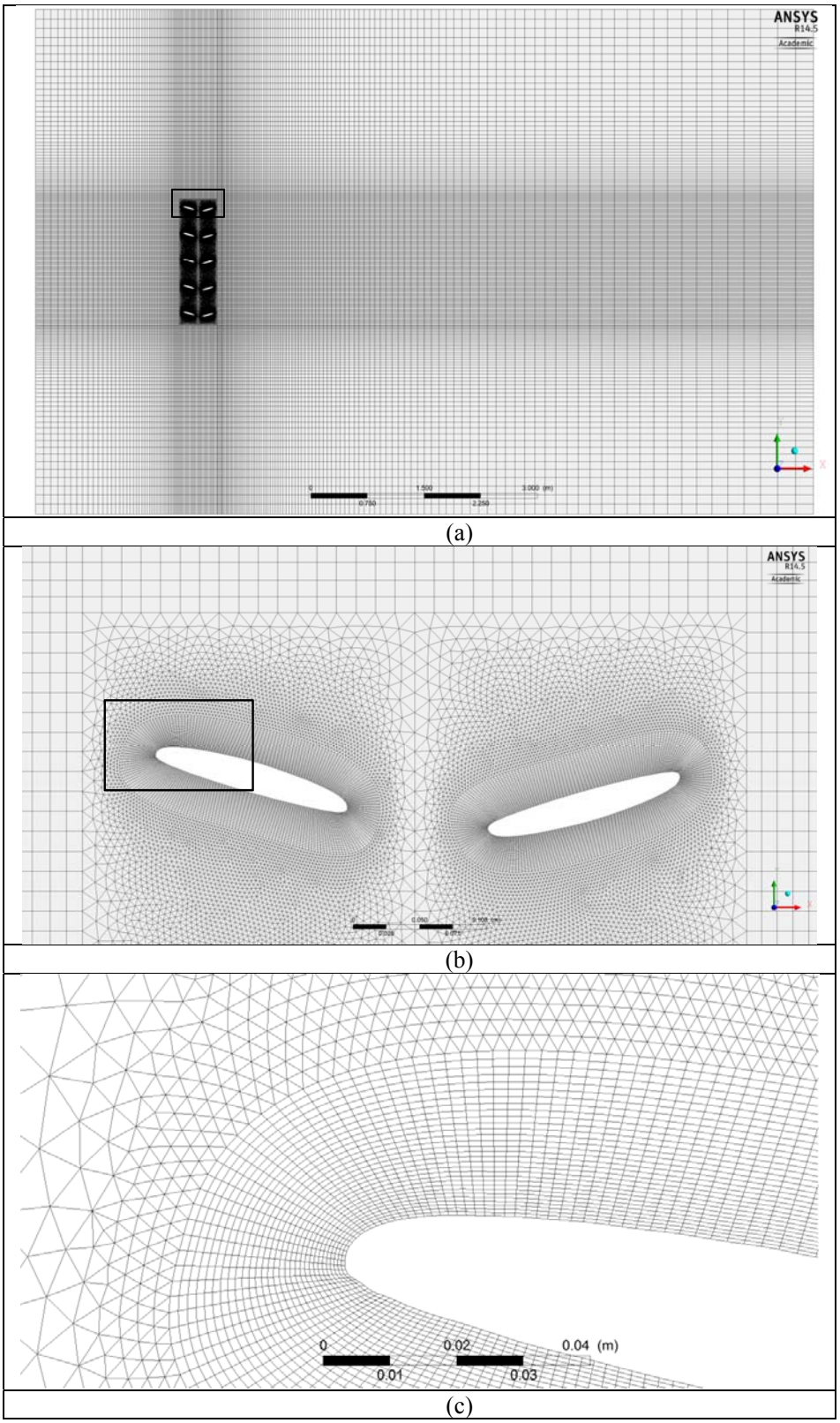

Figure 4-1 (a). Structured mesh generated around the unstructured region in the entire domain. (b). Combination of structured and unstructured mesh around the blades. (c). Very fine structured rectangular grids adjacent to the blade surface.

4.2.2 Mesh Independence Study

As mentioned before, increasing the number of grids results in decreasing solution speed. Hence there is a challenge in mesh generation between mesh quality (using finer grids) and simulation speed (using coarser grids). Mesh independence study assists to find the optimum grid structure over object boundaries. In this study the mesh quality around the PowerWindow airfoil has been increased in three steps. 50 cells (6 mm) were initially generated around each blade. This number is increased to 100 (3 mm), 200 (1.5 mm) and 400 (0.75 mm) in the next steps. Figure 4.2 (a), (b),(c), and (d) shows the grid structure and size around the airfoil in each step.

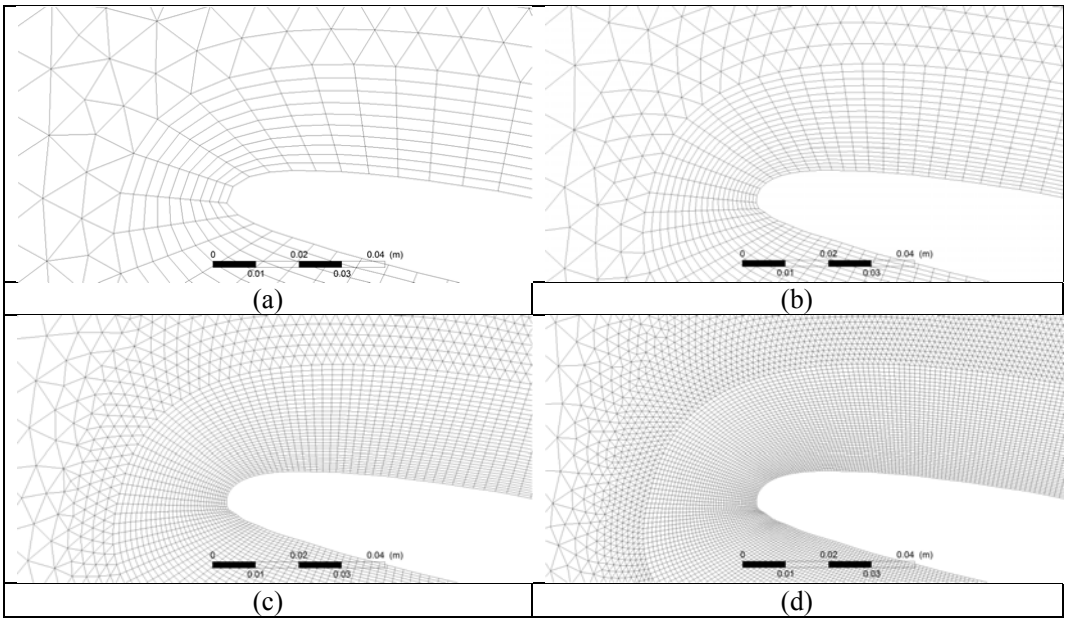

Figure 4-2. Mesh generated around the PowerWindow airfoil with (a) 50 cells, (b) 100 cells, (c) 200 cells and (d) 400 cells.

The main purpose of this part of mesh independence study is to investigate the effect of mesh quality on the result of the simulations, regardless of their consistency with the experimental or analytical models. Therefore the pressure distribution is investigated on the PowerWindow blades in this study. Figure 4.3 shows pressure

value created over one PowerWindow blade with different number of mesh grids over its boundary. This figure shows that the mesh with 50 and 100 cells on the blades are not reliable enough as the results are very far from the results achieved with 200 and 400 cells, while the result achieved by 200 cells is very close to 400 cells. This means that increasing the numbre of grids on the blades further than 200 does not improve the simulation results significantly. Hence using such a mesh structure preserves the result accuracy while saves its the calculation time.

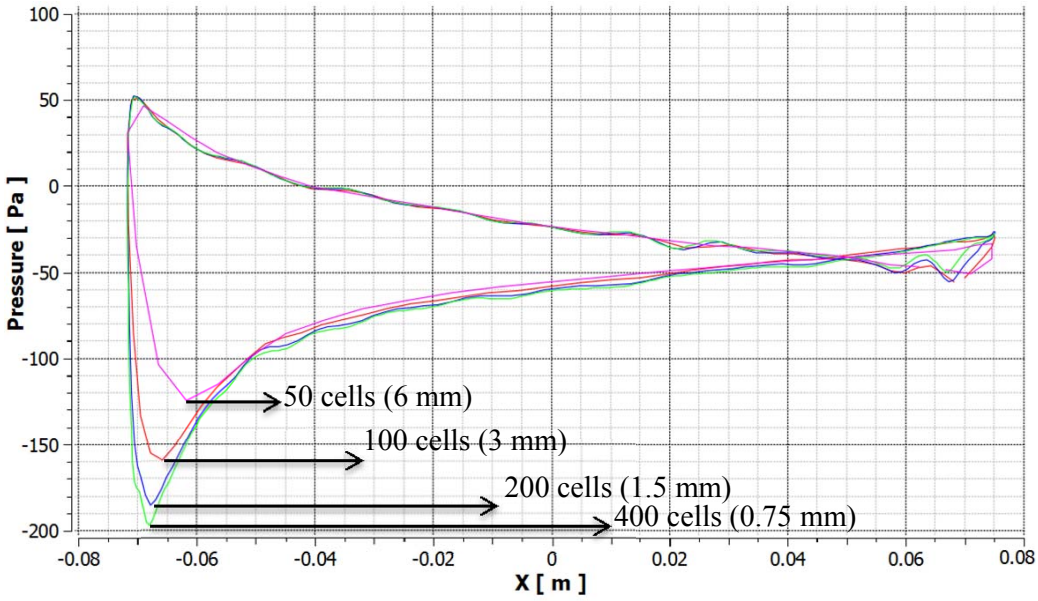

Figure 4-3. pressure created over PowerWindow airfoil when surrounded by different number of cells.

Appendix E contains figures showing (a) the mesh generated around the front, bottom blade of PowerWindow, (b); the pressure counturs around this blade (c); and the pressure created over the five front blades of PowerWindow along their cords.

4.2.3 Boundary Conditions

The frame of the hybrid region containing the front and rear blades were set as Multiple Reference Frame (MRF). MRF computational method is a steady-state approximation. In this method individual cell zone s can move with different rotational and/or translational speeds. Interfaces are defined between cell zones of a local reference frame and the adjacent cell zones to enable computing (interpolating) flow variables in between them. In the MRF approach relative motion of a moving zone is not accounted respecting the adjacent zones (moving or stationary); but the grid are fixed for the computation. Fluent enforces the continuity of the absolute velocity at the interfaces between two cell zones.

In the PW CFD model, the inlet boundary condition is constant free stream velocity of $8m.s^{-1}$ and outlet boundary is set to atmospheric pressure. The top and bottom wall were set as stationary walls for the landed PowerWindow, but moving wall with the same velocity as incoming wind for the suspended PowerWindow. This condition assists to create more uniform flow (as expected in practice) over the PowerWindow blades in suspended position, since as shown in Figure 4.4 (a) and (b), boundary layers of the stationary walls at the top and bottom of the wind tunnel create a non-uniform flow over the PowerWindow blades. The dashed line shows the uniform flow in the simulated wind tunnel which can be achieved by setting moving walls with the same velocity as incoming wind.

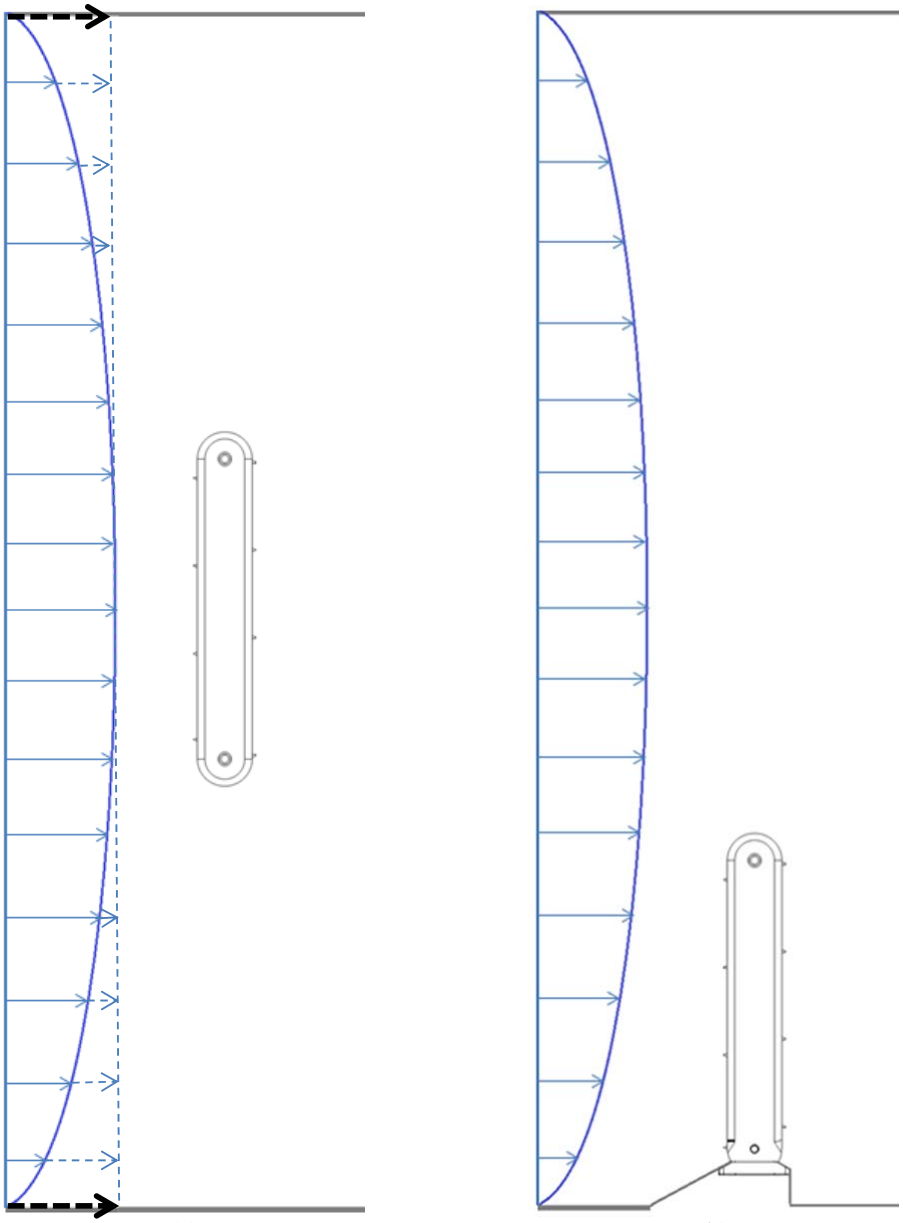

(a) (b)

Figure 4-4. Non-uniform flow due to boundary layers of the stationary walls at top and bottom of the wind tunnel over PowerWindow in (a). suspended and (b). landed position.

CHAPTER 5. RESULTS AND DISCUSSION

The modified BEM model obtained in this study might be the best tool to analyze and enhance the performance of PowerWindow in further studies. Effect of solidity and design angle on the performance of PowerWindow is investigated and discussed using this model in this study.

However, in a prior step, the modified BEM model is used to investigate its validity by comparing its results with the ones obtained by CFD and experimental model. Hence PowerWindow efficiency is also investigated in term of coefficient of performance (C_P) using all three approaches and been compared in this study. C_P shows the ratio of the power captured by the generator to the entire wind energy passing through its swept area. Equation 5.1 gives C_P definition.

$$C_P = \frac{P_{measured}}{P_{wind}} = \frac{T\omega}{0.5\rho AU^3} \quad (5\text{-}1)$$

5.1 Coefficient of Performance by BEM, CFD and Experimental Model

Power generation of PowerWindow, operating in suspended and landed position achieved by BEM, CFD and experimental model has been investigated in this part in term of C_P in order to: (i) validate its CFD results by the BEM results in suspended position; (ii) verify its CFD results by the experimental result in landed position; and also (iii) find the flow mechanism and power generation of the PowerWindow front and rear blades in those positions.

5.1.1 Suspended Position

Figures 5.1 (a) and (b) (extracted from Tables D.1-D.8 in appendix D) show a calculated by the modified BEM model of the suspended PowerWindow when $\sigma = 0.428$ against λ when $\theta_0 = 12°, 14°, 16°$ and $18°$. Figure 5.1 (a), shows a, calculated with $\varepsilon = 0.5$ and Figure 5.1 (b) shows a, calculated with $\varepsilon = 1.0$.

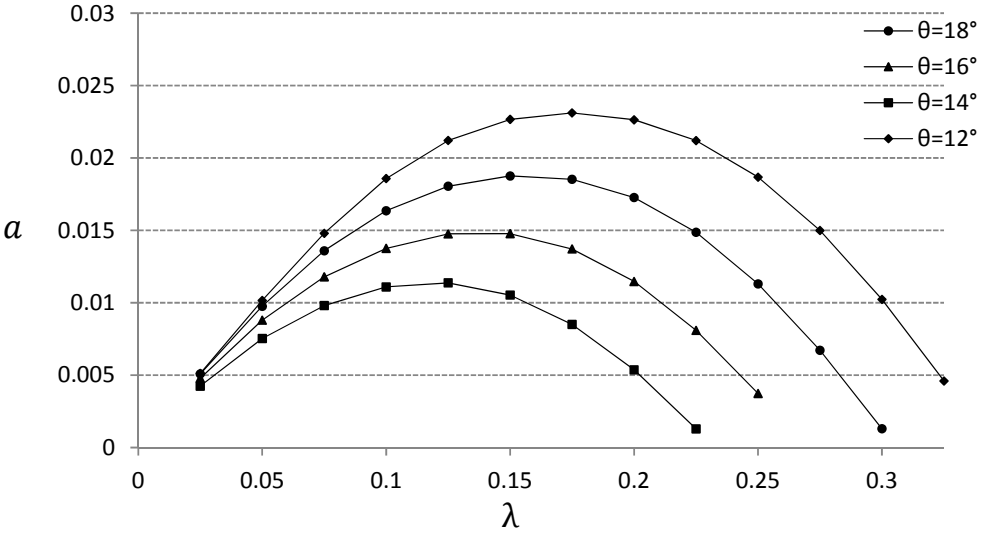

(a)

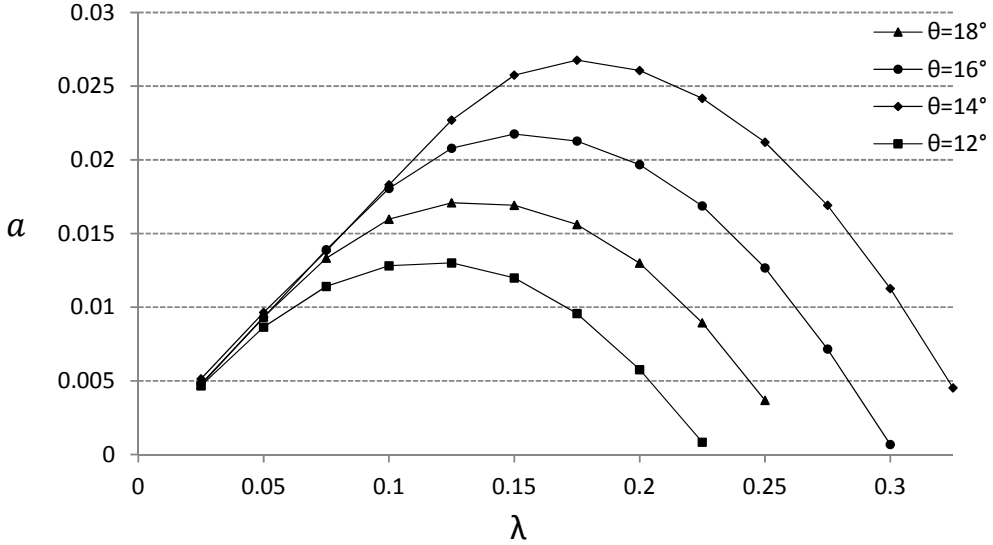

(b)

Figure 5-1. a calculated by the modified BEM model of the suspended PowerWindow when $\sigma = 0.428$ against λ when $\theta_0 = 12°, 14°, 16°$ and $18°$ when (a) $\varepsilon = 0.5$ and (b) $\varepsilon = 1.0$.

Both Figures 5.1 (a) and (b) show that there is a maximum a for each θ_0 which increases and occurs in higher λ by increasing θ_0. Considering equations 2.15 and 3.5, the maximum power generation occurs when $a = 1/3 \approx 0.33$, which results in $C_P = 59\%$ (Betz limit). Since the maximum a achieved in these operating conditions is $a = 0.175$ (belongs to $\theta_0 = 18°$), the C_P is not expected to be very high. However this shows that increasing θ_0 may assist to optimize PowerWindow efficiency. This is more investigated later in this study.

Comparing Figures 5.1 (a) and (b) also shows that when $\varepsilon = 1.0$, higher a is predicted by the modified BEM model rather than to when $\varepsilon = 0.5$. Moreover as mentioned before, as σ is higher ε is closer to 1.0. This shows that increasing σ may assist to optimize PowerWindow efficiency. This is also more investigated later in this study.

Figures 5.2 (a), (b), (c) and (d) show the power captured by the suspended PowerWindow in term of C_P when $\sigma = 0.428$ against λ when $\theta_0 = 12°, 14°, 16°$ and 18° achieved by BEM and CFD models. Since the exact value of ε has not been investigated in this study, C_P of the suspended PowerWindow achieved by BEM is plotted once when $\varepsilon = 1.0$, and once when $\varepsilon = 0.5$. However the exact value of ε is needed to be found based on incoming wind velocity, operating λ and the σ of PowerWindow in further studies. It should be mentioned that P_front, P_rear and P_total refer to the power generated by the front blades, rear blades and the total power captured by PowerWindow. These figures show that the power generation achieved by the CFD models, are within the range predicted by the modified BEM model.

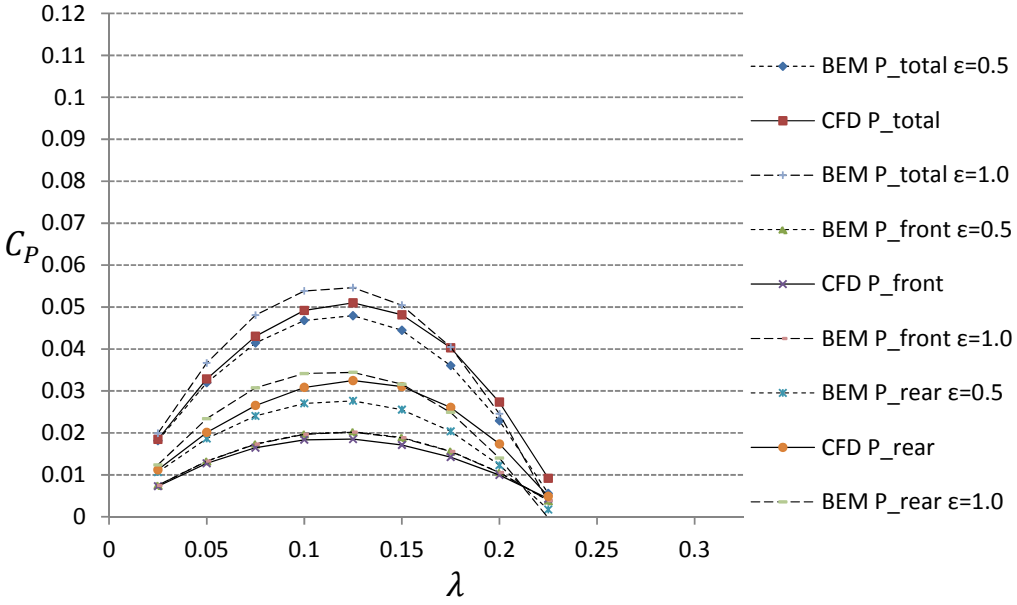
0.12
0.11
0.1
0.09
0.08
0.07
0.06
0.05
0.04
0.03
0.02
0.01
0
C_P
0
0.05
0.1
0.15
0.2
0.25
0.3
λ
BEM P_total ε=0.5
CFD P_total
BEM P_total ε=1.0
BEM P_front ε=0.5
CFD P_front
BEM P_front ε=1.0
BEM P_rear ε=0.5
CFD P_rear
BEM P_rear ε=1.0

(a)

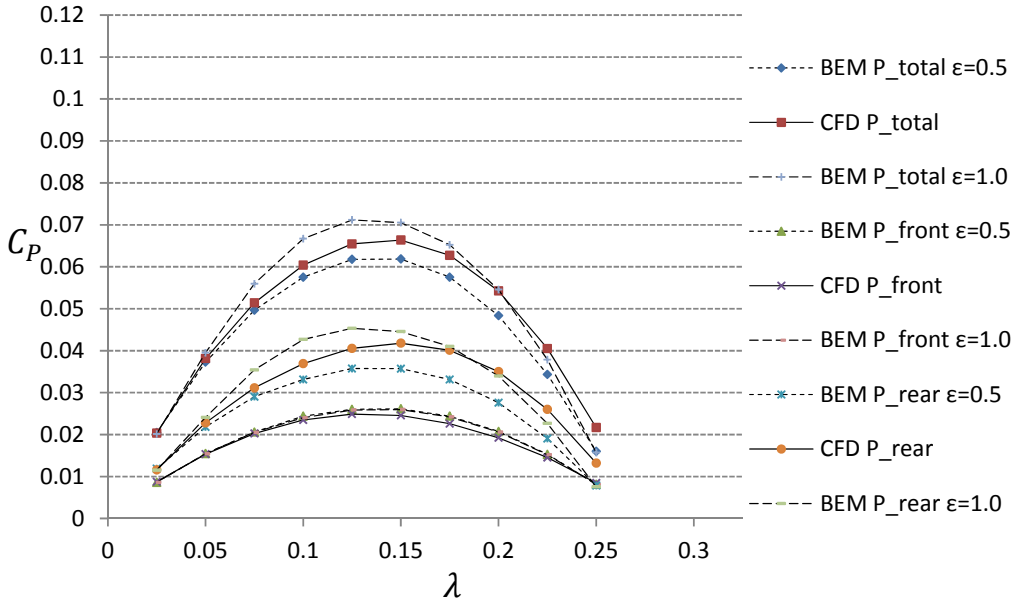
0.12
0.11
0.1
0.09
0.08
0.07
0.06
0.05
0.04
0.03
0.02
0.01
0
C_P
0
0.05
0.1
0.15
0.2
0.25
0.3
λ
BEM P_total ε=0.5
CFD P_total
BEM P_total ε=1.0
BEM P_front ε=0.5
CFD P_front
BEM P_front ε=1.0
BEM P_rear ε=0.5
CFD P_rear
BEM P_rear ε=1.0

(b)

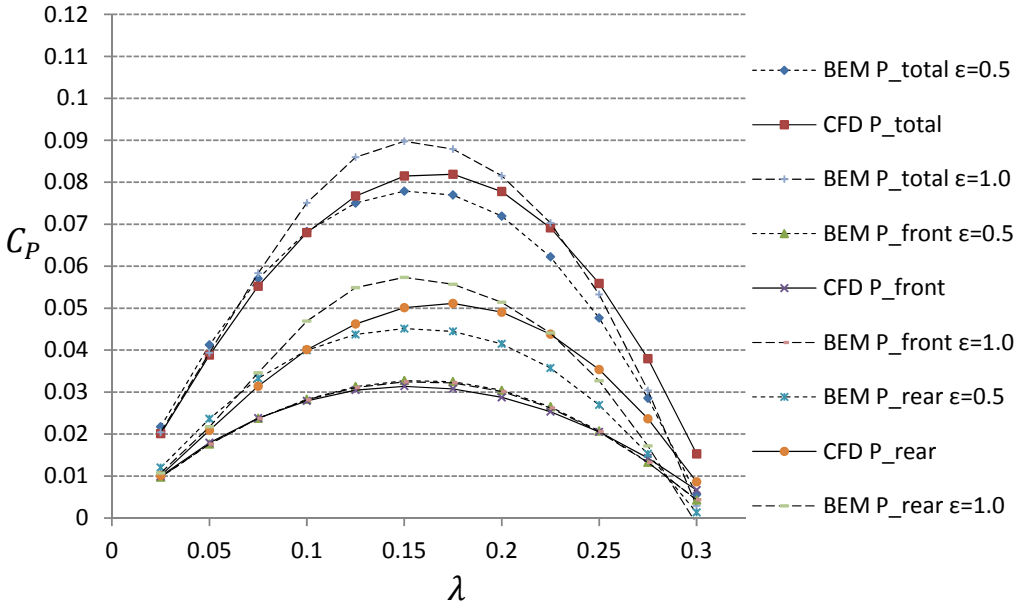

(c)

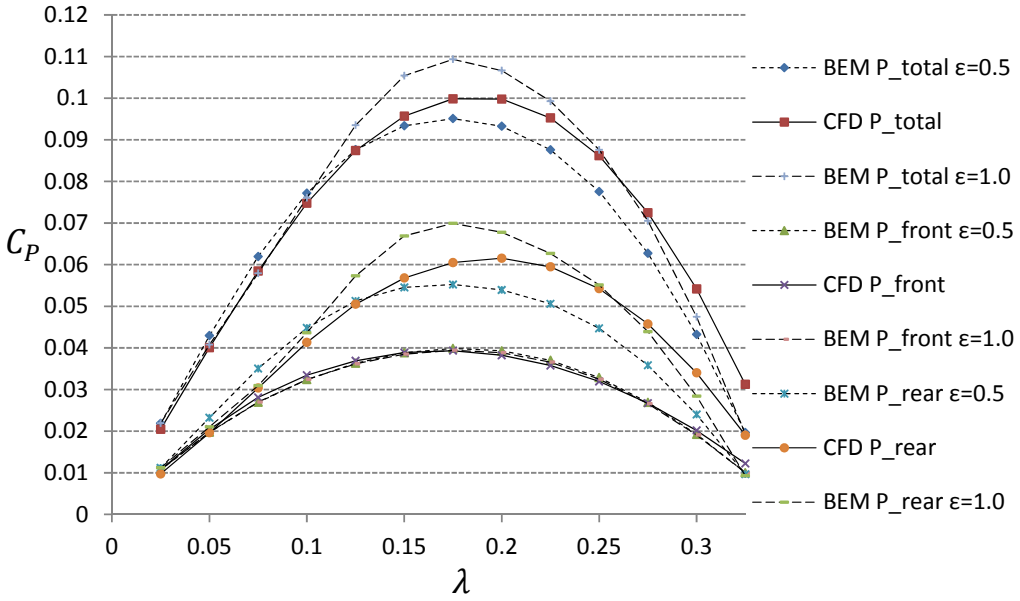

(d)

Figure 5-2. C_P of PowerWindow in suspended position in an ideal wind tunnel when $\sigma = 0.428$ against λ when (a).$\theta_0 = 12°$, (b). $\theta_0 = 14°$, (c). $\theta_0 = 16°$, and (d). $\theta_0 = 18°$ using BEM and CFD models.

Figures 5.2 (a), (b), (c) and (d) show that both BEM and CFD model agrees that the power captured by the rear blades is greater than the front blades in the major range of λ. Comparing equations 3.26 and 3.32 (or 3.38 when $\varepsilon \neq 1$) shows that $\alpha_2$is higher than $\alpha_1$when $\lambda < (1 - a)\tan\theta_0$. Although there is a limited range in which $\alpha_2$is higher than α_1, BEM results shows that in these configurations and operating λ, $\alpha_2$is higher than $\alpha_1$and they both are between $0°$ and $20°$ ($0° < \alpha_1 < \alpha_2 < 20°$). The reason is that the vertical velocity of the flow increases when passes the front blades and creates a higher α over the rear blades. Figure 3.6 (a) shows that for $0° < \alpha < 20°$, increase in α results in increase in C_L. Hence vertical force exerted on the rear blades, and consequently their power generation are expected to be greater than the front blades. As a result the front blades assist the rear blade to capture greater power.

Lee et al. [11] showed that using a counter rotating rotor in the counter rotating HAWTs enhances the C_P, but not in every design condition. For example using a counter rotating rotor with the same radius, rotating speed and pitch as the front one behind it, has decreased C_P from 0.448 (C_P of the relative single rotor) to 0.445, but by optimizing the pitch difference between the front and rear blades, C_P has increased to 0.457. Similar optimization can also be done on the PowerWindow by creating a design angle difference between its front and rear blades in further studies. Although C_P of the counter rotating HAWT was not significantly greater than its single rotor, this design is considerably more efficient than a single rotor design, because two turbines have been installed on one structure and operating with a slightly higher C_P in this design.

A major difference in C_P calculation of the PowerWindow and counter rotating HAWT is that in the counter rotating HAWT, C_P shows the ratio of the total power captured by the front and rear rotor to their total swept area, but in the PowerWindow, C_P shows the ratio of the total power captured by the front and rear rotor to their common swept area. Because as mentioned before, in the counter rotating HAWT, the downstream flow of the front rotor would be fully developed before reaching its rear rotor inlet, while in PowerWindow, power is assumed to be extracted during one flow expansion and deceleration.

Another point which Figures 5.2 (a), (b), (c) and (d) show is that an advantage of PowerWindow is that it can operate with a 0.11 efficiency in very low linear velocity ratios ($0.1< \lambda < 0.2$) which is not achievable with conventional wind turbines. It can also be seen that increasing θ_0 results in greater power extraction from the PowerWindow and shifts the optimum λ (the operation point) to higher values. Equations 3.26 and 3.32 (or 3.38 when $\varepsilon \neq 1$) show that increasing θ_0 generally increases α and as discussed before increasing α results in increasing the lift force exerted on the blades and capturing greater power from wind energy. This shows that performance of the PowerWindow is greatly affected by θ_0 which can be increased and optimized in further studies.

5.1.2 Landed Position

As mentioned before, BEM model cannot predict the flow mechanism and power generation of PowerWindow in landed position, because the aerodynamic forces exerted on the PowerWindow blades are very non uniform in this position. Nevertheless the PowerWindow prototype (configured in $\sigma = 0.428$ and $\theta_0 = 16$)

has been experimentally tested in landed position, the measured data compared to CFD simulation results. As shown in Figure 5.3 (a) the prototype is placed on the ground in a wind tunnel and a small ramp is embedded at its inlet bottom which helps to accelerate overall magnitude and increase vertical component of wind when entering PowerWindow. Wind velocity is $8\,m.s^{-1}$ in the wind tunnel. The power generated in the generators has been recorded against time and shown in Figure 5.3 (b). As can be seen the maximum power generated by PowerWindow with this configuration is around $140\,W$ which results in $C_P = 0.1467$. Linear velocity of the PowerWindow blades has been measured within $1.5\,m.s^{-1}$ and $2.0\,m.s^{-1}$ in this condition which results in $0.1875 < \lambda < 0.25$. It should be mentioned that the total captured power is greater than this since some power will always be wasted due to transmission loss.

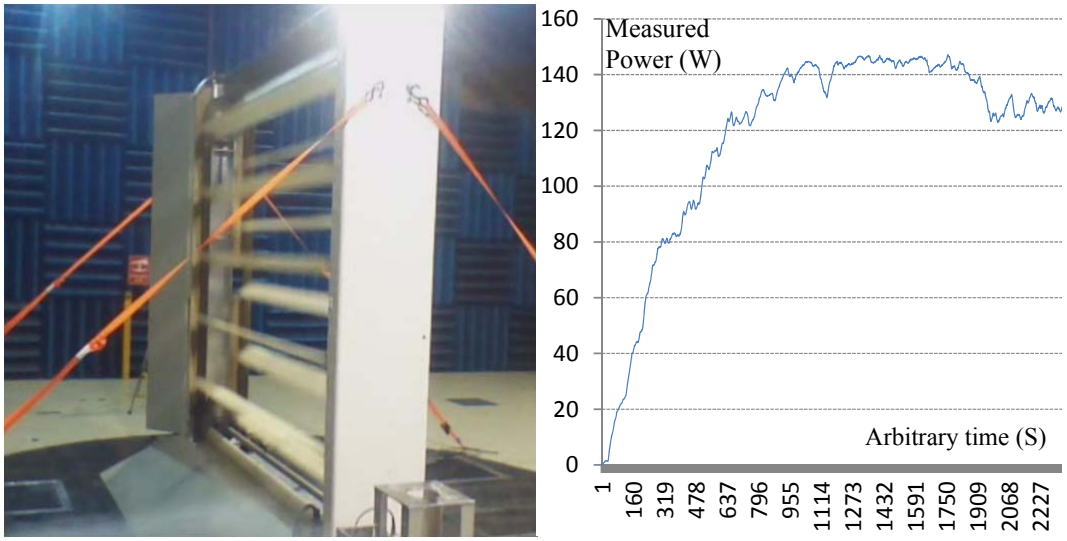

(a) (b)

Figure 5-3 (a). Prototype of the PowerWindow operating in landed position when $\sigma = 0.428$ and $\theta_0 = 16$ in wind tunnel, and (b) its power generator recorded results against time.

For coordinating the CFD model boundary conditions to the PowerWindow prototype, its CFD model was located in landed position in the wind tunnel and a

small ramp was embedded at its inlet bottom. The top and bottom walls were also set to stationary walls. The rest of the variables in this CFD model were exactly similar to the CFD model of the suspended PowerWindow generated for the BEM model. Figures 5.4 shows the total power captured by the PowerWindow prototype (when $\theta_0 = 16°$) and the landed PowerWindow achieved by the CFD model when $\theta_0 = 12°, 14°, 16°$and 18° and $\sigma = 0.428$ in term of C_P against λ. The reason for investigating C_P in $\theta_0 = 14°, 16°$and 18° is that although in the prototype $\theta_0 = 16°$, it was seen that the prototype belts where slightly bent due to the wind axial force during the experimental test, which should have created a slight deviation in θ_0 when transferring the blades from bottom to top and vice versa.

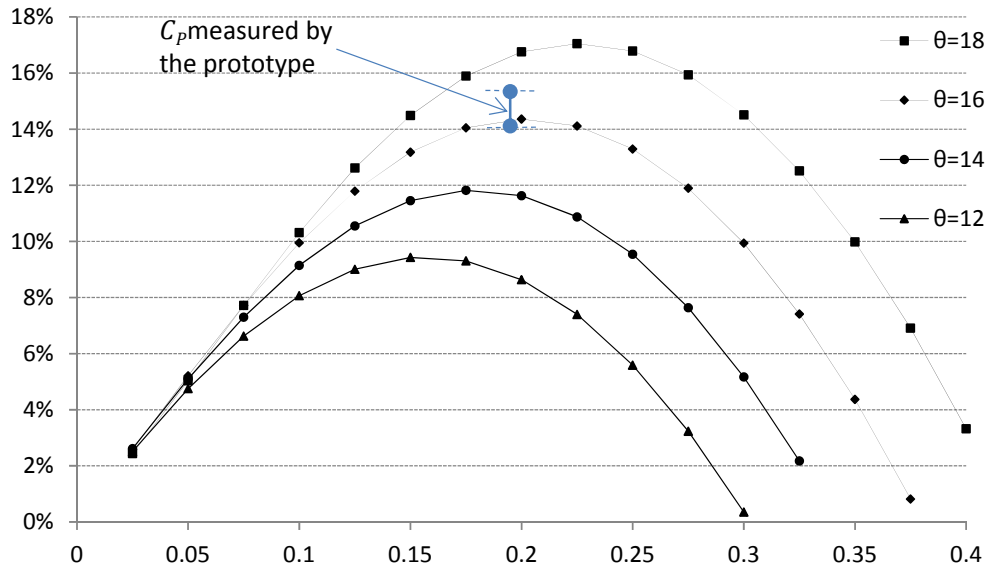

Figure 5-4. C_P of the PowerWindow prototype (when $\theta_0 = 16°$) and the landed PowerWindow achieved by the CFD model when $\theta_0 = 14°, 16°$and 18°and $\sigma = 0.428$ against λ.

Figure 5.4 shows that the operating λ and the maximum C_P of the PowerWindow prototype is very close to the values expected by the CFD model (when $\theta_0 = 16°$), which assists to validated the results obtained by the CFD model. Comparing Figure

5.4 and Figures 5.2 (b), (c) and (d) also shows that a greater C_P (50-70%) is acheived by the PowerWindow in landed position rather than suspended position. The reason is discussed later.

5.2 Effect of Installation Configuration on the Coefficient of Performance

Comparing Figure 5.4 and Figures 5.2 (b), (c) and (d) shows that C_P of the PowerWindow has increased from 0.065, 0.08 and 0.1 in suspended position to 0.12, 0.14 and 0.17 in landed position, which means that the performance of the PowerWindow installed in the landed position (in this boundary and operating conditions) is around 70% higher than the same PowerWindow installed in the suspended position. Figure 5.5 (a), (b), (c) and (d) show the power captured by the suspended and landed PowerWindow in term of C_P when $\sigma = 0.428$ against λ when $\theta_0 = 12°, 14°, 16°$and $18°$ achieved by the CFD models. In these figures P_Suspended_front, P_Suspended_rear and P_Suspended_total refer to the power generated by the front blades, rear blades and the total power captured by the suspended PowerWindow and P_Landed_front, P_Landed_rear and P_Landed_total refer to the power generated by the front blades, rear blades and the total power captured by the landed PowerWindow.

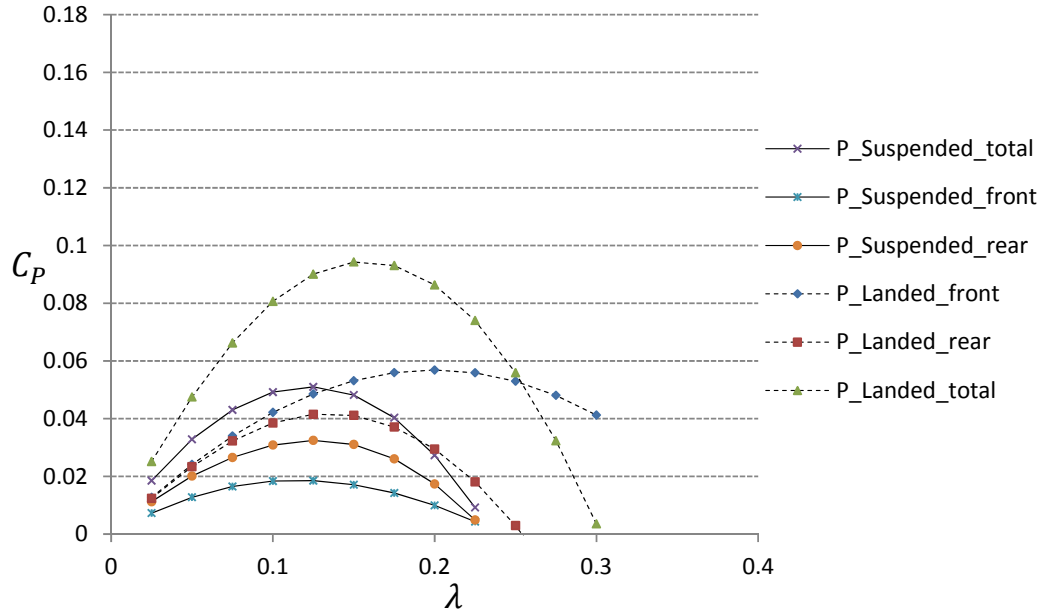
0.18
0.16
0.14
0.12
0.1
0.08
0.06
0.04
0.02
0
C_P
0
0.1
0.2
0.3
0.4
λ
P_Suspended_total
P_Suspended_front
P_Suspended_rear
P_Landed_front
P_Landed_rear
P_Landed_total

(a)

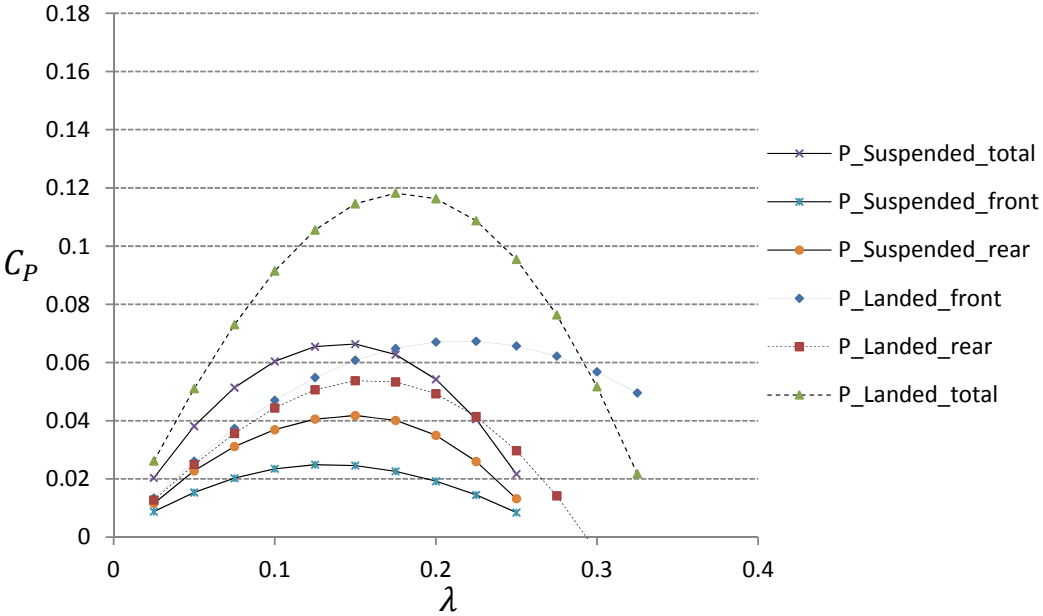
0.18
0.16
0.14
0.12
0.1
0.08
0.06
0.04
0.02
0
C_P
0
0.1
0.2
0.3
0.4
λ
P_Suspended_total
P_Suspended_front
P_Suspended_rear
P_Landed_front
P_Landed_rear
P_Landed_total

(b)

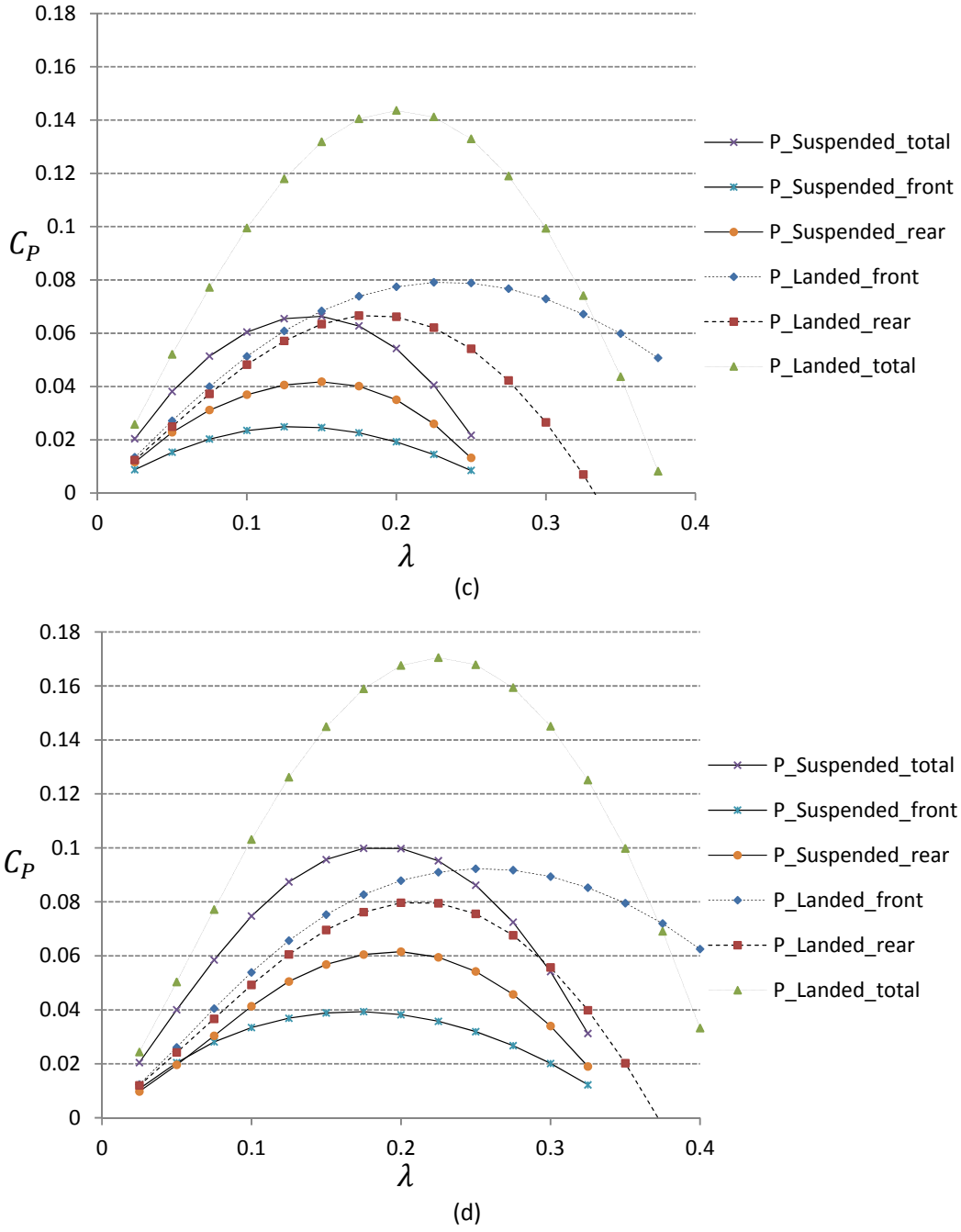

Figure 5-5. C_P of the PowerWindow in suspended and landed position when $\sigma = 0.428$ against λ when (a).$\theta_0 = 12°$, (b). $\theta_0 = 14°$, (c). $\theta_0 = 16°$, and (d). $\theta_0 = 18°$ obtained by the CFD models.

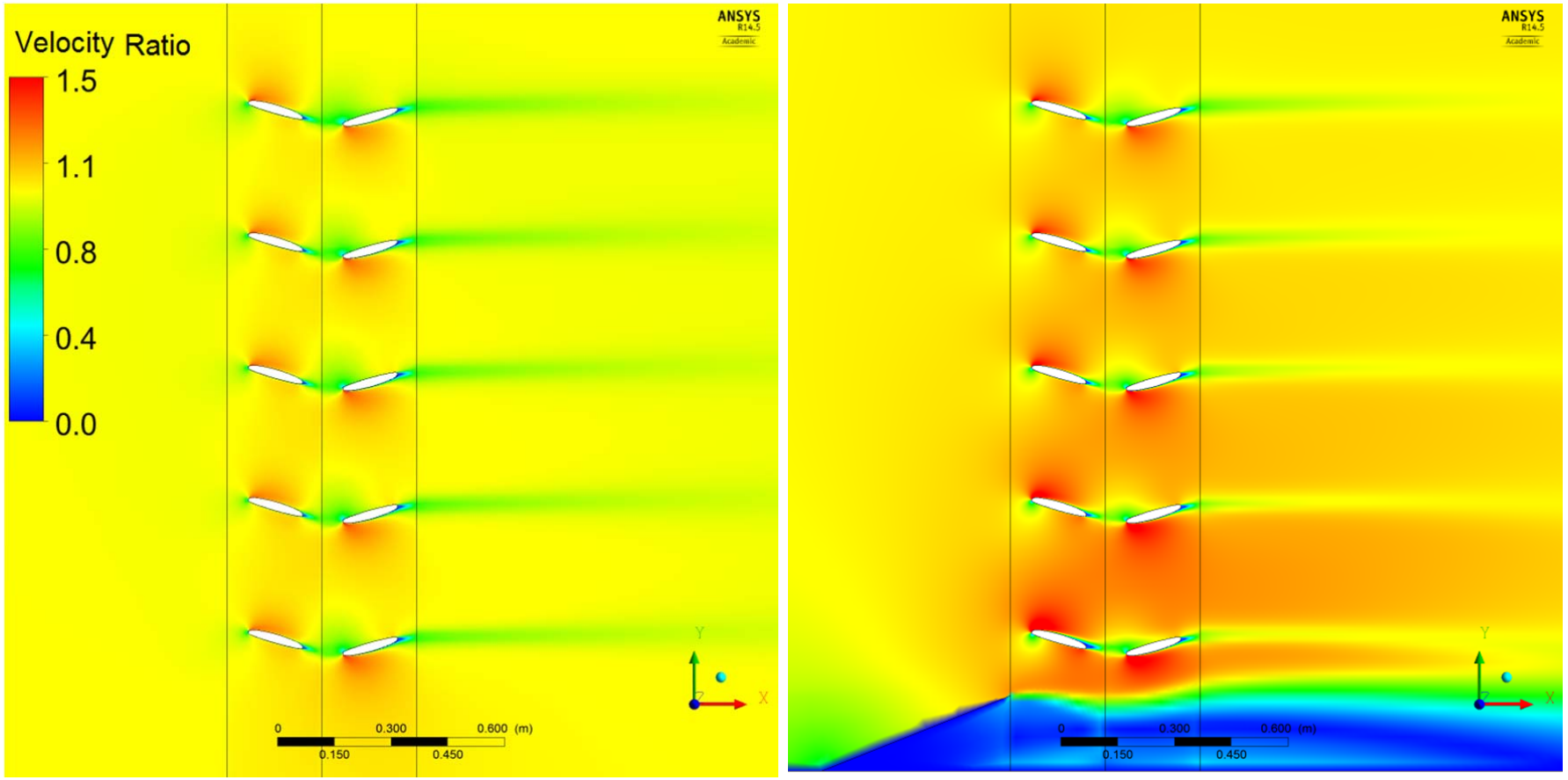

(a) (b)

Figure 5-6. R_V contours of the wind passing (a) the suspended PowerWindow and (b) the landed PowerWindow, with the ramp located at its inlet bottom ($\sigma = 0.428$ and $\theta_0 = 16°$)

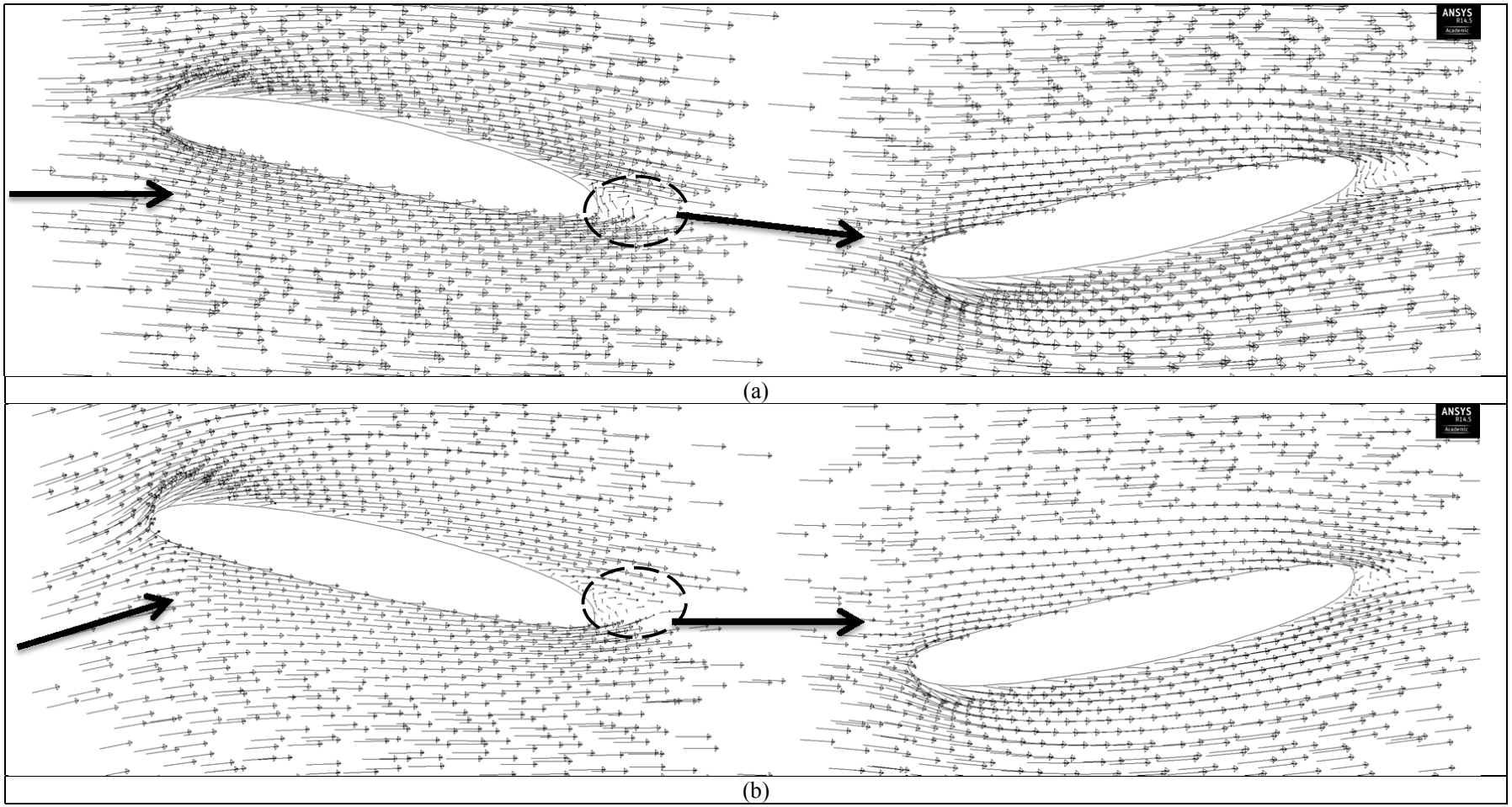

Figure 5-7. Velocity vectors around (a) suspended; and (b) landed PowerWindow bottom blades when $\sigma = 0.428$ and $\theta_0 = 12°$

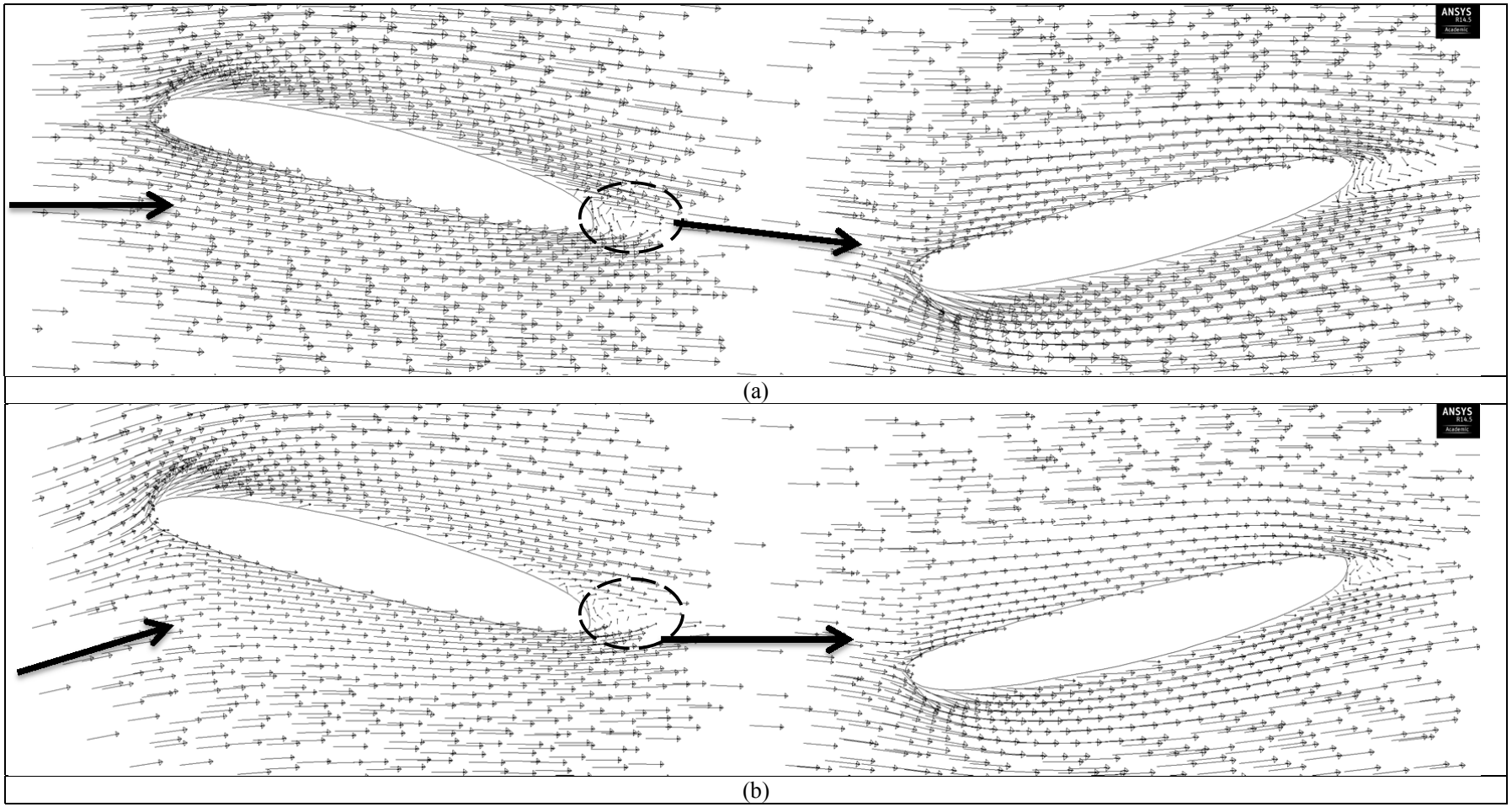

Figure 5-8. Velocity vectors around (a) suspended; and (b) landed PowerWindow bottom blades when $\sigma = 0.428$ and $\theta_0 = 14°$

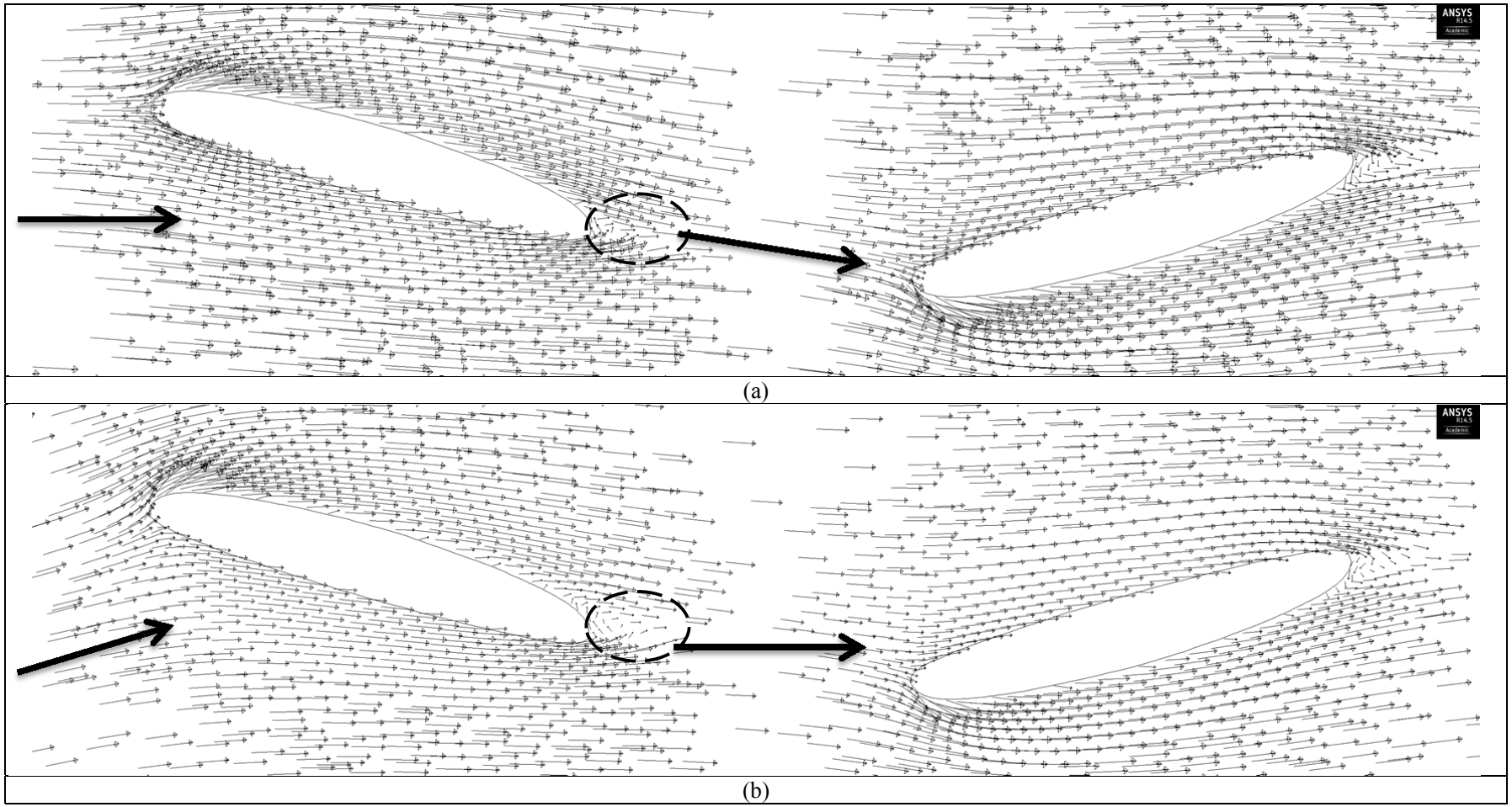

Figure 5-9. Velocity vectors around (a) suspended; and (b) landed PowerWindow bottom blades when $\sigma = 0.428$ and $\theta_0 = 16°$

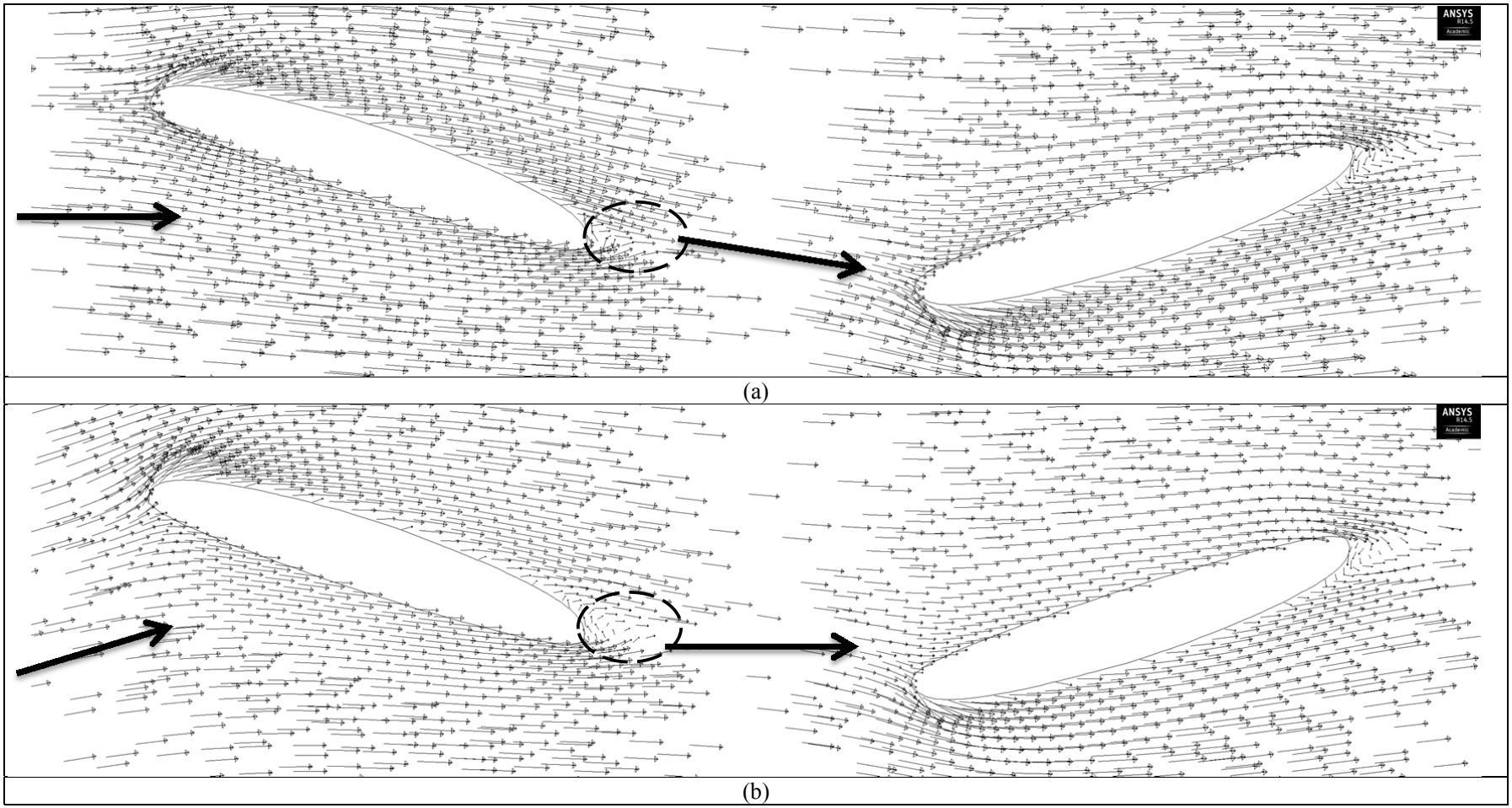

Figure 5-10. Velocity vectors around (a) suspended; and (b) landed PowerWindow bottom blades when $\sigma = 0.428$ and $\theta_0 = 18°$

As can be seen in Figure 5.5 (a), (b), (c) and (d) a significant difference between the suspended PowerWindow and landed PowerWindow is that on the contrary of the suspended PowerWindow, the power captured by the front blades are greater than the power captured by the rear ones in landed PowerWindow. Total power captured by the landed PowerWindow is also higher than suspended PowerWindow, and the operation point of the PowerWindow has shifted to higher λs in the landed position. For example the maximum C_P of the suspended PowerWindow when $\theta_0 = 16°$ is 0.08, in $\lambda = 0.175$, while the maximum C_P of the landed PowerWindow is 0.14, in $\lambda = 0.2$. The reason can be found by investigating the flow mechanism when passing both models. Figure 5.6 (a) and (b) show the velocity ratio (R_V) contours of the wind passing the suspended PowerWindow and the landed PowerWindow with the ramp located at its inlet bottom. R_V shows the local air velocity ratio to the wind velocity in these figures (equation 5.2).

$$R_V = \frac{V_{local}}{V_{wind}} \tag{5-2}$$

As can be seen in Figure 5.6 (a) in the suspended PowerWindow, the maximum R_V is around 1.2 within the blades, while as can be seen in in Figure 5.6 (b) in landed PowerWindow it is almost 1.5. This is because: (i) air flow cannot expand from bottom side of the landed PowerWindow; and (ii) the ramp at the bottom of landed PowerWindow inlet leads more air to its swept area which creates higher velocity there. Increase in the velocity magnitude in the PowerWindow results in increase in its dynamic pressure and as the dynamic pressure of the upstream flow of the PowerWindow increases, higher pressure would be exerted on the pressure side of its blades. On the other hand, vertical velocity of the wind increases when passing above

the ramp. Increase in wind vertical velocity at the upstream of the front blades results in increase in α_1 and decrease in α_2. This is investigated in Figures 5.7-10 (a) and (b) which show the velocity vectors around (a) suspended; and (b) landed PowerWindow bottom blades when (σ=0.428 and) $\theta_0 = 12°, 14°, 16°$ and $18°$. As a result, $P_2 - P_3 > P_4 - P_5$ in this position, while in suspended position, $P_4 - P_5 > P_2 - P_3$. P_2, P_3, P_4 and P_5 refer to the static pressure of air in the sections shown in Figure 5.11. This can more clearly be seen in the pressure contours around the suspended and landed PowerWindow.

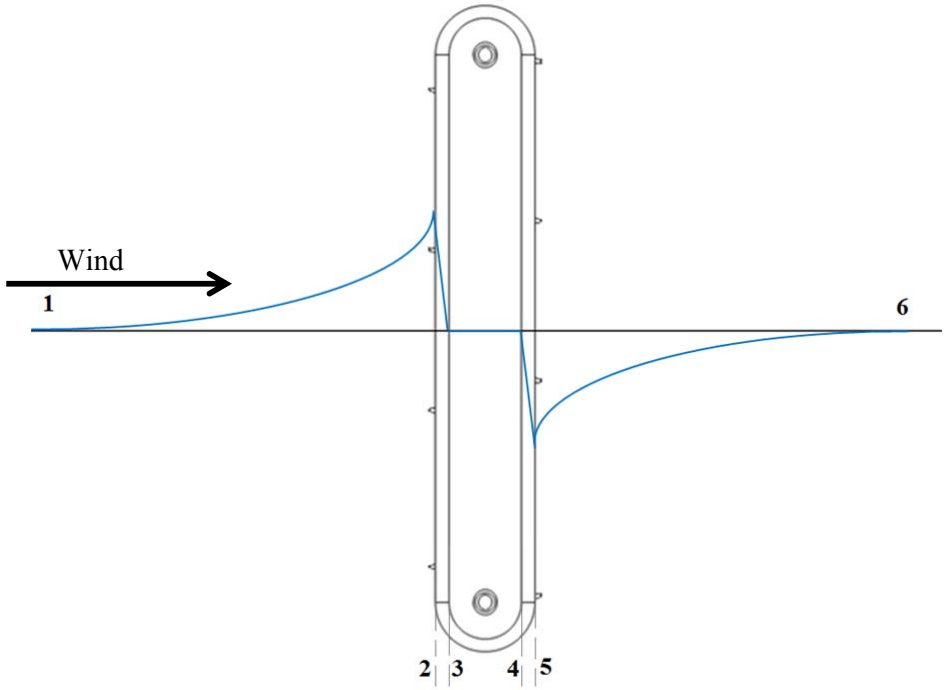

Figure 5-11. Air static pressure when passing PowerWindow.

The regions within the dashed line in Figures 5.7-10 (a) and (b) indicate the separation point on the suction sides of the blades. These figures show that the separation point has slightly shifted to the trailing edge of the blades using the ramp at the bottom of the landed PowerWindow. Therefor using the ramp can change the stall condition and its effect can be investigated in further studies.

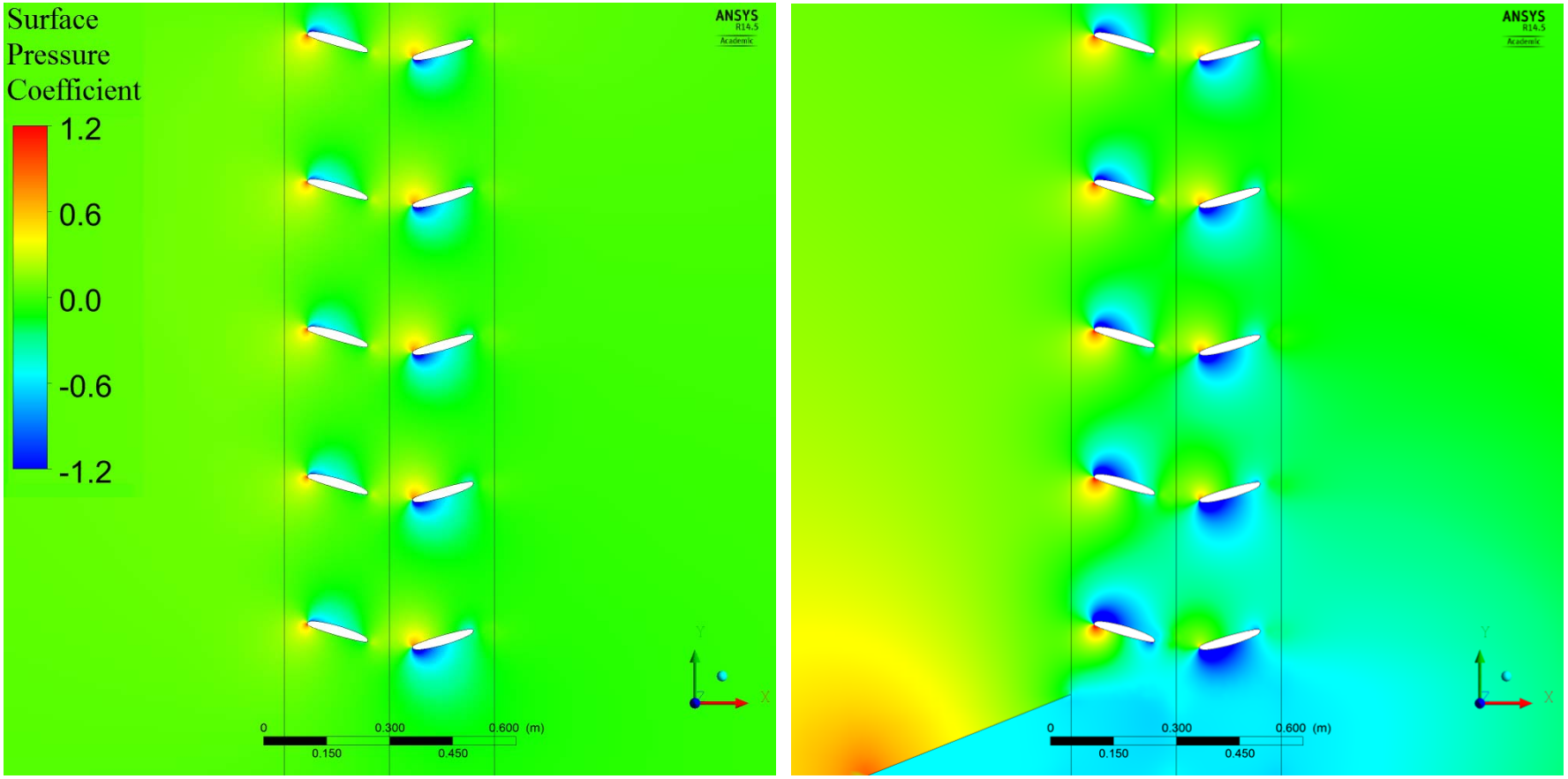

(a) (b)

Figure 5-12. C_{SP} contours of the wind passing (a) the suspended PowerWindow and (b) the landed PowerWindow, with the ramp located at its inlet bottom in $\lambda = 1.0$ ($\sigma = 0.428$ and $\theta_0 = 16°$).

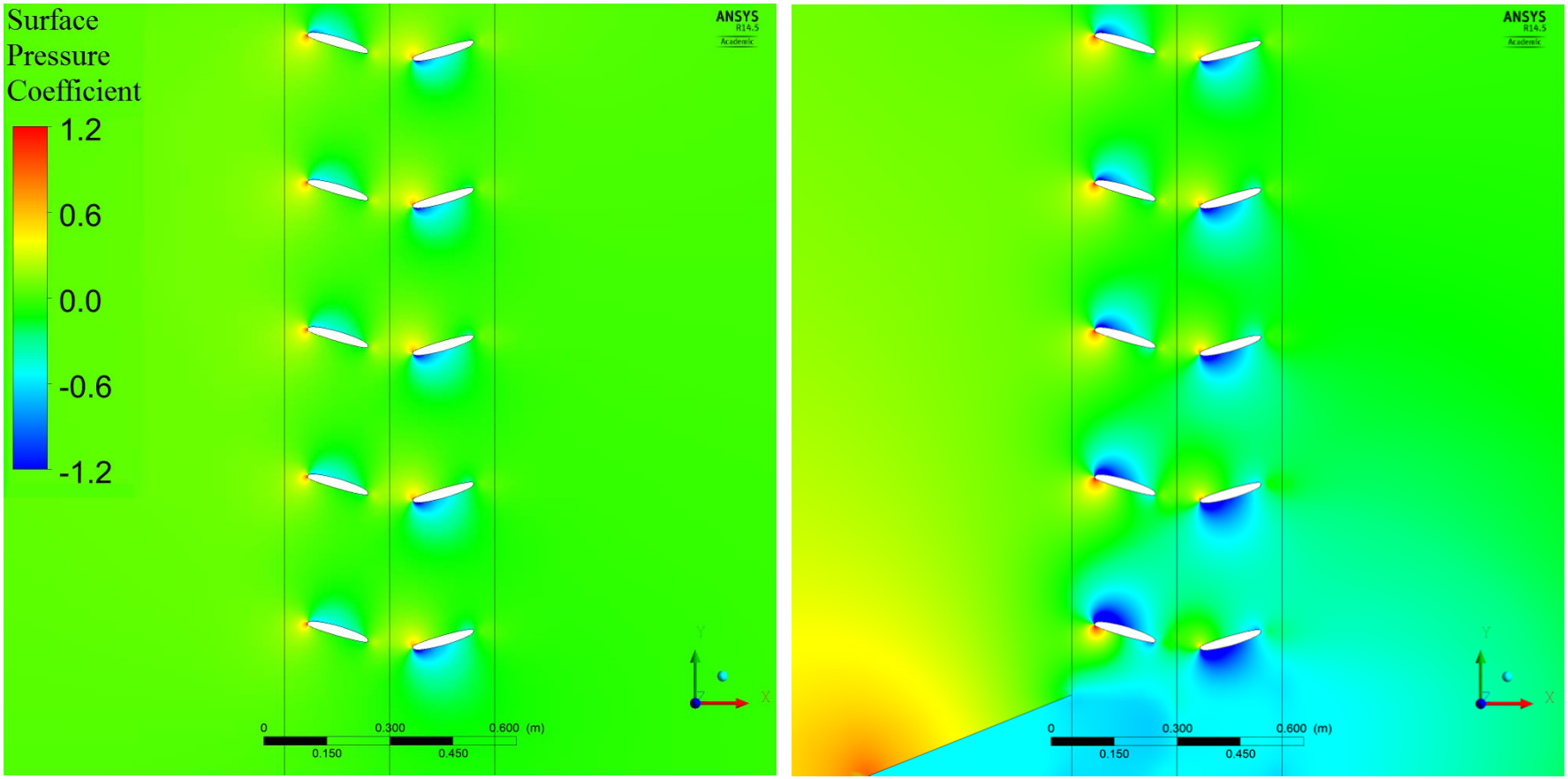

(a) (b)

Figure 5-13. C_{SP} contours of the wind passing (a) the suspended PowerWindow and (b) the landed PowerWindow, with the ramp located at its inlet bottom in $\lambda = 1.5$ ($\sigma = 0.428$ and $\theta_0 = 16°$).

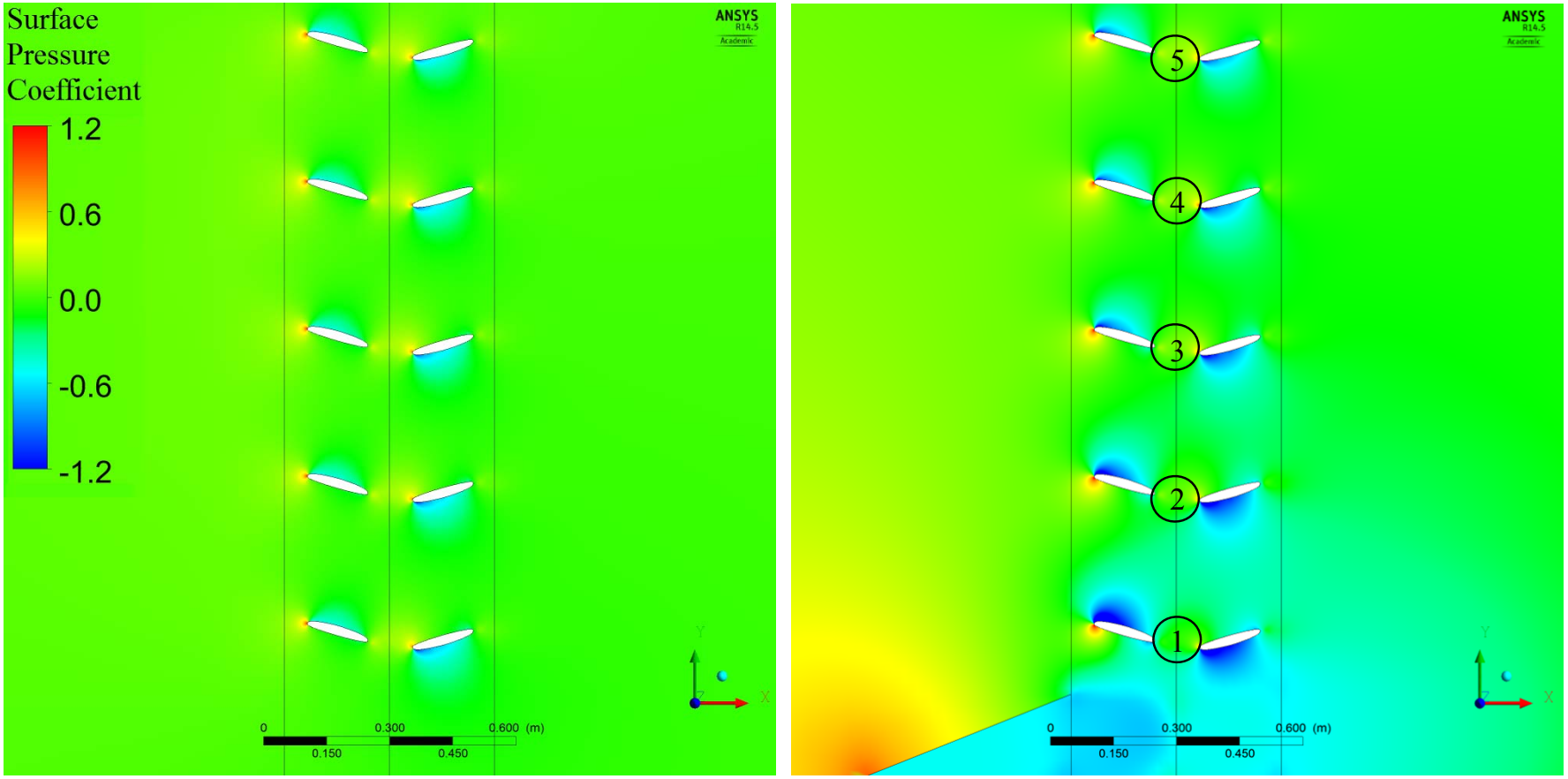

(a) (b)

Figure 5-14. C_{SP} contours of the wind passing (a) the suspended PowerWindow and (b) the landed PowerWindow, with the ramp located at its inlet bottom in $\lambda = 2.0$ ($\sigma = 0.428$ and $\theta_0 = 16°$).

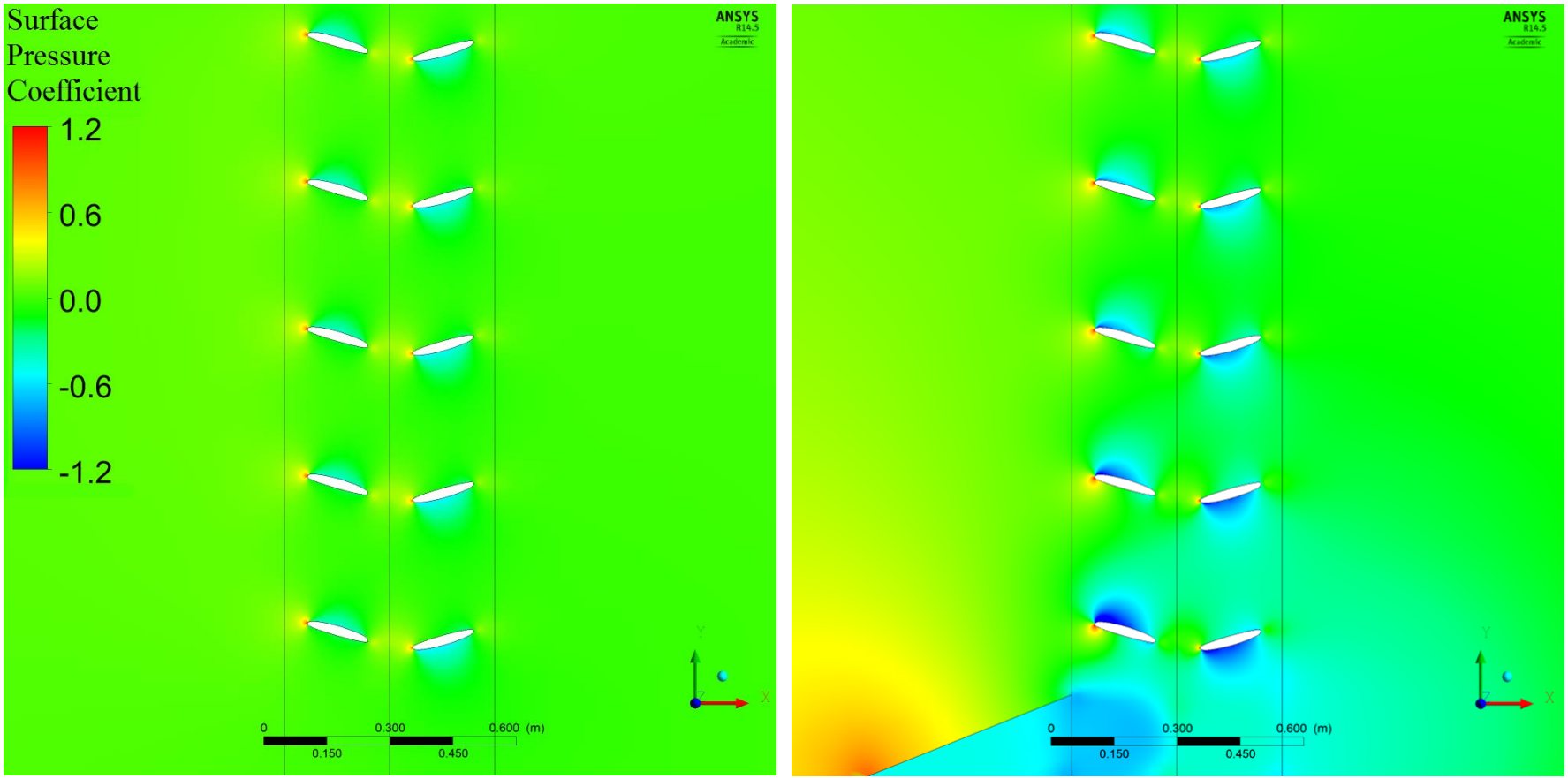

(a) (b)

Figure 5-15. C_{SP} contours of the wind passing (a) the suspended PowerWindow and (b) the landed PowerWindow, with the ramp located at its inlet bottom in $\lambda = 2.5$ ($\sigma = 0.428$ and $\theta_0 = 16°$).

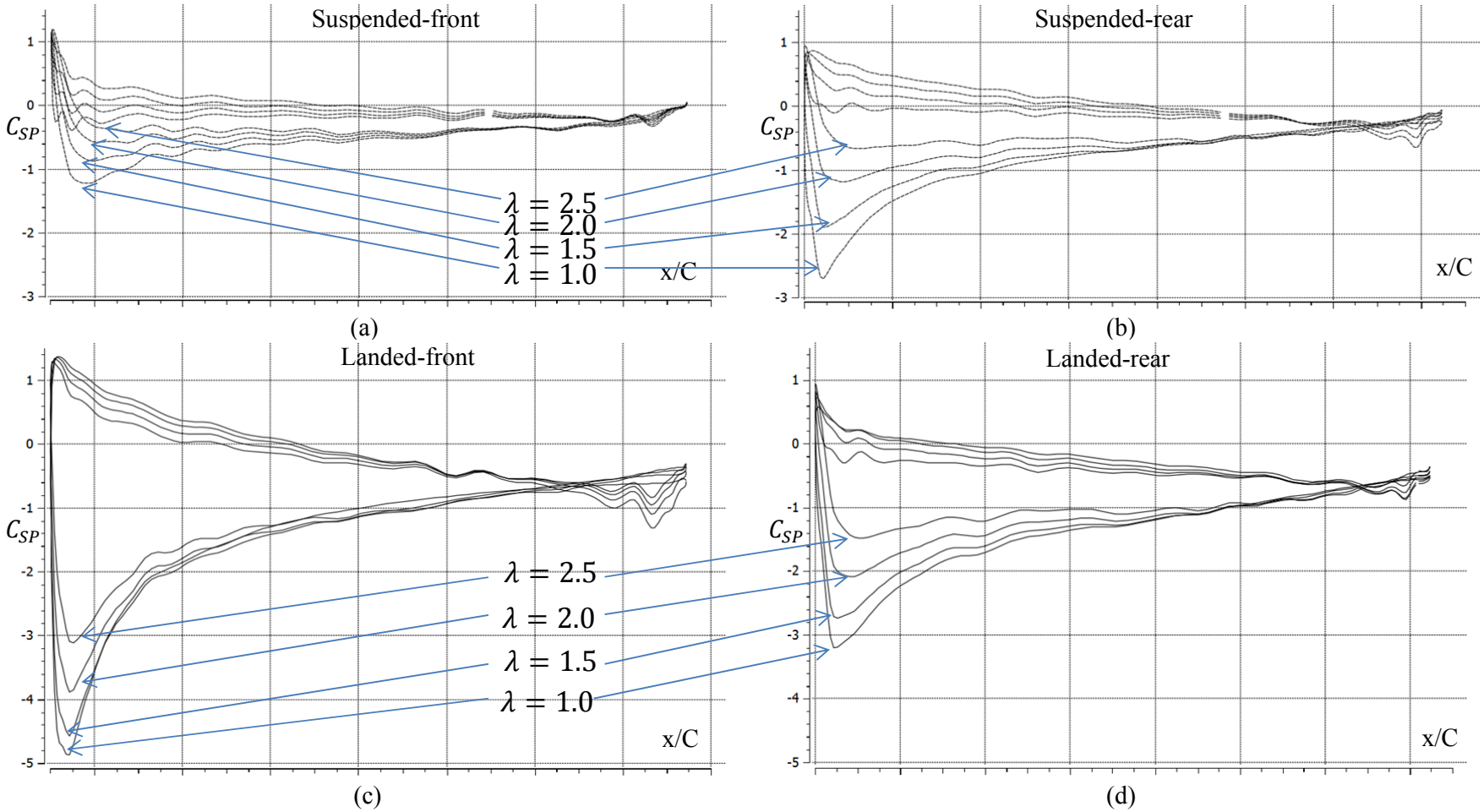

Figure 5-16. C_{SP} over the bottom front and rear blades of the suspended and landed PowerWindow (when $\sigma = 0.428$, $\theta_0 = 16°$) in different λ.

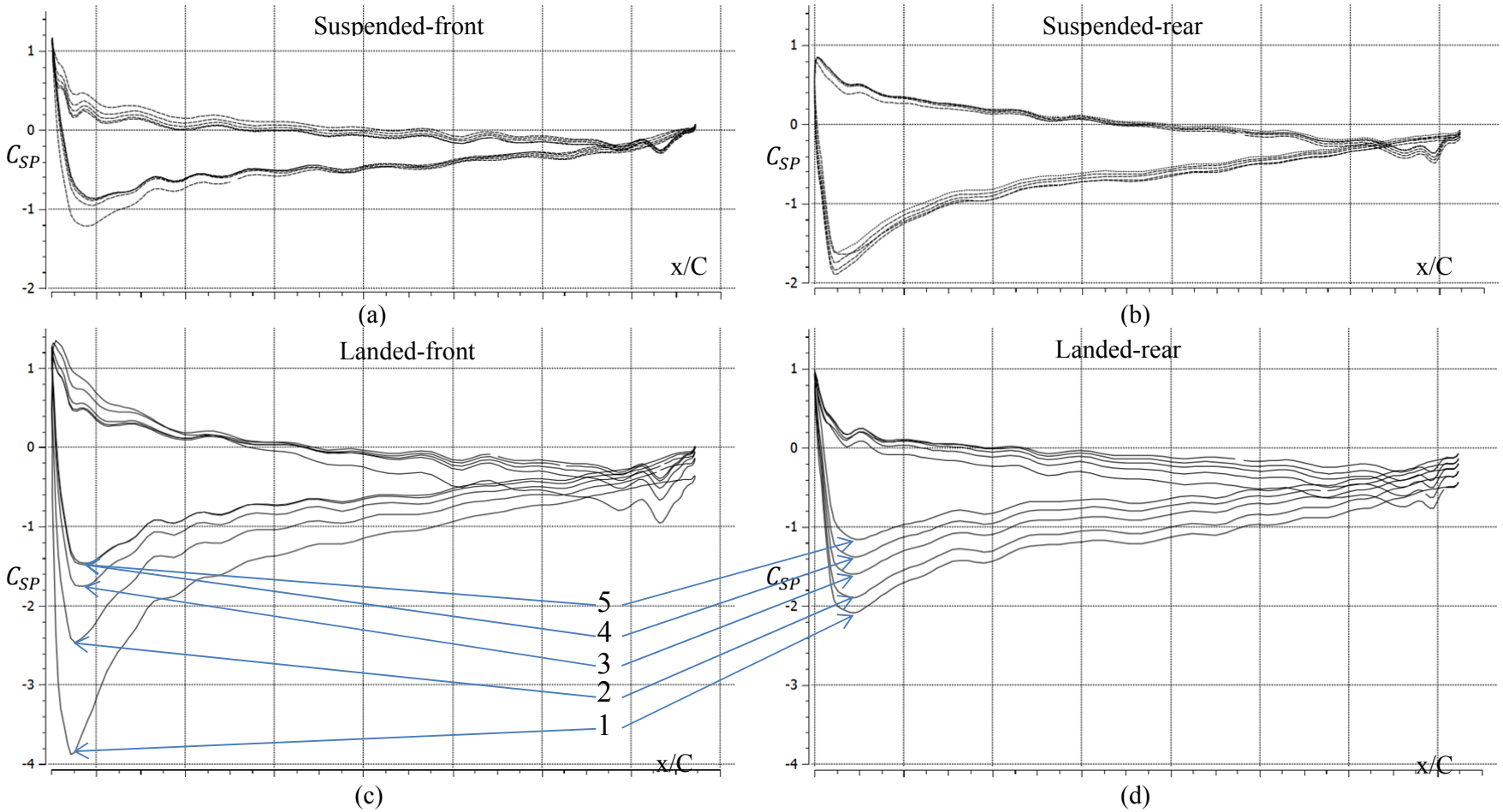

Figure 5-17. C_{SP} over the front and rear blades of the suspended and landed PowerWindow (when $\sigma = 0.428$, $\theta_0 = 16°$) in operating condition.

To have deeper insight over the pressure distribution on the front and rear blades of the suspended and landed PowerWindow, their C_{SP} value is investigated and plotted through their cord line using CFD simulation tools. Figures 5.12 -15 show C_{SP} contours around the front and rear blades of the suspended and landed PowerWindow when $\sigma = 0.428$, $\theta_0 = 16°$ in $\lambda = 0.1$ 0.15, 0.2, and 0.25. Figures 5.16 (a), (b), (c) and (d) also show C_{SP} value over the front and rear blades of the suspended and landed PowerWindow when $\sigma = 0.428$, $\theta_0 = 16°$ in $\lambda = 0.1$, 0.15, 0.2, and 0.25. These figures show that increasing λ has remarkably decreased C_{SP} over the suspended and landed PowerWindow front and rear blades.

Figures 5.17 (a), (b), (c) and (d) show C_{SP} value over the front and rear blades of the suspended and landed PowerWindow (when $\sigma = 0.428$, $\theta_0 = 16°$) in operating condition ($\lambda = 0.15$ for the suspended PowerWindow and $\lambda = 0.2$ for the landed PowerWindow). In Figures 5.17 (a) and (b), C_{SP} curves are very close together. This shows that almost a uniform force is exerted on suspended PowerWindow front and rear blades, which confirm the assumption considered for the BEM model. Moreover C_{SP} curves over the suction side of the rear blades of the suspended PowerWindow are lower than front blades, hence the distance between the C_{SP} curves over the pressure and suction side of the suspended PowerWindow rear blades, plotted in Figure 5.17 (b), are greater than the distance between the C_{SP} lines of its front blades, shown in Figure 5.17 (a). This confirms the BEM model result which has calculated a greater power generation by the rear blades of the suspended PowerWindow compared to its front blades.

On the contrary of the C_{SP} distribution over the suspended PowerWindow blades in Figure 5.17 (a) and (b) in Figures 5.17 (c) and (d), C_{SP} distributions over the blades in landed PowerWindow are very non-uniform, and C_{SP} lines over the suction side of its front blades are achieved lower than the C_{SP} lines of its rear blades. In this figure, pressure lines show the C_{SP} value on the blades, which have been named respectively from the bottom to the top of the landed PowerWindow shown in Figures 5.14 (b). Pressure lines show that as the blades are closer to the ramp (bottom of the landed PowerWindow) the sub-atmospheric pressure on their suction side is lower, so that as can be seen in Figure 5.17 (b), the minimum C_{SP} is almost -2 which belongs to the suspended PowerWindow rear blades, while as can be seen in Figure 5.17 (c) it is almost -4, which belongs to the bottom blade among the landed PowerWindow font blades.

A noticeable point in Figures 5.16 and 5.17 (a), (b), (c) and (d) is that the C_{SP} line crosses the zero pressure line on the pressure side of the blades, so that C_{SP} has a positive value at the leading edge of the blades but a negative value at their trailing edge. The reason is that the flow strangely decelerates when reaching the leading edge and its pressure increases almost to the stagnation pressure. While the flow velocity increases to a value greater than the wind incoming velocity when reaches the trailing edge. As a result the pressure decreases to a value lower than the incoming wind (atmospheric) pressure.

5.3 Effect of Solidity on the Coefficient of Performance

As discussed before, increasing σ may results in increase in the efficiency of PowerWindow. Therefore an investigation has been done to understand effect of σ on the C_P of using the modified BEM model for suspended PowerWindow. Figure 5.18 shows C_P of the suspended PowerWindow against λ when $\theta_0 = 16°$ when $\sigma = 0.428$, 0.857 and 1.714. The assumptions considered for ε is based on value of σ. As mentioned before if $\sigma > 1$ it might be accepted to assume $\varepsilon \approx 1.0$, but as $\sigma \ll 1$, ε would be closer to zero ($\varepsilon \to 0$). Hence ε is approximated $\varepsilon = 0.5$, 0.75 and 1.0 for $\sigma = 0.428$, 0.857 and 1.714 respectively.

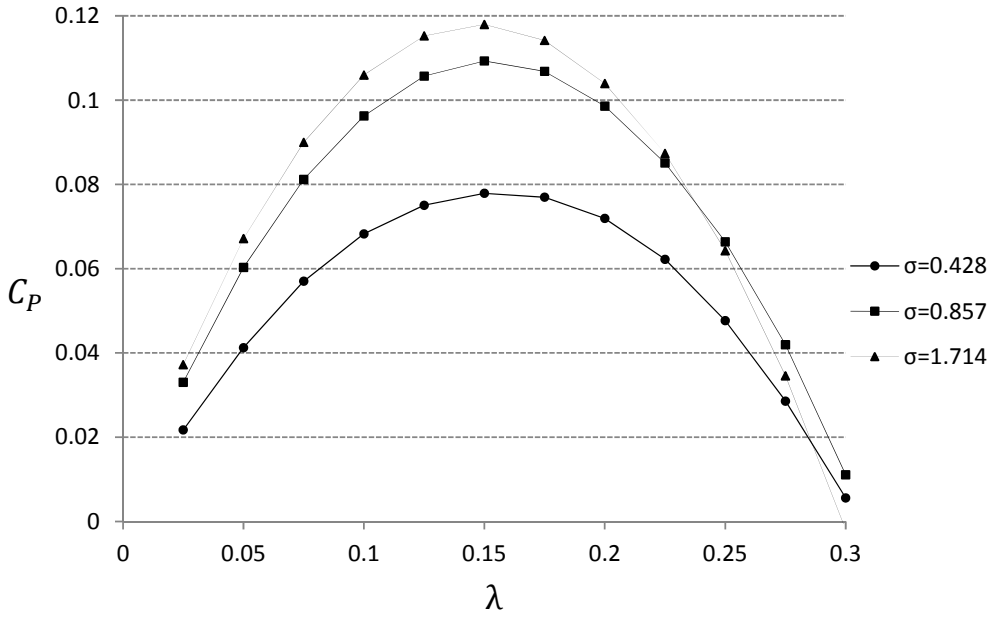

Figure 5-18. C_P of the suspended PowerWindow against λ when $\theta_0 = 16°$ (and $\varepsilon = 0.5$) when $\sigma = 0.428$ (and $\varepsilon = 0.75$), 0.857 and 1.714 (and $\varepsilon = 1.0$).

Figure 5.18 shows that the optimum λ is not dependent on the σ value. This figure also shows that increasing σ from 0.428 to 0.857 has greatly enhanced the C_P, but increasing σ from 0.857 to 1.714 has not remarkably enhanced it. The reason can be

investigated in Figure 3.5 (a). It is shown that as the σ is higher, in a same α, C_L is lower, which results in decrease in vertical force exerted on each blade. However increase in σ also results in increase in projection area which increases the total force exerted on all the blades. Hence there is always an optimum σ for a θ_0 in which the maximum C_P would be gained and further the C_P decreases. More extensive studies are needed to investigate the optimum σ for each θ_0.

Accuracy of the modified BEM model prediction on C_P is also highly dependent on ε, and ε is a function of σ and λ. Hence further investigations are needed to find the relation between ε and σ and λ.

5.4 Effect of Design angle on the Coefficient of Performance

As discussed before, increasing θ_0 may results in increase in the efficiency of PowerWindow. Therefore an investigation has been done to understand effect of θ_0 on the C_P of using the modified BEM model for suspended PowerWindow. Figure 5.19 shows C_P of the suspended PowerWindow against λ when $\theta_0 = 6°$,12°, 18° and 24° when $\sigma = 0.428$ and assuming $\varepsilon = 0.5$. This figure shows that increasing θ_0 has significantly enhanced the C_P and shifted the optimum λ (the operation point) to higher values. As mentioned before equations 3.26 and 3.32 (or 3.38 when $\varepsilon \neq 1$) show that increasing θ_0 generally increases α and as discussed before increasing α results in increasing the lift force exerted on the blades and capturing greater power from wind energy. Hence further studies can be done on optimization of the PowerWindow performance based on θ_0 adjustment.

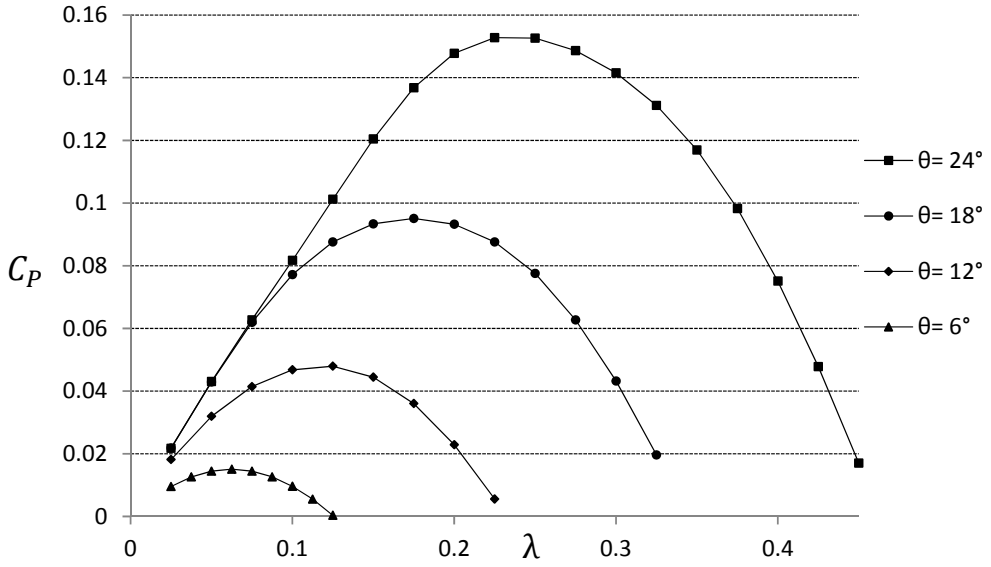

Figure 5-19. C_P of the suspended PowerWindow against λ when $\theta_0 = 6°$, 12°, 18° and 24° when $\sigma = 0.428$ and assuming $\varepsilon = 0.5$

In this study C_P has not been calculated for $\theta_0 > 24°$, since stall is highly possible in further θ_0, while its possibility is dependent on σ for the front and rear blades and also ε for the rear ones. As mentioned before ε is a function of σ and λ. Hence further studies are needed to investigate effect of σ and λ over ε and also σ and ε over C_L and C_D.

5.5 Effect of the Blades Position on the Coefficient of Performance

For investigating how locating the rear blades next to the front ones impacts on the C_P of PowerWindow, the CFD model of the prototype ($\sigma = 0.428$ and $\theta_0 = 16°$) has been built and tested in four different poses shown in Figure 5.20. In each pose L_0 shows the elevation of the front blade to its adjacent rear blade. The L_0/C ratio is $2/3$,$1/3$, 0 and $-1/3$ respectively in pose A, B, C and D while the cord length of each blade is 15cm ($C = 15cm$). This approach allows investigating the relation

between the power generation performance of PowerWindow and position of the front blades to the rear ones. Figure 5.21 shows the C_P achieved by the front, rear and the total blades of the CFD model versus λ. The arrow within the horizontal solid lines shows the C_P achieved by the prototype in the experimental test. The curved lines show the C_P predicted by the CFD model in different λs. The operating condition of the CFD model is the λ in which the maximum C_P is achieved ($\lambda = 0.2$). Figure 5.21 demonstrates that the fluctuation in the maximum C_P of the PowerWindow prototype was also expected by the CFD model.

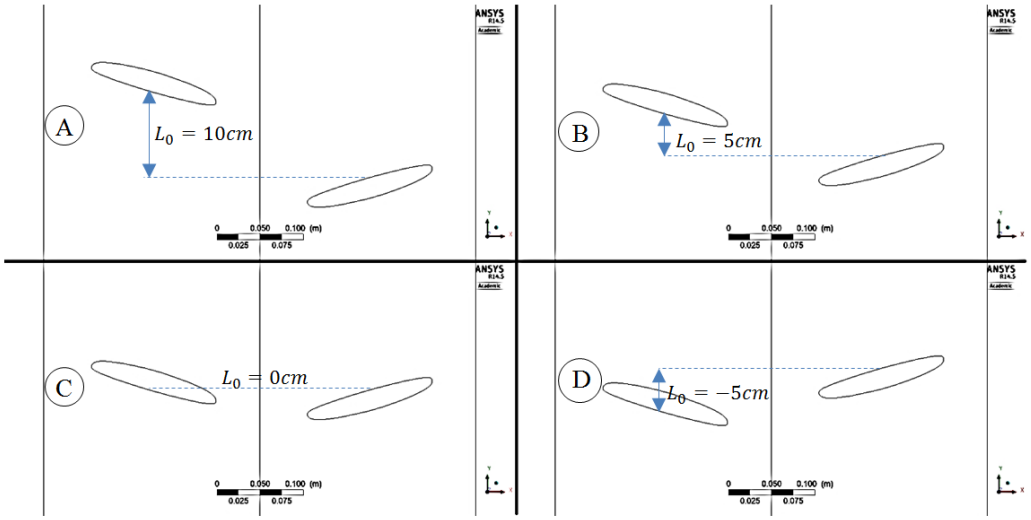

Figure 5-20. Front and rear blades of the PowerWindow CFD model in poses A: ${L_0}/{C} =$, B: ${L_0}/{C} = 1/3$, C: ${L_0}/{C} = 0$ and D: ${L_0}/{C} = -1/3$ (C = 15cm).

Figure 5.21 shows that the C_P of PowerWindow slightly depends on how the rear blades are located next to the front ones which results in a sinusoidal (quasi-steady) C_P. The reason has been investigated via the velocity and pressure distribution analysis. The sinusoidal (quasi-steady) C_P is not desirable, as it can result in noise creation and fatigue failure. However, increasing σ might result in decreasing the fluctuation, which needs more investigations in further studies.

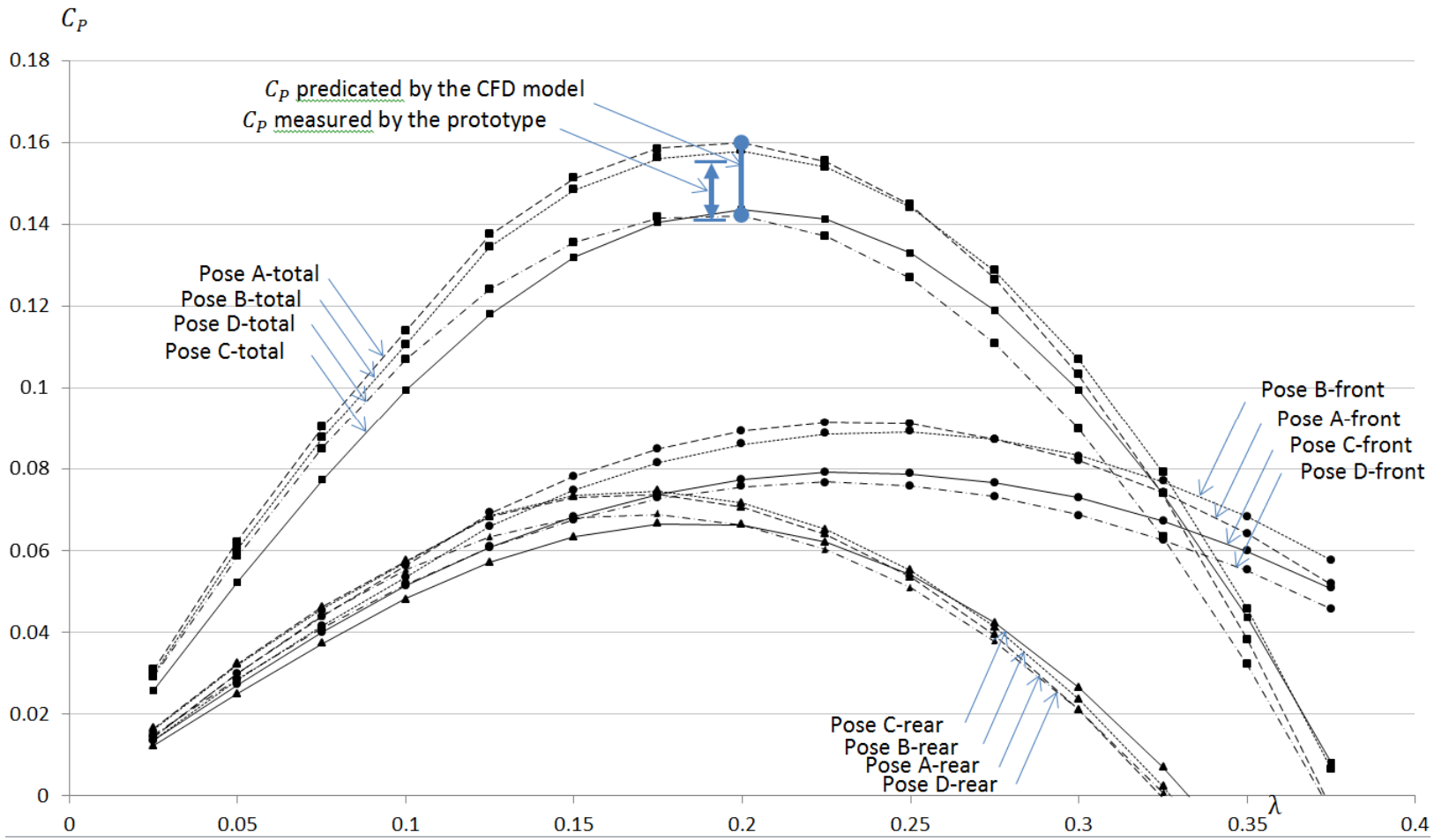

Figure 5-21. C_P of the PowerWindow prototype in operating condition (shown by the arrow between two horizontal solid lines in $\lambda \approx 0.2$), and the CFD model in A, B, C and D poses when $\theta_0 = 16°$ and $\sigma = 0.428$ versus λ.

Figures 5.22 (a), (b), (c) and (d) show the velocity ratio (R_V) the contours of the wind passing the PowerWindow model when $\sigma = 0.428$ and $\theta_0 = 16°$ in operating condition ($\lambda = 0.2$) respectively in poses A, B, C and D. A comparison between Figures 5.22 (a), (b), (c) and (d) show that in pose C and D the rear blades are located in the lower velocity area of the downstream of the front blades which not only adversely affect the wind flow over the rear blades but also blocking the downstream flow of the front blades might decrease the overall pressure drop of the flow passing PowerWindow.

Figure 5.23 (a), (b), (c) and (d) show the streamlines around the PowerWindow blades in $\lambda = 0.2$ (the operating condition) when $\sigma = 0.428$ and $\theta_0 = 16°$ in pose A, B, C and D. This figure shows that in pose A and B the front blades adding a downward velocity to the incoming wind, lead the upstream flow of the rear blades toward them, while in pose D the front blades have almost no effect of the upstream flow of the rear blades. It can also be seen that in pose C the front blades have slightly blocked the upstream flow of the rear blades. Hence the rear blades in pose C, are expected to have a lower C_P.

Figures 5.24 (a), (b), (c) and (d) show the pressure contours of the wind passing over the middle blades of the PowerWindow model when $\sigma = 0.428$ and $\theta_0 = 16°$ in operating condition ($\lambda = 0.2$) respectively in poses A, B, C and D. Figure 5.25 (a) and (b) show the C_{SP} value over these blades. Figure 5.24 and 5.25 agree that the power generated by PowerWindow in pose A and B is higher than C and D due to the higher pressure created on their pressure side and lower pressure created on their suction side.

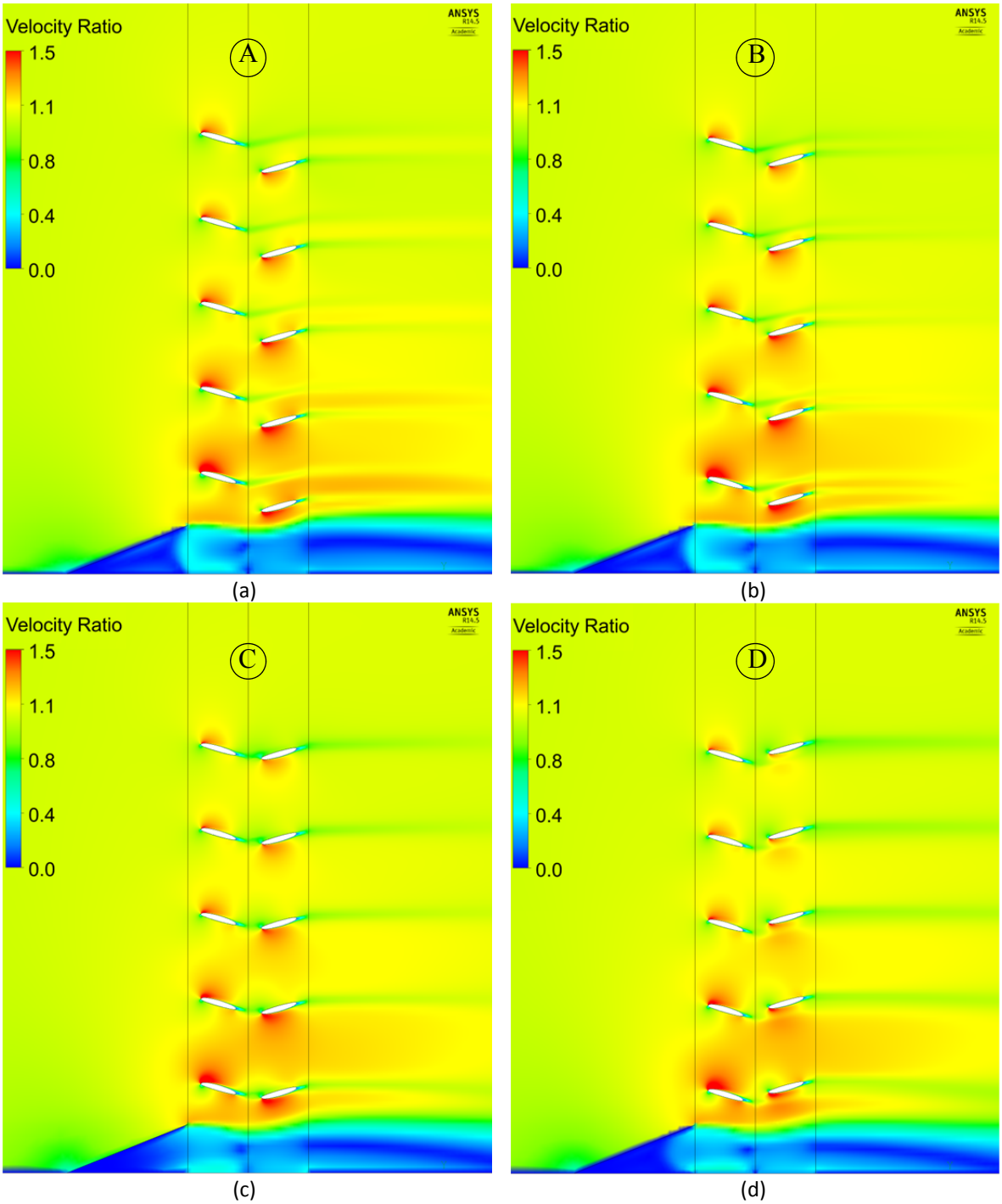

Figure 5-22 R_V contours of the wind passing the PowerWindow CFD model in $\lambda = 0.2$ (the operating condition) when $\sigma = 0.428$ and $\theta_0 = 16$ ° in (a) pose A, (b) pose B, (c) pose C and (d) pose D.

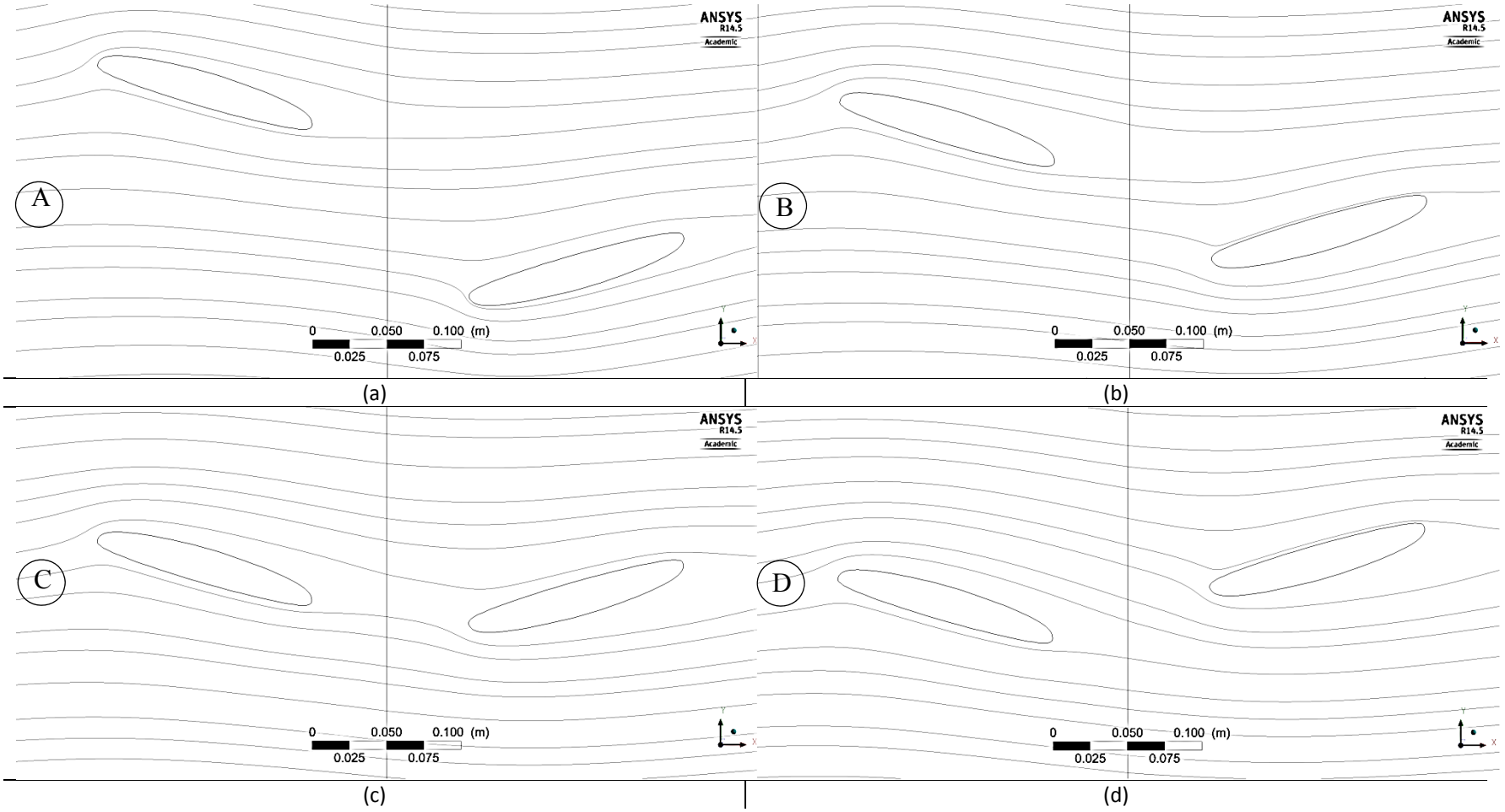

Figure 5-23 Streamlines around the the middle blades of PowerWindow model in $\lambda = 0.2$ (the operating condition) when $\sigma = 0.428$ and $\theta_0 = 16$ ° in (a) pose A, (b) pose B, (c) pose C and (d) pose D.

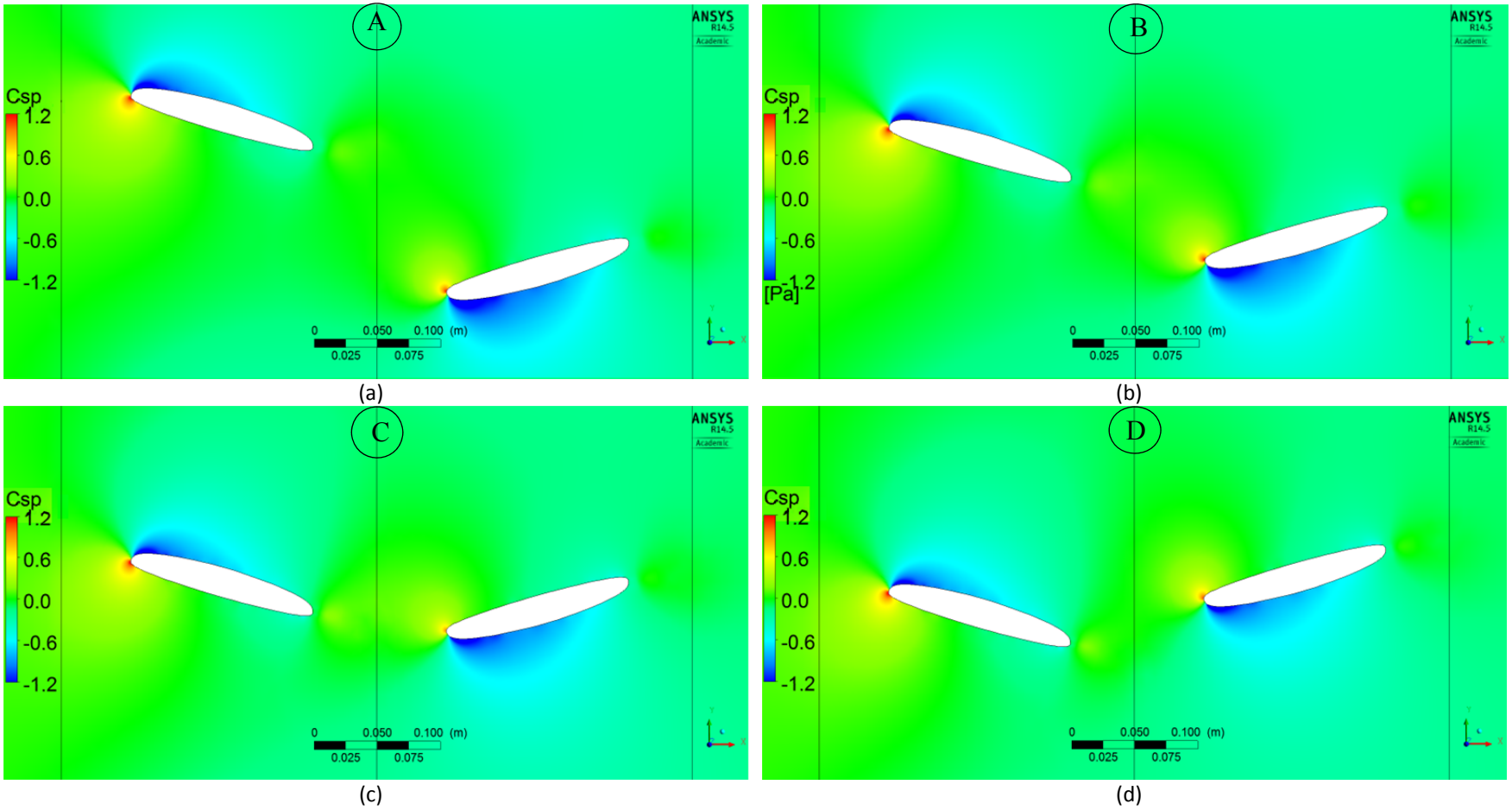

Figure 5-24 Air static pressure over the middle blades of PowerWindow CFD model in $\lambda = 0.2$ (the operating condition) when $\sigma = 0.428$ and $\theta_0 = 16$ ° in (a) pose A, (b) pose B, (c) pose C and (d) pose D.

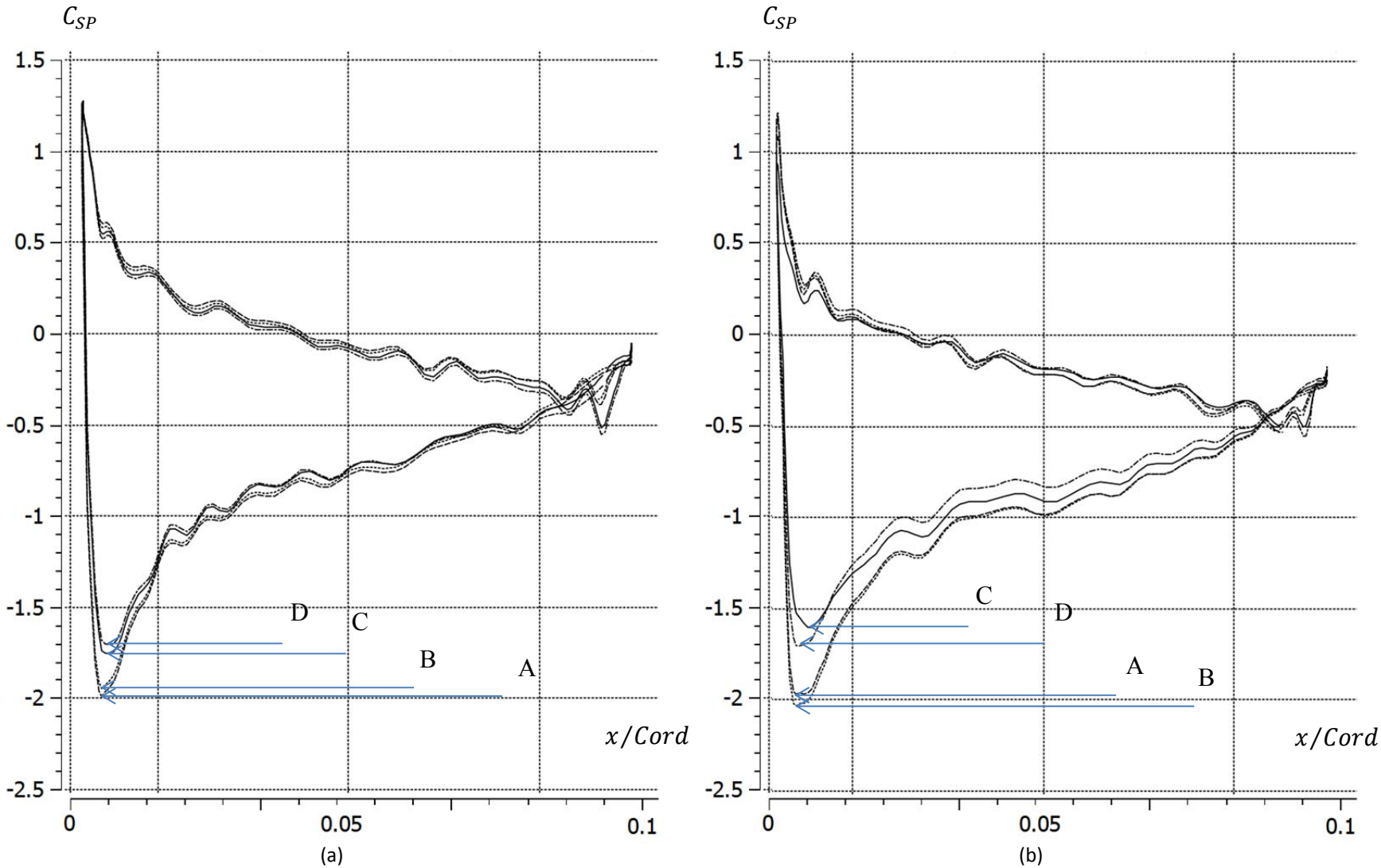

Figure 5-25 C_{SP} distribution over the (a) front and (b) rear middle blades of PowerWindow CFD model, when $\sigma = 0.428$, $\theta_0 = 16°$ and $\lambda = 0.2$ though the cord length.

CHAPTER 6. CONCLUSION AND PROSPECTS

An analytical model based on the modified BEM theory successfully predicted the performance of a suspended PowerWindow. CFD model of the suspended PowerWindow has also been created and its results have been validated by the BEM model. CFD model of a landed PowerWindow was also created and an analogy has been done between this type and the suspended one. Validity of the CFD model of the landed PowerWindow was confirmed by an experimental test from the prototype operating in same condition.

Investigations on the aerodynamic mechanism of the PowerWindow showed that this device can generate electricity with an acceptable efficiency (around 15%) in very low linear velocity ratios (around 0.2) which is not achievable with most of the common wind turbines. Studies showed that front blades of PowerWindow can increase the angle of attack of the rear blades and consequently raise their performance significantly. It was also shown that using a ramp at the bottom of the PowerWindow inlet can greatly increase the power captured by the PowerWindow by increasing its inlet velocity magnitude and its direction. By using the ramp for the prototype the coefficient of performance of the PowerWindow with solidity of 0.428 was enhanced from 5%, 6.5%, 8% and10% to 9.5%, 12%, 14.5% and 17% (which means $70-100\%$ increase) respectively.

The BEM and CFD model developed in this study assist to analyze PowerWindow mechanism and performance, and can be very useful for optimization of the device and enhancing its performance. Effect of solidity and design angle on

performance of the suspended PowerWindow was also investigated in this study and it was shown that:

(i) Performance of the PowerWindow can be enhanced by increasing the design angle.

(ii) Increasing the design angle further than an optimum point, increases possibility of stall on PowerWindow blades which eventually results in decrease in its performance.

(iii) Increasing the solidity of PowerWindow, decrease possibility of stall and increases the angle in which stall happens.

(iv) Increasing solidity of the PowerWindow till an optimum point enhances its performance.

(v) Performance of the rear blades of PowerWindow is highly dependent of affected flow ratio, which is dependent on the solidity of the PowerWindow and its operating linear velocity ratio.

(vi) Coefficient of performance of PowerWindow slightly depends on how the rear blades are located next to the front ones, which results in a sinusoidal power generation, and is not desirable, as it results in noise creation and fatigue failure.

(vii) Increasing the solidity might assists to minimize the fluctuation of PowerWindow.

REFERENCES

1. Eriksson, S., H. Bernhoff, and M. Leijon, *Evaluation of different turbine concepts for wind power.* Renewable and Sustainable Energy Reviews, 2008. **12**(5): p. 1419-1434.

2. Bak, C. and P. Fuglsang, *Modification of the NACA 632-415 leading edge for better aerodynamic performance.* Journal of Solar Energy Engineering, 2002. **124**(4): p. 327-334.

3. Malcolm, D.J., *Modal Response of 3-Bladed Wind Turbines.* Journal of Solar Energy Engineering, 2002. **124**(4): p. 372-377.

4. Miller, R.H., *The aerodynamics and dynamic analysis of horizontal axis and wind turbines.* Journal of Wind Engineering and Industrial Aerodynamics, 1983. **15**(1–3): p. 329-340.

5. Schreck, S.J., et al., *Blade Dynamic Stall Vortex Kinematics for a Horizontal Axis Wind Turbine in Yawed Conditions*.* Journal of Solar Energy Engineering, 2001. **123**(4): p. 272-281.

6. Islam, M., D.S.K. Ting, and A. Fartaj, *Aerodynamic models for Darrieus-type straight-bladed vertical axis wind turbines.* Renewable and Sustainable Energy Reviews, 2008. **12**(4): p. 1087-1109.

7. Drew, D.R., J.F. Barlow, and T.T. Cockerill, *Estimating the potential yield of small wind turbines in urban areas: A case study for Greater London, UK.* Journal of Wind Engineering and Industrial Aerodynamics, 2013. **115**(0): p. 104-111.

8. Sharma, R.N. and U.K. Madawala, *The concept of a smart wind turbine system.* Renewable Energy, 2012. **39**(1): p. 403-410.

9. Kosasih, B. and S. Jafari, *High-Efficiency Shrouded Micro Wind Turbine for Urban-Built Environment.* Applied Mechanics and Materials, 2014. **493**: p. 294-299.

10. Billinton, R. and G. Bai, *Generating capacity adequacy associated with wind energy.* Energy Conversion, IEEE Transactions on, 2004. **19**(3): p. 641-646.

11. Lee, S., et al., *Effects of design parameters on aerodynamic performance of a counter-rotating wind turbine.* Renewable Energy, 2012. **42**(0): p. 140-144.

12. Lee, S., H. Kim, and S. Lee, *Analysis of aerodynamic characteristics on a counter-rotating wind turbine.* Current Applied Physics, 2010. **10**(2 SUPPL.): p. S339-S342.

13. Hwang, B., S. Lee, and S. Lee, *Optimization of a counter-rotating wind turbine using the blade element and momentum theory.* Journal of Renewable and Sustainable Energy, 2013. **5**(5).

14. Mohamed, M.H., *Performance investigation of H-rotor Darrieus turbine with new airfoil shapes.* Energy, 2012. **47**(1): p. 522-530.

15. Aslam Bhutta, M.M., et al., *Vertical axis wind turbine – A review of various configurations and design techniques.* Renewable and Sustainable Energy Reviews, 2012. **16**(4): p. 1926-1939.

16. Mohamed, M.H., et al., *Optimal blade shape of a modified Savonius turbine using an obstacle shielding the returning blade.* Energy Conversion and Management, 2011. **52**(1): p. 236-242.

17. Akwa, J.V., H.A. Vielmo, and A.P. Petry, *A review on the performance of Savonius wind turbines.* Renewable and Sustainable Energy Reviews, 2012. **16**(5): p. 3054-3064.

18. Gupta, R. and A. Biswas, *Computational fluid dynamics analysis of a twisted three-bladed H-Darrieus rotor.* Journal of Renewable & Sustainable Energy, 2010. **2**(4): p. 043111.

19. Sharpe, T. and G. Proven, *Crossflex: Concept and early development of a true building integrated wind turbine.* Energy and Buildings, 2010. **42**: p. 2365-2375.

20. Debnath, B.K., A. Biswas, and R. Gupta, *Computational fluid dynamics analysis of a combined three-bucket Savonius and three-bladed Darrieus rotor at various overlap conditions.* Journal of Renewable & Sustainable Energy, 2009. **1**(3): p. 033110.

21. Zhang, Q., H. Chen, and B. Wang, *Modeling and Simulation of Two-Leaf Semi-rotary VAWT*, in *Life System Modeling and Intelligent Computing*, K. Li, et al., Editors. 2010, Springer Berlin Heidelberg. p. 389-398.

22. Pope, K., et al., *Effects of stator vanes on power coefficients of a zephyr vertical axis wind turbine.* Renewable Energy, 2010. **35**(5): p. 1043-1051.

23. Bedon, G., M. Raciti Castelli, and E. Benini, *Optimization of a Darrieus vertical-axis wind turbine using blade element – momentum theory and evolutionary algorithm.* Renewable Energy, 2013. **59**(0): p. 184-192.

24. Meyer, K., *WOMBAT—A tool for mixed model analyses in quantitative genetics by restricted maximum likelihood (REML).* Journal of Zhejiang University SCIENCE B, 2007. **8**(11): p. 815-821.

25. Mertens and S. Mertens, *The energy yield of roof mounted wind turbines.* Wind Engineering, 2003. **27**(6): p. 507-518.

26. Ponta, F.L., J.J. Seminara, and A.D. Otero, *On the aerodynamics of variable-geometry oval-trajectory Darrieus wind turbines.* Renewable Energy, 2007. **32**(1): p. 35-56.

27. Ponta, F.L. and L.I. Lago, *Analysing the suspension system of variable-geometry oval-trajectory (VGOT) Darrieus wind turbines.* Energy for Sustainable Development, 2008. **12**(2): p. 5-16.

28. Otero, A.D. and F.L. Ponta, *On the structural behaviour of variable-geometry oval-trajectory Darrieus wind turbines.* Renewable Energy, 2009. **34**(3): p. 827-832.

29. Joselin Herbert, G.M., et al., *A review of wind energy technologies.* Renewable and Sustainable Energy Reviews, 2007. **11**(6): p. 1117-1145.

30. Ramsamooj, D.V. and T.A. Shugar, *Modeling of corrosion fatigue in metals in an aggressive environment.* International Journal of Fatigue, 2001. **23, Supplement 1**(0): p. 301-309.

31. Zhiquan, Y., et al., *Structure Dynamic Analysis of a Horizontal Axis Wind Turbine System Using a Modal Analysis Method.* Wind Engineering, 2001. **25**(4): p. 237-248.

32. Wei, D. and Z. Feng. *Loading Analysis and Strength Calculation of Wind Turbine Blade Based on Blade Element Momentum Theory and Finite Element Method*. in *Power and Energy Engineering Conference (APPEEC), 2010 Asia-Pacific*. 2010.

33. Lanzafame, R. and M. Messina, *Fluid dynamics wind turbine design: Critical analysis, optimization and application of BEM theory.* Renewable Energy, 2007. **32**(14): p. 2291-2305.

34. Glauert, H., *Airplane propellers, Aerodynamic theory, Julius Springer (Berlin.* Germany), 1935: p. 169-360.

35. Rajagopalan, R.G. and S.R. Mathur, *Three dimensional analysis of a rotor in forward flight.* Journal of the American Helicopter Society, 1993. **38**(3): p. 14-25.

36. Pratumnopharat, P. and P.S. Leung, *Validation of various windmill brake state models used by blade element momentum calculation.* Renewable Energy, 2011. **36**(11): p. 3222-3227.

37. Sørensen, J.N. and C.W. Kock, *A model for unsteady rotor aerodynamics.* Journal of Wind Engineering and Industrial Aerodynamics, 1995. **58**(3): p. 259-275.

38. Bohorquez, F., D. Pines, and P.D. Samuel, *Small Rotor Design Optimization Using Blade Element Momentum Theory and Hover Tests.* Journal of Aircraft, 2010. **47**(1): p. 268-283.

39. Hu, Y. and S.S. Rao, *Robust Design of Horizontal Axis Wind Turbines Using Taguchi Method.* Journal of Mechanical Design, 2011. **133**(11): p. 111009-111009.

40. Ohyama, K. and T. Nakashima. *Wind turbine emulator using wind turbine model based on blade element momentum theory*. in *Power Electronics Electrical Drives Automation and Motion (SPEEDAM), 2010 International Symposium on*. 2010.

41. Masters, I., et al., *A robust blade element momentum theory model for tidal stream turbines including tip and hub loss corrections.* Proceedings of IMarEST - Part A - Journal of Marine Engineering and Technology, 2011. **10**(1): p. 25-35.

42. Malki, R., et al., *Planning tidal stream turbine array layouts using a coupled blade element momentum – computational fluid dynamics model.* Renewable Energy, 2014. **63**(0): p. 46-54.

43. Buckland, H.C., et al., *Cavitation inception and simulation in blade element momentum theory for modelling tidal stream turbines.* Proceedings of the Institution of Mechanical Engineers, Part A: Journal of Power and Energy, 2013. **227**(4): p. 479-485.

44. Døssing, M., H.A. Madsen, and C. Bak, *Aerodynamic optimization of wind turbine rotors using a blade element momentum method with corrections for wake rotation and expansion.* Wind Energy, 2012. **15**(4): p. 563-574.

45. Bai, C.J.H., F.B. *Using CFD Computation for Aerodynamic Performance Design and Analysis of Horizontal Axis Wind Turbine Blade*. in *15th National Computational Fluid Dynamics Conference*. 2008. Tainan, Taiwan.

46. Robin, L., G. Janusz, and M. Florian, *Predicting 2D Airfoil and 3D Wind Turbine Rotor Performance using a Transition Model for General CFD Codes*, in *44th AIAA Aerospace Sciences Meeting and Exhibit*. 2006, American Institute of Aeronautics and Astronautics.

47. Xu, G. and L.N. Sankar, *Development of engineering aerodynamics models using a viscous flow methodology on the NREL phase VI rotor.* Wind Energy, 2002. **5**(2-3): p. 171-183.

48. Shen, W.Z., et al., *Tip loss corrections for wind turbine computations.* Wind Energy, 2005. **8**(4): p. 457-475.

49. Madsen, H.A., et al., *Validation and modification of the Blade Element Momentum theory based on comparisons with actuator disc simulations.* Wind Energy, 2010. **13**(4): p. 373-389.

50. Carroll, J. and D. Marcum, *Comparison of a Blade Element Momentum Model to 3D CFD Simulations for Small Scale Propellers.* SAE International Journal of Aerospace, 2013. **6**(2): p. 721-726.

51. Malki, R., et al., *A coupled blade element momentum – Computational fluid dynamics model for evaluating tidal stream turbine performance.* Applied Mathematical Modelling, 2013. **37**(5): p. 3006-3020.

52. Esfahanian, V., et al., *Numerical analysis of flow field around NREL Phase II wind turbine by a hybrid CFD/BEM method.* Journal of Wind Engineering and Industrial Aerodynamics, 2013. **120**(0): p. 29-36.

53. Lanzafame, R., S. Mauro, and M. Messina, *Wind turbine CFD modeling using a correlation-based transitional model.* Renewable Energy, 2013. **52**(0): p. 31-39.

54. O'Doherty, T., et al. *Considerations of a horizontal axis tidal turbine*. Proceedings of the ICE - Energy, 2010. **163**, 119-130.

55. Vermeer, L.J., J.N. Sørensen, and A. Crespo, *Wind turbine wake aerodynamics.* Progress in Aerospace Sciences, 2003. **39**(6–7): p. 467-510.

56. Whale, J., et al., *An experimental and numerical study of the vortex structure in the wake of a wind turbine.* Journal of Wind Engineering and Industrial Aerodynamics, 2000. **84**(1): p. 1-21.

57. Sezer-Uzol, N. and L.N. Long, *3-D Time-Accurate CFD Simulations of Wind Turbine Rotor Flow Fields*.

58. Buning, P.G., et al., *Application of the chimera overlapped grid scheme to simulation of space shuttle ascent flows*, in *The 4th international symposium on computational fluid dynamics*. 1991: Davis, California. p. 132–137.

59. Li, Y., et al., *Dynamic overset CFD simulations of wind turbine aerodynamics.* Renewable Energy, 2012. **37**(1): p. 285-298.

60. Sørensen, N.N., J.A. Michelsen, and S. Schreck, *Navier-Stokes predictions of the NREL phase VI rotor in the NASA Ames 80 ft × 120 ft wind tunnel.* Wind Energy, 2002. **5**(2-3): p. 151-169.

61. Mark, P. and M. Dimitri, *Unstructured Mesh CFD Aerodynamic Analysis of the NREL Phase VI Rotor*, in *47th AIAA Aerospace Sciences Meeting including The New Horizons Forum and Aerospace Exposition*. 2009, American Institute of Aeronautics and Astronautics.

62. Bazilevs, Y., et al., *3D simulation of wind turbine rotors at full scale. Part I: Geometry modeling and aerodynamics.* International Journal for Numerical Methods in Fluids, 2011. **65**(1-3): p. 207-235.

63. Jonkman, J., et al., *Definition of a 5-MW Reference Wind Turbine for Offshore System Development*. 2009. p. Medium: ED; Size: 75 pp.

64. Fu, P. and M. Farzaneh, *A CFD approach for modeling the rime-ice accretion process on a horizontal-axis wind turbine.* Journal of Wind Engineering and Industrial Aerodynamics, 2010. **98**(4–5): p. 181-188.

65. AbdelSalam, A.M. and V. Ramalingam, *Wake prediction of horizontal-axis wind turbine using full-rotor modeling.* Journal of Wind Engineering and Industrial Aerodynamics, 2014. **124**(0): p. 7-19.

66. Jafari, S.A.H. and B. Kosasih, *Flow analysis of shrouded small wind turbine with a simple frustum diffuser with computational fluid dynamics simulations.* Journal of Wind Engineering and Industrial Aerodynamics, 2014. **125**(0): p. 102-110.

67. Guo, T., et al., *A CFD/CSD model for aeroelastic calculations of large-scale wind turbines.* Science China Technological Sciences, 2013. **56**(1): p. 205-211.

68. David, C., et al., *Investigating Aeroelastic Performance of Multi-Mega Watt Wind Turbine Rotors Using CFD*, in *53rd AIAA/ASME/ASCE/AHS/ASC Structures, Structural Dynamics and Materials Conference*. 2012, American Institute of Aeronautics and Astronautics.

69. Sanderse, B., S.P. van der Pijl, and B. Koren, *Review of computational fluid dynamics for wind turbine wake aerodynamics.* Wind Energy, 2011. **14**(7): p. 799-819.

70. Raciti Castelli, M., A. Englaro, and E. Benini, *The Darrieus wind turbine: Proposal for a new performance prediction model based on CFD.* Energy, 2011. **36**(8): p. 4919-4934.

71. Hirahara, H., et al., *Testing basic performance of a very small wind turbine designed for multi-purposes.* Renewable Energy, 2005. **30**(8): p. 1279-1297.

72. Kishinami, K., et al., *Theoretical and experimental study on the aerodynamic characteristics of a horizontal axis wind turbine.* Energy, 2005. **30**(11–12): p. 2089-2100.

73. Hailiang, X., H. Jiabing, and H. Yikang, *Operation of Wind-Turbine-Driven DFIG Systems Under Distorted Grid Voltage Conditions: Analysis and Experimental Validations.* Power Electronics, IEEE Transactions on, 2012. **27**(5): p. 2354-2366.

74. Utsunomiya, T., et al., *At Sea Experiment of a Hybrid Spar for Floating Offshore Wind Turbine Using 1/10-Scale Model.* Journal of Offshore Mechanics and Arctic Engineering, 2013. **135**(3): p. 034503-034503.

75. Wei, K., et al. *Modeling analysis and experimental research on a combined-type vertical axis wind turbine*. in *Electronics, Communications and Control (ICECC), 2011 International Conference on*. 2011.

76. Ingram, G., *Wind Turbine Blade Analysis using the Blade Element Momentum Method*. 2005.

77. Shives, M. and C. Crawford, *Developing an empirical model for ducted tidal turbine performance using numerical simulation results.* Proceedings of the Institution of Mechanical Engineers, Part A: Journal of Power and Energy, 2011.

78. Menter, F.R., *Review of the shear-stress transport turbulence model experience from an industrial perspective.* Int. J. Comput. Fluid Dyn., 2009. **23**(4): p. 305-316.

79. El-Behery, S.M. and M.H. Hamed, *A comparative study of turbulence models performance for separating flow in a planar asymmetric diffuser.* Computers & Fluids, 2011. **44**(1): p. 248-257.

80. Buice, C.U. and J.K. Eaton, *Experimental Investigation of Flow Through an Asymmetric Plane Diffuser.* Journal of Fluids Engineering, 2000. **122**(2): p. 433-435.

A. APPENDIX A

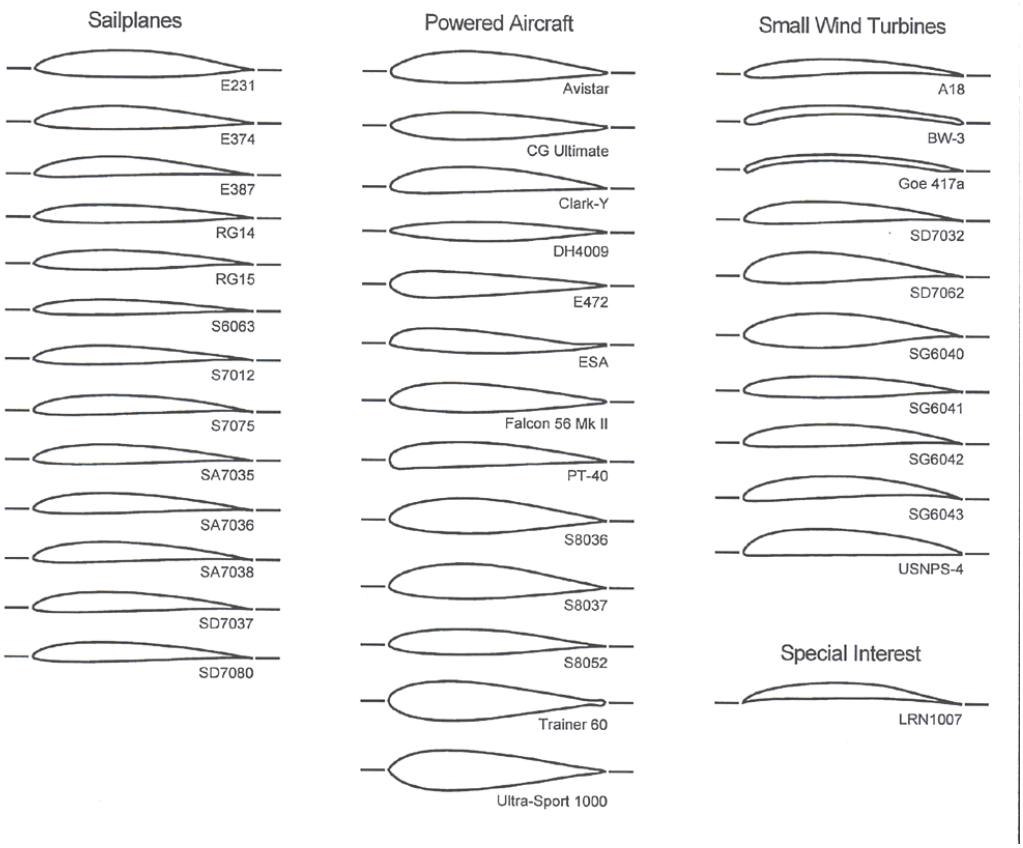

Figure A-1. A number of commercial airfoils with different applications

B. APPENDIX B

C_L and C_D data file of the isolated airfoil and cascade configuration of the the PowerWindow blade.

Table B.1. C_L against α when $\sigma = 0.428, 0.857$ and 1.714.

α	C_L, $(isolated)$	C_L,$(\sigma = 0.428)$	C_L,$(\sigma = 0.857)$	C_L,$(\sigma = 1.714)$
-14	-0.5146	-0.53831	-0.08904	-0.09314
-13	-0.55047	-0.52076	-0.09524	-0.0901
-12	-0.58218	-0.4914	-0.10073	-0.08502
-11	-0.59409	-0.4558	-0.10279	-0.07886
-10	-0.57404	-0.41529	-0.09932	-0.07185
-9	-0.53285	-0.37086	-0.09219	-0.06417
-8	-0.47945	-0.32393	-0.08295	-0.05605
-7	-0.41613	-0.27551	-0.072	-0.04767
-6	-0.34682	-0.2255	-0.06001	-0.03902
-5	-0.27344	-0.17415	-0.04731	-0.03013
-4	-0.19734	-0.12212	-0.03414	-0.02113
-3	-0.11803	-0.07	-0.02042	-0.01211
-2	-0.03875	-0.01679	-0.0067	-0.0029
-1	0.043803	0.036933	0.007579	0.00639
0	0.126327	0.090887	0.021857	0.015725
1	0.20858	0.144663	0.036089	0.02503
2	0.289663	0.198723	0.050117	0.034383
3	0.369019	0.252289	0.063848	0.043651
4	0.447455	0.305506	0.077419	0.052859
5	0.525151	0.357891	0.090862	0.061922
6	0.602442	0.409735	0.104234	0.070892
7	0.67711	0.460728	0.117154	0.079715
8	0.750857	0.511307	0.129913	0.088466
9	0.821759	0.561048	0.142181	0.097073
10	0.889908	0.609819	0.153972	0.105511
11	0.953287	0.657579	0.164938	0.113774
12	1.011519	0.703763	0.175013	0.121765
13	1.061839	0.748847	0.183719	0.129566
14	1.105192	0.792137	0.19122	0.137055
15	1.136123	0.833719	0.196572	0.14425
16	1.144139	0.872065	0.197959	0.150885
17	1.127982	0.907414	0.195163	0.157001
18	1.09882	0.938098	0.190118	0.16231
19	1.046339	0.963956	0.181037	0.166784
20	1.011973	0.985124	0.175091	0.170446
21	0.982084	0.995754	0.16992	0.172285
22	0.95918	0.991368	0.165957	0.171526

23	0.946941	0.965359	0.16384	0.167026
24	0.942245	0.918569	0.163027	0.158931
25	0.94	0.871399	0.162639	0.150769
26	0.93	0.841119	0.160909	0.14553
27	0.920082	0.818976	0.159193	0.141699
28	0.935946	0.801256	0.161937	0.138633
29	0.980702	0.78824	0.169681	0.136381
30	0.985508	0.778597	0.170513	0.134713
31	0.997587	0.771853	0.172603	0.133546
32	1.005455	0.766602	0.173964	0.132637
33	1.018852	0.762861	0.176282	0.13199
34	1.02	0.75946	0.17648	0.131402
35	1.034281	0.756196	0.178951	0.130837
36	1.046177	0.752677	0.18101	0.130228

Table B.2. C_D against α when $\sigma = 0.428, 0.857$ and 1.714.

α	C_D, $(isolated)$	C_D,$(\sigma = 0.428)$	C_D,$(\sigma = 0.857)$	C_D,$(\sigma = 1.714)$
-14	0.191419	0.149895	0.125186	0.122531
-13	0.167881	0.13779	0.116733	0.118558
-12	0.147844	0.126456	0.108937	0.114874
-11	0.132808	0.116045	0.101671	0.111466
-10	0.119735	0.106496	0.09508	0.10835
-9	0.108285	0.097773	0.089179	0.105493
-8	0.098257	0.090034	0.083994	0.102964
-7	0.089561	0.083327	0.079495	0.100745
-6	0.082203	0.077635	0.075639	0.098855
-5	0.076214	0.072928	0.072531	0.097301
-4	0.071447	0.069207	0.070138	0.096074
-3	0.067929	0.066466	0.068387	0.095185
-2	0.065471	0.064667	0.067325	0.094638
-1	0.064069	0.063863	0.066968	0.094424
0	0.063768	0.064036	0.067287	0.094523
1	0.06443	0.065148	0.068296	0.094968
2	0.066099	0.067246	0.069962	0.095755
3	0.068863	0.07025	0.072318	0.096894
4	0.072586	0.074175	0.075326	0.098328
5	0.07733	0.078952	0.079	0.098328
6	0.082977	0.084613	0.083269	0.102136
7	0.089534	0.091021	0.088211	0.104492
8	0.096934	0.098334	0.093715	0.107164
9	0.105182	0.106392	0.099796	0.110123
10	0.114342	0.115172	0.106383	0.113404
11	0.124164	0.124686	0.113542	0.116934
12	0.134765	0.134806	0.121197	0.120714

13	0.146369	0.145625	0.129286	0.124746
14	0.158993	0.157042	0.137845	0.129019
15	0.172905	0.168961	0.146843	0.133458
16	0.187549	0.181195	0.156173	0.138159
17	0.204601	0.193801	0.165876	0.14301
18	0.225887	0.206544	0.175895	0.148055
19	0.251576	0.219344	0.186212	0.153143
20	0.282951	0.232529	0.196806	0.158454
21	0.312467	0.245407	0.207537	0.163889
22	0.341388	0.258126	0.218467	0.169426
23	0.370957	0.272084	0.229532	0.175061
24	0.399836	0.290049	0.240641	0.180776
25	0.42	0.312598	0.25154	0.186563
26	0.46	0.335885	0.262579	0.192376
27	0.509655	0.358774	0.273752	0.198192
28	0.545086	0.381597	0.284636	0.203983
29	0.548298	0.40401	0.2946	0.209785
30	0.576176	0.425938	0.304838	0.215586
31	0.608047	0.447253	0.320724	0.221234
32	0.640249	0.468222	0.342402	0.226778
33	0.67388	0.488565	0.363876	0.23226
34	0.7	0.5087	0.384649	0.237653
35	0.738836	0.528572	0.404692	0.243099
36	0.776315	0.548265	0.424129	0.248317

C. APPENDIX C

Modified BEM model programed for a PowerWindow prototype configuration (which has been investigated in this study), when 5 blades are located on each side ($N = 5$), each blade and PowerWindow swept area equals $0.3\,m^2$ and $3.35\,m^2$ ($B = 0.3\ m.s^{-1}, A = 3.35\ m.s^{-1}$), which results a solidity of 0.428 ($\sigma = 0.428$), design angle of $18°$ ($\theta_0 = 12°$), when incoming wind velocity is $8\,m.s^{-1}$($V = 8\,m.s^{-1}$) and AFR is 0.5 ($\varepsilon = 0.5$).

```
syms i
N=5;
A=3.35;
B=0.30;
S=(N*B)/A;
e=0.5;
T=12*(pi/180);
V=8;
counter=0;
deg=11;
format long
Coef_Cl=polyfit(a,Cl,deg)
deg=5;
format long
Coef_Cd=polyfit(a,Cd,deg)
for y=0.025:0.025:0.225
    counter=counter+1;
    y
    b1=atan(y/(1-i));
    a1=(T-b1)*(180/pi);
    Cl1= poly2sym(Coef_Cl,a1);
    Cd1= poly2sym(Coef_Cd,a1);
    b2=atan(((1+e)*y-(1-i)*e*tan(T))/(1-i));
    a2=(T-b2)*(180/pi);
    Cl2= poly2sym(Coef_Cl,a2);
    Cd2= poly2sym(Coef_Cd,a2);
    P1= V*y*.5*1.2*V^2*N*B* (1-2*i+i^2+y^2 )*(Cl1*cos(b1) -
Cd1*sin(b1));
    P2= V*y*.5*1.2*V^2*N*B*(1-2*i+i^2+((1+e)*y-e*(1-
i)*tan(T))^2)*(Cl2*cos(b2) - Cd2*sin(b2));
    Pt=P1+P2;
    Pw=0.5*1.2*V^3*A* 4*i*(1-i)^2 ;
    x=solve (Pw -  Pt == 0, i)
%    digits(1000);
    x=double(x);
    b1=atan(y/(1-x));
    a1=(T-b1)*(180/pi)
    Cl1= polyval(Coef_Cl,a1);
    Cd1= polyval(Coef_Cd,a1);
    b2=atan(((1+e)*y-(1-x)*e*tan(T))/(1-x));
    a2=(T-b2)*(180/pi)
    Cl2= polyval(Coef_Cl,a2);
    Cd2= polyval(Coef_Cd,a2);
```

```
    P1= V*y*.5*1.2*V^2*N*B* (1-2*x+x^2+y^2 )*(Cl1*cos(b1) -
Cd1*sin(b1))
    P2= V*y*.5*1.2*V^2*N*B*(1-2*x+x^2+((1+e)*y-e*(1-
x)*tan(T))^2)*(Cl2*cos(b2) - Cd2*sin(b2))
    Pt=P1+P2
    Pw=0.5*1.2*V^3*A* 4*x*(1-x)^2;
    fP1(counter)=P1;
    fP2(counter)=P2;
    fPt(counter)=Pt;
end
```

Note 1: $\sigma, \varepsilon, \theta_0, \alpha, \beta, a, \lambda, P_{front,} P_{rear}$ and P_{total} are replaced with $S, e, T, a, b, i(\text{or } x), y, P_1 P_2$ and P_t in the program.

Note 2: C_L and C_D data file for the relevant cascade configuration (reported in appendix B), should be opened before running the program.

D. APPENDIX D

Power extraction by the PowerWindow front and rear blades and the relevant a, α_1 and $\alpha_2$in every λ calculated by the modified BEM model when $\sigma = 0.428$, $\varepsilon = 0.5$ and 1, $\theta_0 = 12°$, 14°, 16° and 18°

Table D.1. Modified BEM results when $\sigma = 0.428$, $\varepsilon = 0.5$ and $\theta_0 = 12°$

λ	a	P_{total}(W)	α_1	P_{front}(W)	α_2	P_{rear}(W)
0.025	0.004249	17.34363	10.5618	7.1779	15.92538	10.16573
0.05	0.007526	30.51746	9.115924	12.69639	13.75897	17.82107
0.075	0.009803	39.56599	7.668545	16.60495	11.57972	22.96103
0.1	0.0111	44.6827	6.225741	18.86261	9.400251	25.82009
0.125	0.011376	45.7687	4.793856	19.37607	7.233748	26.39262
0.15	0.010531	42.4407	3.379801	18.07195	5.094183	24.36876
0.175	0.008505	34.41779	1.990322	14.95304	2.995026	19.46475
0.2	0.005369	21.86376	0.630605	10.10683	0.946968	11.75693
0.225	0.001295	5.316928	-0.69629	3.666413	-1.04303	1.650515

Table D.2. Modified BEM results when $\sigma = 0.428$, $\varepsilon = 1$ and $\theta_0 = 12°$

λ	a	P_{total}(W)	α_1	P_{front}(W)	α_2	P_{rear}(W)
0.025	0.004659	18.99877	10.5612	7.171676	21.21998	11.82709
0.05	0.008652	35.00071	9.112656	12.6641	18.3726	22.33661
0.075	0.011409	45.90091	7.661533	16.53962	15.48075	29.3613
0.1	0.01281	51.38889	6.215805	18.77482	12.57073	32.61407
0.125	0.013002	52.1413	4.782104	19.27721	9.66724	32.86409
0.15	0.011981	48.14528	3.367336	17.97218	6.795782	30.17311
0.175	0.009568	38.63765	1.979794	14.87349	3.984051	23.76416
0.2	0.005758	23.43213	0.626266	10.07631	1.255298	13.35582
0.225	0.000832	3.418882	-0.6906	3.703032	-1.37747	-0.28415

Table D.3. Modified BEM results when $\sigma = 0.428$, $\varepsilon = 0.5$ and $\theta_0 = 14°$

λ	a	P_{total}(W)	α_1	P_{front}(W)	α_2	P_{rear}(W)
0.025	0.004795	19.54885	12.56101	8.228448	18.97127	11.3204
0.05	0.008795	35.5687	11.11224	14.74437	16.80517	20.82433
0.075	0.011788	47.38661	9.659879	19.66411	14.62003	27.7225
0.1	0.013757	54.90317	8.210291	23.28381	12.42887	31.61936
0.125	0.014756	58.96218	6.769396	24.84525	10.24426	34.11693
0.15	0.014774	59.03337	5.343234	24.95657	8.079022	34.0768
0.175	0.013711	54.90317	3.938566	23.28381	5.946951	31.61936
0.2	0.011475	46.15692	2.562226	19.80634	3.86162	26.35058
0.225	0.008096	32.78836	1.219508	14.59423	1.83378	18.19412
0.25	0.003737	15.26879	-0.0868	7.776296	-0.13018	7.492497

Table D.4. Modified BEM results when $\sigma = 0.428$, $\varepsilon = 1$ and $\theta_0 = 14°$

λ	a	P_{total}(W)	α_1	P_{front}(W)	α_2	P_{rear}(W)
0.025	0.004715	19.22716	12.56112	8.22983	25.25985	10.99733
0.05	0.009335	37.71302	11.11067	14.7266	22.44029	22.98642
0.075	0.013326	53.4025	9.65314	19.59228	19.55751	33.81022
0.1	0.01597	63.65621	8.197358	22.91455	16.63845	40.74166
0.125	0.017084	67.94211	6.752453	24.68133	13.71254	43.26078
0.15	0.01692	67.31464	5.324623	24.78313	10.80418	42.53151
0.175	0.01561	62.2696	3.919548	23.11272	7.936647	39.15689
0.2	0.012988	52.08552	2.545149	19.65871	5.136926	32.42682
0.225	0.008938	36.13776	1.209005	14.50792	2.429704	21.62984
0.25	0.003672	15.00453	-0.08592	7.783102	-0.17177	7.221431

Table D.5. Modified BEM results when $\sigma = 0.428$, $\varepsilon = 0.5$ and $\theta_0 = 16°$

λ	a	P_{total}(W)	α_1	P_{front}(W)	α_2	P_{rear}(W)
0.025	0.005091	20.74567	14.56058	9.273013	22.03267	11.47266
0.05	0.009755	39.37758	13.10944	16.80392	19.86924	22.57366
0.075	0.013591	54.4357	11.65198	22.66691	17.67958	31.76879
0.1	0.016357	65.14991	10.19509	26.99946	15.47738	38.15045
0.125	0.018047	71.63105	8.745421	29.87603	13.27631	41.75502
0.15	0.018757	74.34509	7.308628	31.25639	11.08873	43.0887
0.175	0.018527	73.46514	5.890213	31.02012	8.926757	42.44502
0.2	0.01727	68.65723	4.496567	29.04748	6.803646	39.60975
0.225	0.014869	59.4028	3.134545	25.29051	4.732965	34.11228
0.25	0.011307	45.4993	1.80968	19.79668	2.725722	25.70263
0.275	0.006716	27.27423	0.524758	12.68319	0.788145	14.59104
0.3	0.001302	5.344469	-0.7198	4.085447	-1.07768	1.259022

Table D.6. Modified BEM results when $\sigma = 0.428$, $\varepsilon = 1$ and $\theta_0 = 16°$

λ	a	P_{total}(W)	α_1	P_{front}(W)	α_2	P_{rear}(W)
0.025	0.004783	19.50202	14.56102	9.278999	29.30625	10.22302
0.05	0.009298	37.56677	13.11078	16.82089	26.52591	20.74588
0.075	0.013906	55.66207	11.65059	22.65022	23.66763	33.01184
0.1	0.018056	71.66552	10.18512	26.88564	20.74854	44.77988
0.125	0.02079	82.06019	8.725313	29.65727	17.80064	52.40293
0.15	0.021754	85.69747	7.282409	30.98184	14.85847	54.71564
0.175	0.021274	83.88792	5.862421	30.73733	11.94666	53.15059
0.2	0.019672	77.82482	4.469135	28.77487	9.084865	49.04995
0.225	0.016871	67.12486	3.109228	25.04517	6.297571	42.07969
0.25	0.012668	50.83334	1.790919	19.62079	3.610634	31.21255
0.275	0.007152	29.02037	0.518285	12.62522	1.039181	16.39516
0.3	0.000675	2.7762	-0.7099	4.168981	-1.41456	-1.39278

Table D.7. Modified BEM results when $\sigma = 0.428$, $\varepsilon = 0.5$ and $\theta_0 = 18°$

λ	a	P_{total}(W)	α_1	P_{front}(W)	α_2	P_{rear}(W)
0.025	0.00512	20.86021	16.56054	10.22055	25.11186	10.63966
0.05	0.010162	40.98507	15.10826	18.82631	22.95458	22.15876
0.075	0.014801	59.13791	13.64665	25.69356	20.76351	33.44435
0.1	0.01858	73.67029	12.18203	30.91933	18.55117	42.75096
0.125	0.021206	83.63149	10.72225	34.67639	16.33302	48.95509
0.15	0.022666	89.12224	9.274403	37.06773	14.12366	52.05451
0.175	0.023108	90.77897	7.843784	38.06283	11.9351	52.71615
0.2	0.022635	89.00766	6.435114	37.53071	9.778344	51.47695
0.225	0.021202	83.61474	5.054108	35.32649	7.665621	48.28825
0.25	0.018677	74.03782	3.707464	31.37169	5.61022	42.66613
0.275	0.014993	59.88186	2.401019	25.68669	3.623515	34.19517
0.3	0.010234	41.27116	1.137838	18.37112	1.711997	22.90004
0.325	0.004599	18.75985	-0.08195	9.55708	-0.1229	9.20277

Table D.8. Modified BEM results when $\sigma = 0.428$, $\varepsilon = 1$ and $\theta_0 = 18°$

λ	a	P_{total}(W)	α_1	P_{front}(W)	α_2	P_{rear}(W)
0.025	0.005128	20.89536	16.56052	10.22037	33.35824	10.67499
0.05	0.009641	38.92356	15.10978	18.8477	30.6229	20.07586
0.075	0.013808	55.28336	13.65102	25.75229	27.80498	29.53107
0.1	0.018302	72.60568	12.18367	30.94034	24.91004	41.66533
0.125	0.022699	89.24491	10.71126	34.54266	21.95361	54.70225
0.15	0.02575	100.6119	9.247206	36.75157	18.97339	63.86037
0.175	0.026771	104.3793	7.806365	37.64243	16.01219	66.73691
0.2	0.026065	101.7773	6.395487	37.09536	13.09686	64.68189
0.225	0.024174	94.76012	5.016005	34.91394	10.24245	59.84618
0.25	0.0212	83.60806	3.672137	30.9942	7.468385	52.61386
0.275	0.016914	67.29221	2.372021	25.38247	4.80025	41.90974
0.3	0.011259	45.31135	1.121348	18.203	2.256172	27.10835
0.325	0.004521	18.4432	-0.08062	9.570101	-0.16117	8.873104

E. APPENDIX E

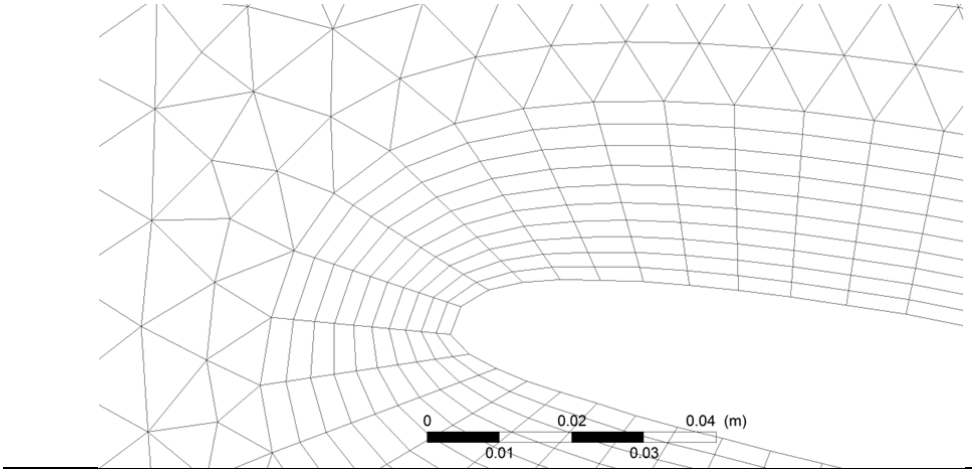

(a)

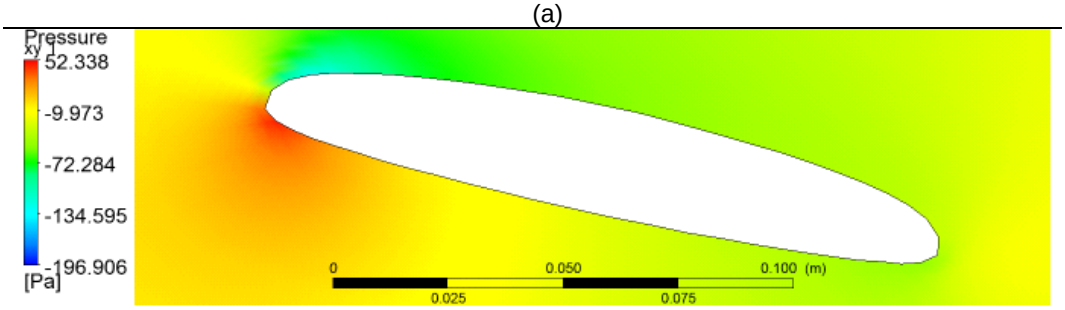

(b)

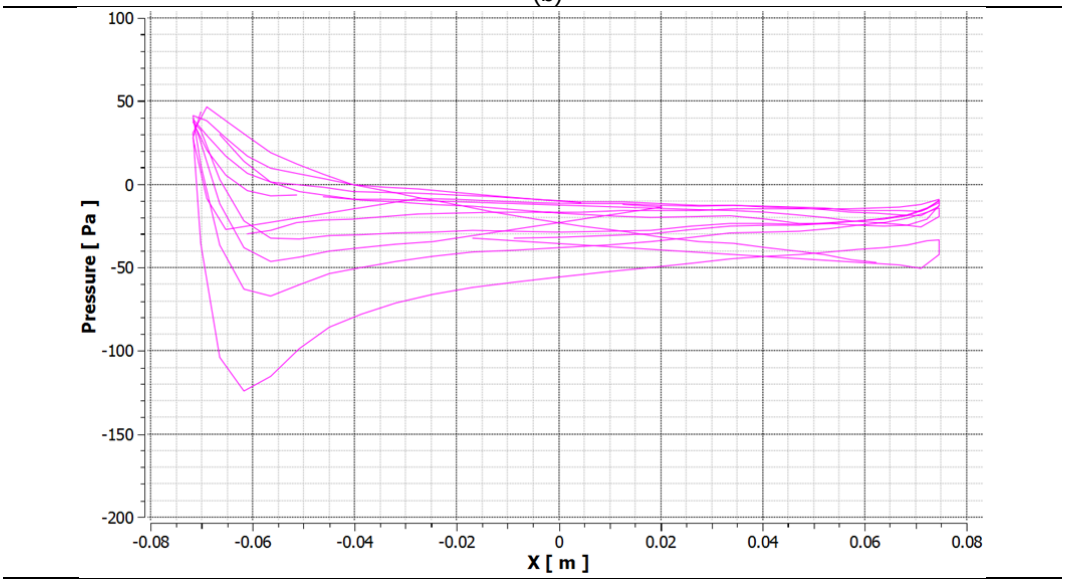

(c)

Figure E-1. (a) Mesh generated around the front, bottom blade of PowerWindow. (b) Pressure counturs around this blade. (c) Pressure created over the five front blades of PowerWindow along their cords.

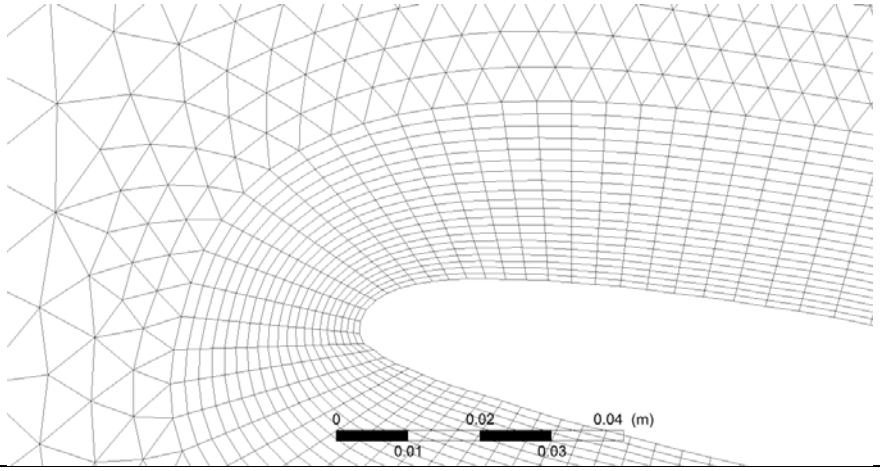

(a)

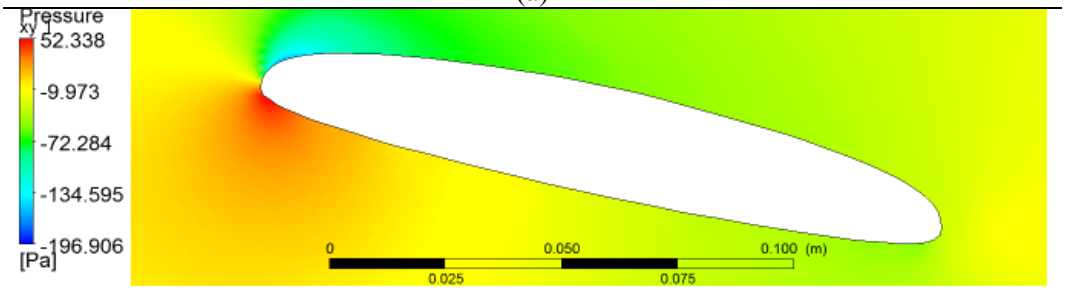

(b)

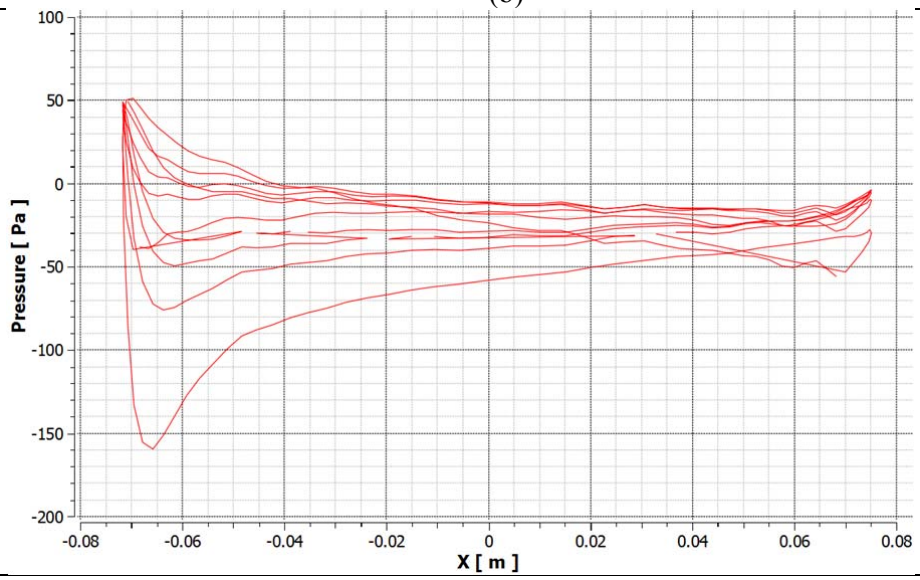

(c)

Figure E-2. (a) Mesh generated around the front, bottom blade of PowerWindow. (b) Pressure counturs around this blade. (c) Pressure created over the five front blades of PowerWindow along their cords.

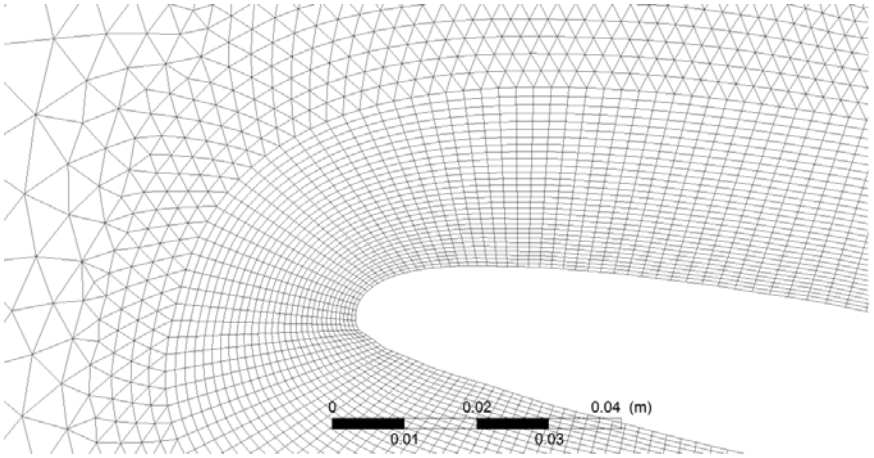

(a)

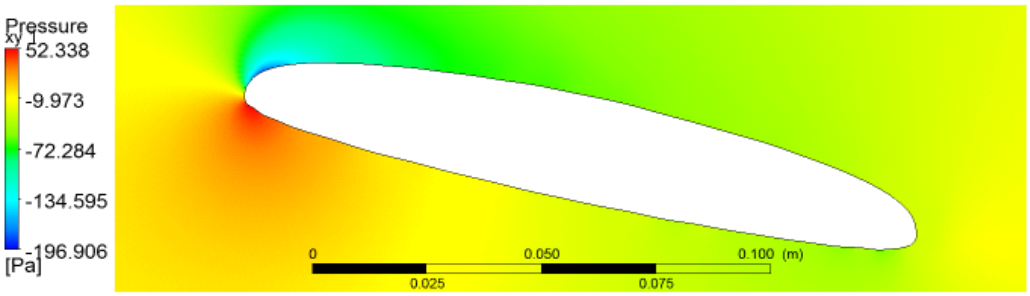

(b)

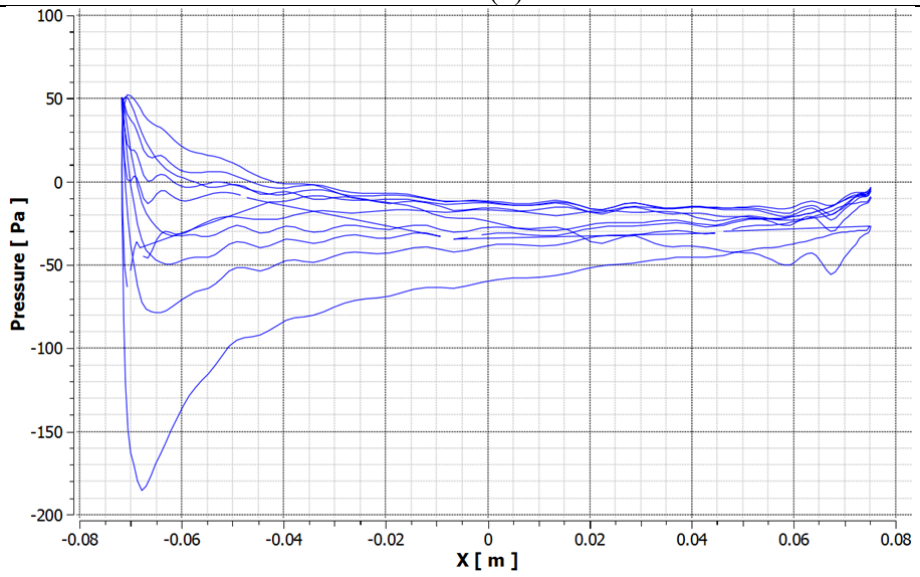

(c)

Figure E-3. Mesh generated around the front, bottom blade of PowerWindow. (b) Pressure counturs around this blade. (c) Pressure created over the five front blades of PowerWindow along their cords.

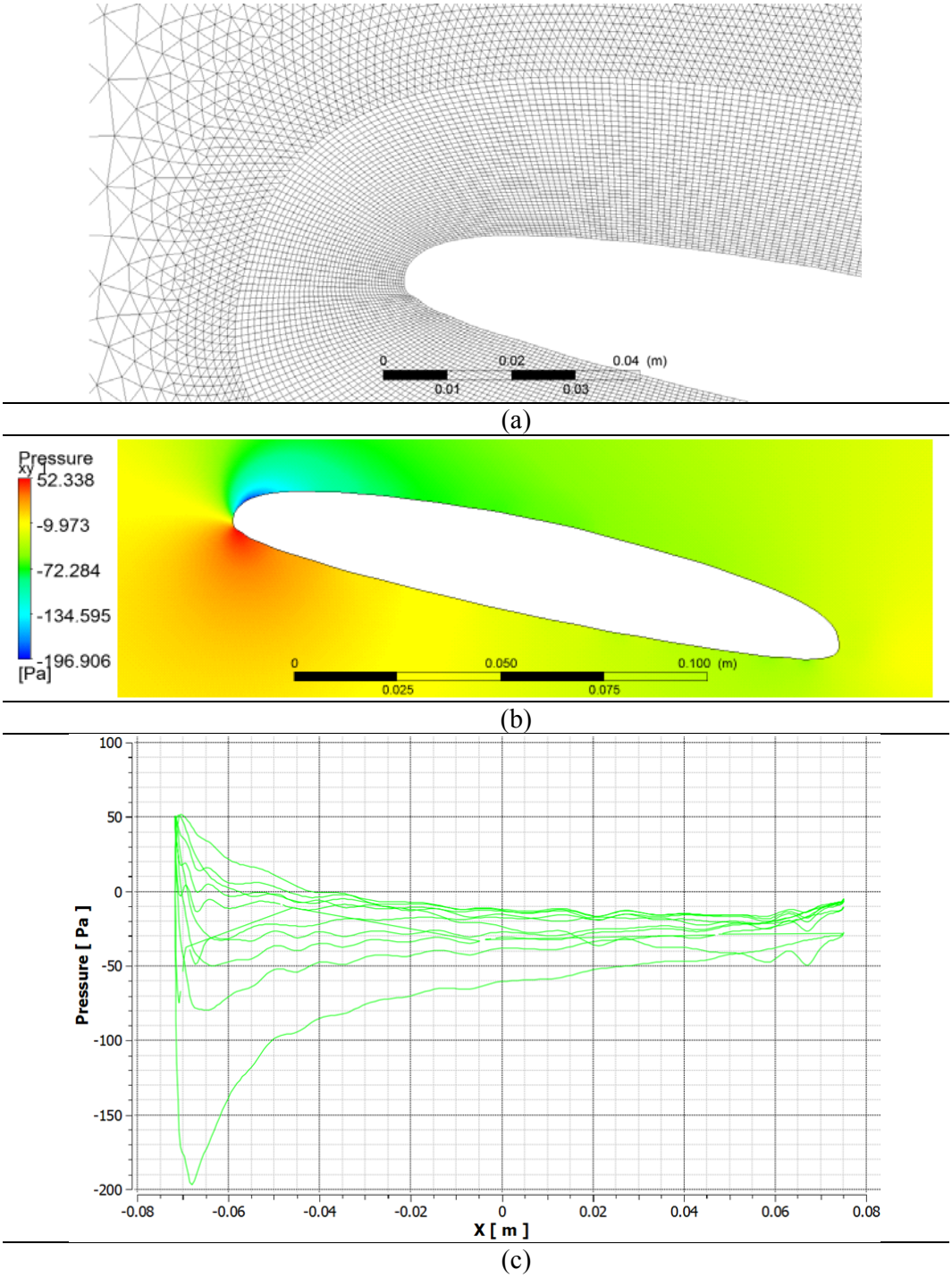

Figure E-4. Mesh generated around the front, bottom blade of PowerWindow. (b) Pressure counturs around this blade. (c) Pressure created over the five front blades of PowerWindow along their cords.